Spring 5-17-2010

Multiscale Modeling and Simulations of Defect Clusters in Crystalline Silicon

Sumeet S. Kapur
University of Pennsylvania, kapurs@gmail.com

Multiscale Modeling and Simulations of Defect Clusters in Crystalline Silicon

Abstract
As the device dimension in semiconductor silicon transistors reach sub-20nm, it significantly enhances the tolerance limits on the size and concentration of defects in the underlying crystalline silicon wafer. Understanding the evolution of defect clusters is critical for controlling the defect density and size distribution within crystalline silicon. The objective of this thesis is to develop the computational methodology that quantitatively describes the evolution of defect clusters in crystalline solids at an atomistic level, and provide a mechanistic understanding of underlying physics behind the defect aggregation process.

In first part of the thesis we develop a novel computational method for probing the thermodynamics of defects in solids. We use this to estimate the configurational entropy of vacancy clusters which is shown to substantially alter the thermodynamic properties of vacancy clusters in crystals at high temperature. The modified thermodynamic properties of vacancy clusters at high temperature are found to explain a longstanding discrepancy between simulation predictions and experimental measurements of vacancy aggregation dynamics in silicon.

In the next part, a comprehensive atomistic study of self-interstitial aggregation in crystalline silicon is presented. The effects of temperature and pressure on the aggregation process are studied in detail and found to generate a variety of qualitatively different interstitial cluster morphologies and growth behavior. A detailed thermodynamic analysis of various cluster configurations shows that both vibrational and configurational entropies are potentially important in setting the properties of small silicon interstitial clusters. The results suggest that a competition between formation energy and entropy of small clusters could be linked to the selection process between various self-interstitial precipitate morphologies observed in ion-implanted crystalline silicon.

Finally in the last section, we investigate the effect of carbon on self-interstitial aggregation. The presence of carbon in the silicon dramatically reduces cluster coalescence, with almost no direct effect on the single self-interstitials. This suggests that suppression of transient enhanced diffusion of boron (in presence of carbon), could be due to the direct interaction between carbon atoms and self-interstitial clusters.

Degree Type
Dissertation

Degree Name
Doctor of Philosophy (PhD)

Graduate Group
Chemical and Biomolecular Engineering

First Advisor
Dr. Talid R. Sinno

Keywords
Silicon, Defects, Inerstitials, Vaccancies, Stress

Subject Categories
Other Chemical Engineering | Thermodynamics

MULTISCALE MODELING AND SIMULATIONS OF DEFECT CLUSTERS IN CRYSTALLINE SILICON

Sumeet S. Kapur

A DISSERTATION

in

Chemical and Biomolecular Engineering

Presented to the Faculties of the University of Pennsylvania

in

Partial Fulfillment of the Requirements for the

Degree of Doctor of Philosophy

2010

_____

Dr. Talid R. Sinno, Supervisor of Dissertation

_____

Dr. Matthew J. Lazzara, Graduate Group Chairperson

Dissertation Committee:
Dr. Talid R. Sinno
Dr. John L. Bassani
Dr. John C. Crocker
Dr. Scott L. Diamond

Acknowledgements

I would like to express my deepest appreciation to my advisor, Professor Talid R. Sinno, for his guidance and invaluable support throughout my graduate career at the University of Pennsylvania. It has been the most enjoyable and satisfying experience to work with a person of his caliber and enthusiasm. His willingness in having regular, insightful discussions and his quest for achieving the most accurate results provided me with the inspiration to work with immense interest and dedication. I also wish to thank the other members of my committee, Professor John L. Bassani, Professor Scott L. Diamond and Professor John C. Crocker, for their patient direction and helpful criticism.

I am very grateful to my officemates and colleagues Manish Prasad, Tom Frewen, Jainguo Dai, Raynaldo Scarlett, and Alex Nieves who have contributed immensely to my personal and professional time at Penn. The group has been a source of friendships as well as good inputs and collaboration. I am also grateful to our Graduate Assistant, Marge Addario and Office Manager, John Linscheid, who kept us organized and were always ready to help.

Finally, I would like to extend a heartfelt thank you and love to my parents Jaswant Kaur and Pritpal Singh Kapur, my sister Harpreet, and my wife Ritu for their constant love and encouragement.

ABSTRACT

MULTISCALE MODELING AND SIMULATIONS OF DEFECT CLUSTERS IN CRYSTALLINE SILICON

Sumeet S. Kapur

Supervisor: Professor Talid R. Sinno

As the device dimension in semiconductor silicon transistors reach sub-20nm, it significantly enhances the tolerance limits on the size and concentration of defects in the underlying crystalline silicon wafer. Understanding the evolution of defect clusters is critical for controlling the defect density and size distribution within crystalline silicon. The objective of this thesis is to develop the computational methodology that quantitatively describes the evolution of defect clusters in crystalline solids at an atomistic level, and provide a mechanistic understanding of underlying physics behind the defect aggregation process.

In first part of the thesis we develop a novel computational method for probing the thermodynamics of defects in solids. We use this to estimate the configurational entropy of vacancy clusters which is shown to substantially alter the thermodynamic properties of vacancy clusters in crystals at high temperature. The modified thermodynamic properties of vacancy clusters at high temperature are found to explain a longstanding discrepancy between simulation predictions and experimental measurements of vacancy aggregation dynamics in silicon.

In the next part, a comprehensive atomistic study of self-interstitial aggregation in crystalline silicon is presented. The effects of temperature and pressure on the aggregation process are studied in detail and found to generate a variety of qualitatively different interstitial cluster morphologies and growth behavior. A detailed thermodynamic analysis of various cluster configurations shows that both vibrational and configurational entropies are potentially important in setting the properties of small silicon interstitial clusters. The results suggest that a competition between formation energy and entropy of small clusters could be linked to the selection process between various self-interstitial precipitate morphologies observed in ion-implanted crystalline silicon.

Finally in the last section, we investigate the effect of carbon on self-interstitial aggregation. The presence of carbon in the silicon dramatically reduces cluster coalescence, with almost no direct effect on the single self-interstitials. This suggests that suppression of transient enhanced diffusion of boron (in presence of carbon), could be due to the direct interaction between carbon atoms and self-interstitial clusters.

Table of Contents

List of Tables

List of Figures

1 Introduction and Motivation

It is difficult to imagine today's world without an electronic gadget, be it your cell phone, computer, or other electronic devices. At the core of all these electronic devices is an integrated circuit (Figure 1.1) or a chip consisting of millions of transistors.

Figure 1.1: Schematic description of the Integrate Circuit (right image) – heart of all electronic devices. [1, 2]

The integrated circuit is most often built on a substrate or a wafer made of single-crystalline silicon using a series of chemical and physical processes. The process of manufacturing integrated circuits can be split into two stages, the wafer preparation and the chip making. During wafer preparation, long cylindrical ingots of high-purity single-crystalline silicon are most often grown using the Czochralski (CZ) crystal growth technique [40]. The cylindrical ingots are sliced into thin wafers which are polished to

create a smooth wafer surface. The polished wafers undergo the next stage of processing, i.e. chip making, which makes use of processes like oxidation, photo-lithography, etching, ion-implantation/doping, annealing etc, to grow millions of transistors and other electronic components on the silicon substrate.

Two trends have dominated the semiconductor silicon industry: increasing wafer size and doubling the transistor count per unit area. Since many integrated circuits are simultaneously built on a single wafer, increasing the wafer size leads to higher number of integrated circuits per wafer, and hence leads to lower production cost per chip, while diminishing the overall use of resources. Keeping in with the trend, today most of silicon wafers are mainly 300mm in diameter, while the next generation of wafers will be 450mm.

In 1965, Gordon Moore predicted that the numbers of transistors on a silicon wafer of a given area will double every 18-24 months (Figure 1.2**:**). Doubling the transistor count on a given area has traditionally been achieved by decreasing the device dimensions, which is a very strong driving force behind today's faster electronic devices. Today's integrated circuits have an average device length of 35-65 nm, and are quickly approaching the sub-20nm regime (see Figure 1.3). However, a decrease in average device dimensions puts additional tolerance limits on the size and concentration of defects in the single-crystalline silicon. Defects in crystalline silicon can exist in different forms and are introduced into the wafer during various stages of integrated circuit manufacturing. For example, voids are known to form during the growth of single-crystal silicon using commercially available Czochralski method [63], whereas large dislocation

loops are observed under high temperature annealing following the ion-implantation process[43]. The concentration of such defects for a 65nm feature-length device, should be less than 0.022/cm^2 for 32nm or larger defects, whereas for the 18nm average length devices (sub-20nm), the maximum allowable defect concentration is 0.017/cm^2 corresponding to 9.0 nm or longer defects [6]. To achieve the device scaling goals it becomes critical to control the quality and quantity of the large crystalline defects formed during the various stages of integrated circuit manufacturing.

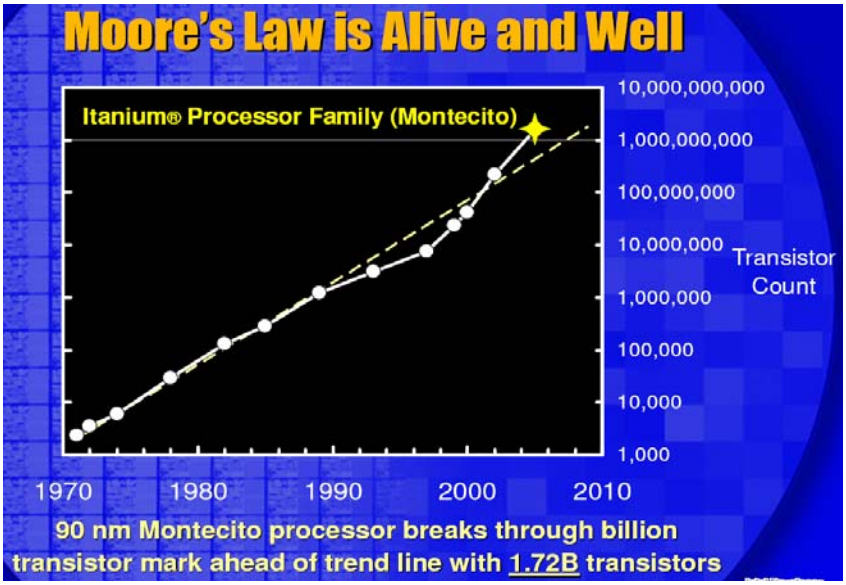

Figure 1.2: Moore's Law (dotted curve) predicts doubling transistor count every two years, Solid point/line: actual Data from Intel Processors, closely following Moore's law for almost 3 decades. [5]

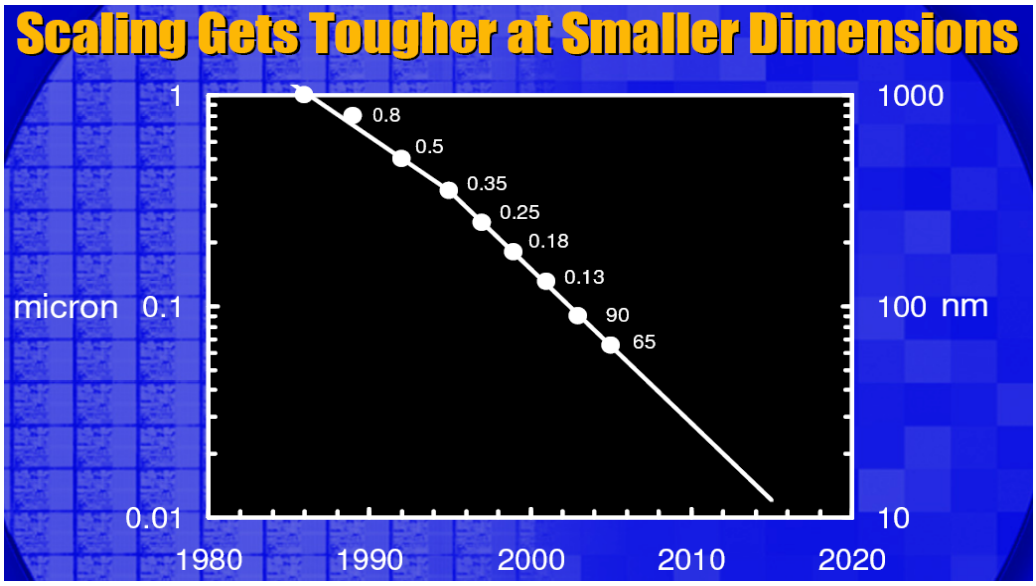

Figure 1.3: Feature length Time Line from Intel [5]. Numbers on curve indicate the transistor gate oxide thickness in nm.

In this thesis, we develop a range of computational and theoretical tools to understand quantitatively the thermodynamics of certain types of crystalline silicon defects. In particular, we study the thermodynamic and structural properties of aggregates of vacancies and self-interstitials which can form during silicon crystal growth and also during the device processing steps such as ion-implantation.

1.1 Defects in Crystalline Semiconductor Silicon

Nothing in the world is perfect. The same is true for crystalline silicon, i.e. silicon crystals inherently possess imperfections in the form of crystalline defects. Crystalline defects can be broadly classified into four types based on their geometry. These are listed in Table 1.1 and are schematically described in Figure 1.4.

Table 1.1: Examples of Crystalline Defects [54]

Defect Type	Examples
Point Defects (zero dimensional)	Intrinsic Defects Vacancy [g] Self-interstitial [c] Extrinsic Defects Substitutional impurity atoms [f,i] Interstitial impurity atoms [a]
Line Defects (one dimensional)	Dislocation Edge dislocation [b] Screw dislocation Dislocation Loops Extrinsic[e] and Intrinsic[h]
Planar (two dimensional)	Stacking Faults Twin Grain boundary
Volume (three dimensional)	Voids Precipitates Interstitial Agglomerates

The most basic of these defects are point defects, which involve misplacement of one atom in the crystal, e.g. a defect where a silicon atom is missing from its lattice position is called a vacancy. If an additional silicon atom is introduced onto a non-lattice position it is called a self-interstitial defect. Vacancy and self-interstitial are an example of silicon atom based defects and are called as intrinsic point defects. Point defects involving foreign atoms are known as extrinsic point defects. , e.g., when a foreign atom occupies a silicon lattice position it is called a substitutional impurity. If a non-silicon atom occupies a non-lattice position it is referred to as an interstitial impurity. The intrinsic point defects do not adversely affect the electronic properties of crystalline silicon if they exist in concentrations below the solubility limit [66]. Indeed, they are

always present at finite temperature because their presence minimizes the free energy of the system.

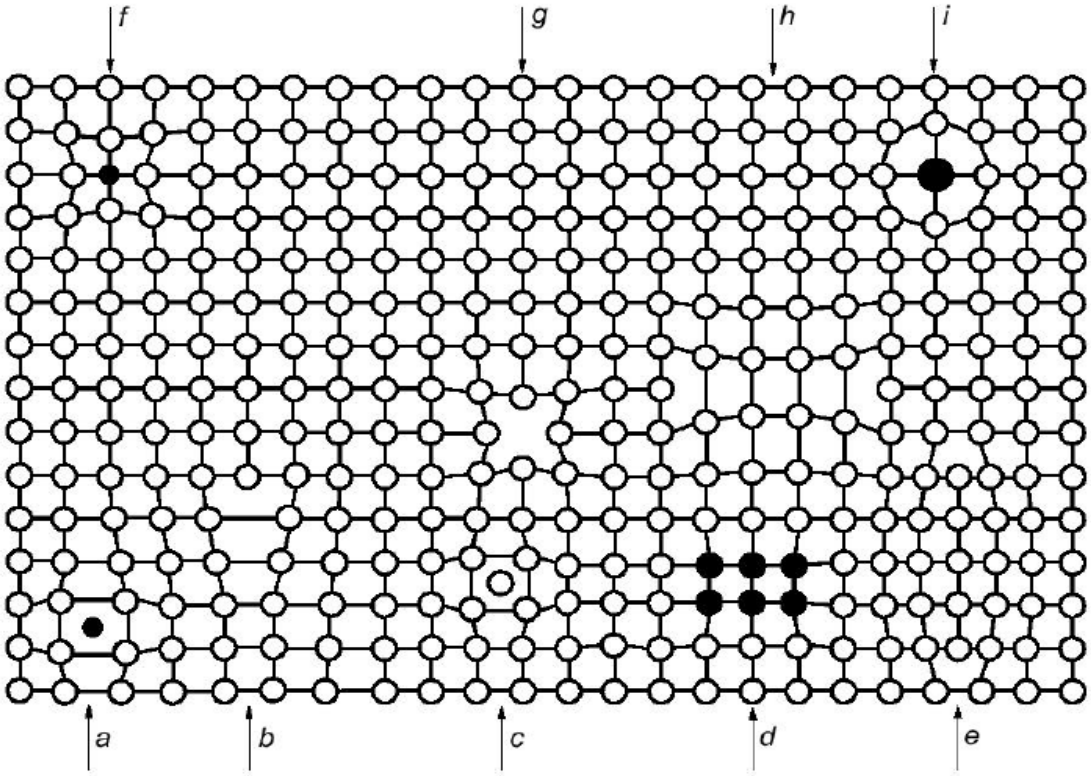

Figure 1.4: Examples of Defects in Crystalline Lattice (a) Impurity Interstitial (b) Dislocation Line (c) Self-Interstitial (d) Cluster of Impurity Atoms (e) Extrinsic Dislocation Loop (f) Small Substitutional Impurity (g) Vacancy (h) Intrinsic Dislocation Loop (i) Large Substitutional Impurity. [54]

However, when present in super-saturation, intrinsic point defects can cluster to form large aggregates, which can be of the same size as microelectronic circuit features and therefore pose problems. These include planar defects and three-dimensional

aggregates (voids, precipitates). Examples are shown schematically in Figure 1.4. A dislocation loop is an example of planar defect wherein an extra plane of atoms (or missing plane of atoms) is created within a crystal. The dislocation loops could be extrinsic or intrinsic in nature, depending upon whether an additional plane of atoms is inserted or removed from the perfect lattice (see Figure 1.4 (e) and Figure 1.4 (h)). Self-interstitials when present in high degree of supersaturation typically form dislocation loops during high temperature annealing. Vacancy aggregates (voids) and small interstitial aggregates ((see Figure 1.4 (e)) are some of the examples of three-dimensional or volume defects. In the following sections, we focus on the two defects that are typically formed during the commercially viable silicon wafer manufacturing and processing steps. The void formation during the Czochralski crystal growth is discussed in Section 1.2 and the self-interstitial aggregation during the post ion-implantation annealing in Section 1.3.

1.2 Void Formation during Czochralski Crystal Growth

Single crystal silicon is commercially grown most often using the Czochralski (CZ) crystal growth process from high-purity poly-crystalline silicon.[63] In the CZ process (see Figure 1.5), the polycrystalline silicon is first melted in a quartz crucible and a seed of single crystal silicon is then dipped into the molten poly-crystalline silicon, and pulled upwards to form long single crystal cylindrical ingots. During the pulling of crystal, individual point defects (vacancies and self-interstitials) are incorporated into the crystal at equilibrium concentrations ($\sim 10^{-6}$ atomic fraction) at the melt-solid interface.

Due to high temperature in the vicinity of the melt-solid interface, the vacancies and self-interstitials are very mobile and hence most of them disappear via the so-called IV recombination reaction,

$$I + V \xleftrightarrow{K_{IV}} Si \tag{1.1}$$

where I and V represent the self-interstitial and vacancy, respectively, and Si represents a silicon atom at a lattice site. The recombination reaction typically leaves one species (vacancy or self-interstitial) to become dominant beyond the thin boundary layer adjacent to the melt/crystal interface- which species survives depends upon the process parameters (crystal pull rate and axial thermal gradients).[48, 152]

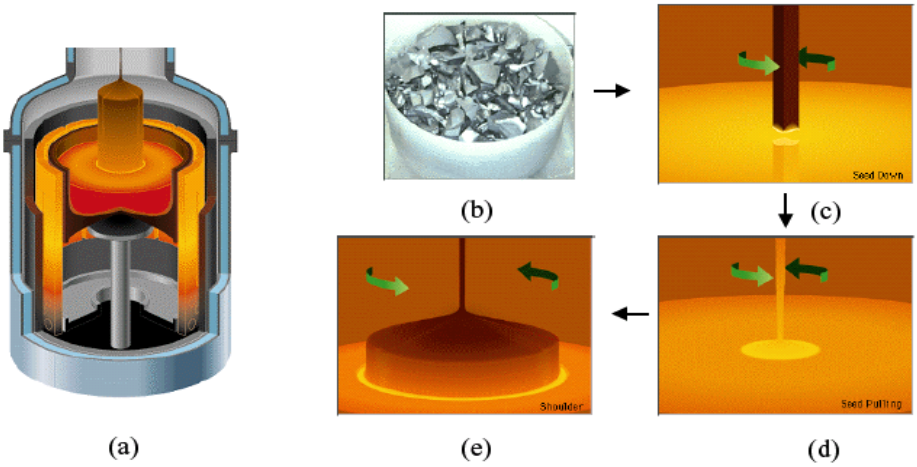

Figure 1.5: Schematic Representation of Czochralski Crystal Growth Process, (a) Czochralski Furnish (b) poly-crystalline silicon in quartz crucible (c) single-crystal seed is dipped into the molten poly-crystalline silicon (d,e) single-crystal silicon is grown by rotating and pulling the seed up. [4]

The native point defects that result from this initial dynamics near melt/crystal interface will then become increasingly supersaturated as the crystal cools, leading to the formation of the relevant type of aggregate. For example voids form by vacancy clustering in the vacancy-rich cluster growth regime whereas stacking faults and dislocation loops form in the interstitial-rich crystal growth regime.

Almost all the CZ-crystals grown today are in the vacancy rich regime, which makes voids as the only major extended defects that form in silicon crystals grown using commercial CZ process. The large vacancy clusters or voids are essentially three dimensional octahedral structures faceted along the (111) plane [81] with sizes typically in the range of 50-120nm. Figure 1.6 shows a transmission electron microscopy (TEM) image of an octahedral void faceted along (111) plane.

The presence of voids in a silicon wafer has detrimental effects on a property known as the Gate Oxide Integrity (GOI) of electronic devices [98]. As a result, the crystal growth conditions should be tailored to minimize the formation of voids during CZ crystal growth process.

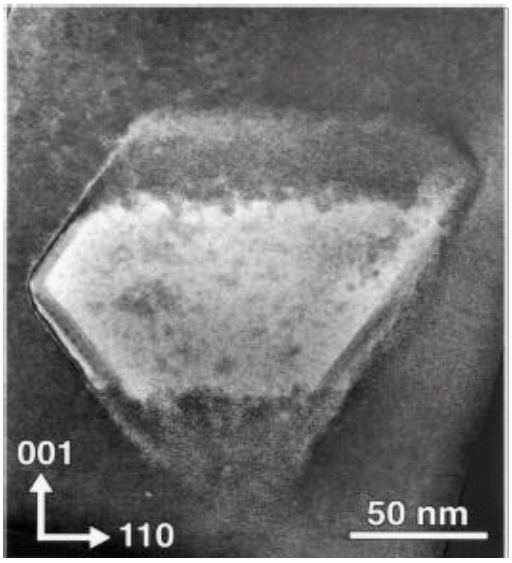

Figure 1.6: TEM Images of an octahedral void. [154]

1.3 Interstitial Aggregation during post Ion-Implant Annealing

Silicon wafers grown using the Czochralski crystal growth process undergo various processing stages during the device manufacturing process. One such step is the implantation of dopant atoms (such as boron/phosphorous) to create electrically active areas within the semiconductor silicon wafer, that eventually governs the performance of electronic devices. Implantation is typically carried out using high energy targeted dopant ion beams at a preset energy level such that ions comes to rest beneath the surface as shown in Figure 1.7 below.

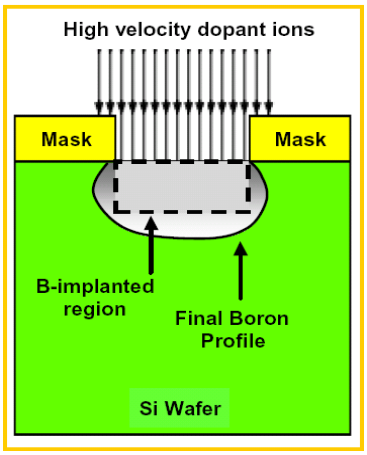

Figure 1.7: Schematic representation of ion implantation and annealing process in silicon wafers. Dopant(B) implantation on a given area is carried out to achieve the desired electronic characteristics. Implantation damages the underlying silicon lattice, which is treated by annealing. Annealing leads to spreading of dopant profiles as these diffuse outwards. [123]

As the high-energy dopant atoms travel through the silicon lattice they create a lot of point defects (interstitials and vacancies) along their path before finally coming to rest. This results in a highly non-equilibrium distribution of point defects (self-interstitials and vacancies) and their clusters[87, 145]. While many of these defects recombine almost instantly, a large supersaturation of self-interstitials is typically left behind because of the net excess atoms present within the lattice following implantation, creating a distribution of interstitial clusters.[87, 145] This causes significant damage to the underlying crystalline silicon lattice. In order to heal the lattice damage as well as move the dopants to the substitutional position (active position), the silicon wafer is annealed at high-temperature following implantation. During annealing, the dopant atoms move to substitutional positions, creating additional self- interstitials in the silicon lattice. The

excess self-interstitial atoms present in supersaturated quantities are thermodynamically unstable and tend to form large interstitial clusters to release the free energy of the system. These interstitial clusters can exist in various sizes and shapes ranging from di-interstitial clusters to large three dimensional and planar interstitial clusters. Apart from forming these extended interstitial clusters, annealing also leads to the spreading of dopants (like Boron) profile beyond the implanted region (Figure 1.8). The spread of boron profile is due to well known phenomenon of transient enhanced diffusion (TED) of boron in presence of excess self-interstitials.[23, 29, 32, 44, 109, 142, 158] Qualitatively, TED is observed because excess self-interstitials effectively increase the mobility of dopant atoms via the "kick-out" mechanism by increasing the fraction of time the latter spend in the mobile interstitial state rather than the immobile substitutional one. However this phenomenon is transient in nature and enhanced diffusion of boron quickly saturates out (Figure 1.8).

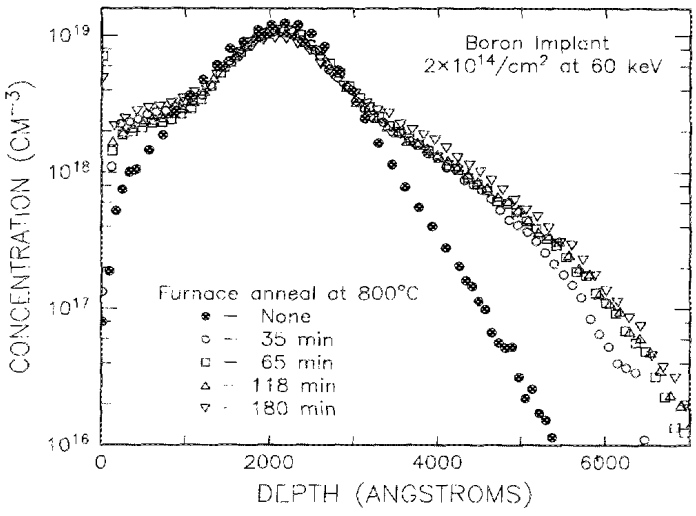

Figure 1.8: Boron concentration profile spreads outwards post implantation anneal at 800°C.[109]

Earlier studies [44] suggested that the source of these excess self-interstitials are the planar interstitial defect clusters named {113} defects (named {113} defects because the <113> crystallographic direction is normal to plane of the defect – see Figure 1.9) formed during the post-implant annealing, which grow to some maximum size and then dissolve during high temperature anneal to release Si self-interstitials. Only recently a conclusive picture has emerged[28], which shows that the supersaturation of self-interstitials present during TED resulted from a complex combination Ostwald ripening of clusters, out-diffusion of self-interstitials to the wafer surface, and a thermodynamic competition between the various possible cluster morphologies. It is this supersaturation of self-interstitials that is responsible for the TED of boron and not the release of self-interstitials from the {113} defects as suggested earlier.

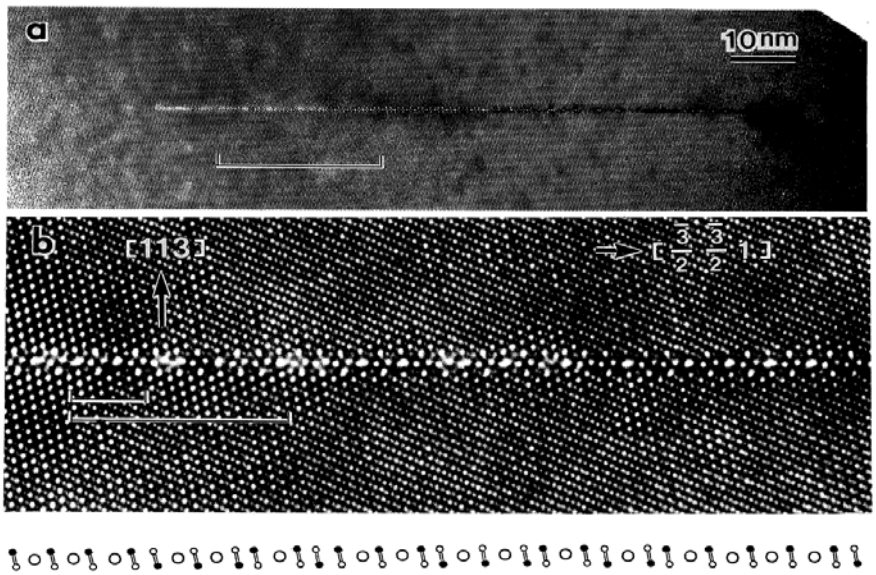

Figure 1.9: HRTEM image of {113} defect in (a), enlarged picture of marked line in (a) is shown in (b). The small open and solid circles represent the interstitials, separated by large open circles (8 membered rings) [34]

Although the model of Claverie et al[28], does explain the source of self-interstitials responsible for the TED of born, but a complete evolution of the extended interstitial clusters involved during the high temperature annealing is still missing. In particular self-interstitial clusters have been observed in a variety of different sizes and morphologies (see Figure 1.10). [36, 44, 74, 88, 89, 106, 107, 116-118, 142, 158] These include small magic clusters like 4 interstitial cluster, 8 interstitial cluster, 12 interstitial cluster etc, rod like line interstitial defects, planar {111}, and {113} defects, large dislocation loops which includes frank partial and perfect dislocation loops and finally the large three dimensional amorphous clusters. It has been a challenge to connect, quantitatively the implantation and annealing conditions to the observed morphologies,

several of which may be present simultaneously. However, in order to control the defect evolution during the post ion-implantation annealing, it is imperative that we understand the structure, formation mechanism and evolution of these extended defects. It must be pointed out that experimental techniques or continuum level models alone cannot provide a conclusive picture, as the later doesn't give any structural details, whereas the former is limited by the minimum image size. We seek to address some of these issues in our work.

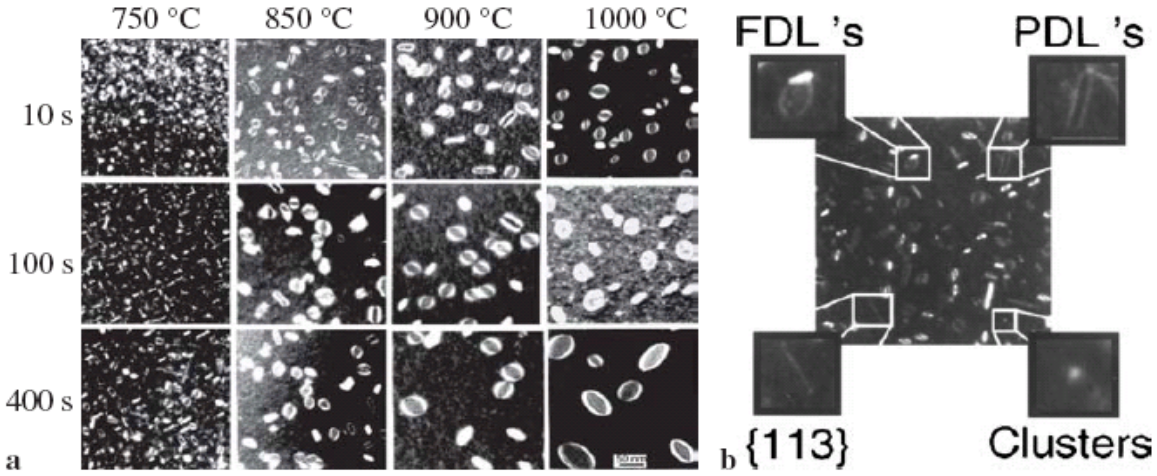

Figure 1.10: Different types of extended interstitial defects after post implant annealing.[28]

1.3.1 Effect of Impurities (Carbon) on Self-Interstitial Clustering in Silicon

Almost all the studies involving self-interstitial clustering in silicon assumes that it doesn't contain any external impurities. This is however rarely true, as the impurities like carbon, oxygen can easily creep into the wafer during the Czochralski crystal growth

process. There has been conscious effort to decrease the impurities concentration in the wafer through various ways.

Until recently carbon was one such impurity which was avoided in silicon, but this changed after Stolk, et al [141] observed a drastic reduction of transient enhanced diffusion (TED) of boron incorporation of carbon above certain concentrations. Figure 1.11 shows boron concentration profiles before (solid line) and after the Si ion implant anneal (dotted line) for two background carbon concentrations ((a): $1x10^{18}/cm^3$ and (b): $2x10^{19}/cm^3$). In the sample with low carbon concentration ($1x10^{18}/cm^3$), boron profile are observed to spread out post implant annealing (see dotted line in Figure 1.11(a)) due to enhanced diffusion of boron, whereas in the sample with higher carbon concentration ($2x10^{19}/cm^3$), (see Figure 1.11(b)), boron profiles stay pinned to their as implanted state – signifying the absence of boron diffusion.

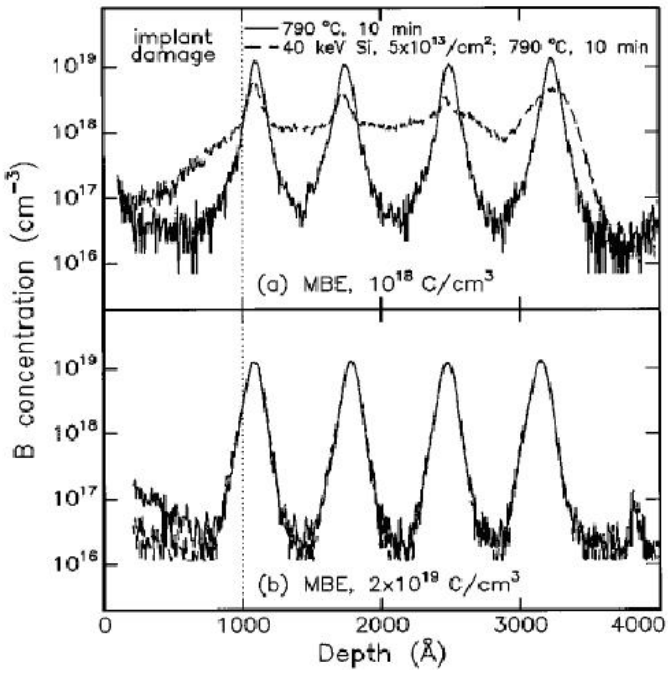

Figure 1.11: Impact of carbon on boron diffusion: (a) Boron concentration profile spreads out post Si implantation anneal for a background carbon concentration of $10^{18}/cm^3$, (b) No spreading in boron concentration profile is observed when the carbon concentration is increased to $2x10^{19}/cm^3$. [141]

In an alternate experiment, Simpson et al [131], have studied the effect of carbon directly on dislocation formation during high temperature anneal following silicon ion implantation onto silicon. They observed that carbon when incorporated onto the substitutional sites leads to complete suppression of dislocation formation in silicon during the anneal stage but has no effect when it occupies non-substitutional sites. In an another study Cacciato et al[21], have observed both the suppression of TED of boron and suppression of dislocation formation during post implant annealing by co-implanting carbon with silicon at 900 ^{o}C. This could be due to the carbon atoms occupying the non-substitutional lattice position as pointed out by Simpson et al[131].

Although it's been postulated that inhibition of TED of boron is due to the interaction of carbon with self-interstitial clusters in silicon, a complete mechanistic picture is missing. Understanding the physics of how carbon interacts with self-interstitial point defects and aggregates in silicon would result in better control over the boron dopant profiles. This is particularly useful as the device dimensions continue to shrink.

1.4 Overall Computational Framework

Our aim is to understand the evolution of defects and defect clusters in silicon and estimate the thermophysical properties for defect clusters under external conditions of stress and temperature. Since the defects are very small in size (less than nm), a direct measurement of the thermophysical properties of defect clusters is not possible using the current experimental techniques. Fortunately a few simulation and modeling methodologies have been developed over the last two decades that have captured the physics under a physical phenomenon reasonably well. These techniques in turn have been used extensively to model the material behavior under a given set of external conditions and have resulted in significant gains in terms of product quality and safety of processes. Depending upon the level of detail and accuracy one wants to achieve with these simulations, the techniques can be broadly divided into four types.

At the most fundamental level is the *ab initio* approach that takes into consideration both the atomic and electronic degrees of freedom. Electronic structure calculations have been used extensively for estimating the defect structures, thermodynamic and transport properties and provide a reasonably accurate estimate in the absence of experimental

data.[7, 18, 47, 104] However the current computing power limit the ability of *ab initio* simulations to $O(100)$ atoms over timescale of $O(10^{-12})$ sec.[55, 73, 156] and as a result, it is almost difficult to study the dynamic aggregation of defects using this approach.

At the next level are the molecular dynamics and Monte Carlo techniques, which use the empirical potentials to describe the interactions between the atoms. Within this approach, the electronic degrees of freedom are averaged out and the behavior of atoms is described using classical mechanics. This results in extending the computing limits to $O(10^6)$ atoms over time scales of $O(10^{-9})$ sec. Various studies have been carried out using the classical empirical atomic potentials to estimate various thermo physical properties of defect and defect clusters, including formation energies and diffusivity , crystal structure, and other transport properties.[8] This approach, based on classical empirical potential offers the most versatile option; and has recently been extended by Manish and Sinno [120-123] to develop a mechanistically consistent picture for aggregation physics of vacancy clusters in Silicon wafer manufacturing.

Instead of simulating the interaction among all the atoms, coarse grained Kinetic Monte Carlo (KMC), offers an alternate technique, where in only the interaction amongst the defects (vacancies and interstitials) is simulated in the form of random sequence of discrete diffusive and reactive events. This offers significant timescale advantage over molecular dynamic and Monte Carlo techniques as the details of atomic vibrations are coarse-grained while retaining the microscopic morphological information. The principal drawback for KMC is that mechanistic information regarding rates for various events has to supplied externally (using either of the approaches mentioned above). The KMC method has been applied extensively in various forms to the study of microstructural

evolution in crystalline materials such as metals and semiconductors. [13, 41, 75, 84, 103] Length scales of the order of 10^{-9} to 10^{-6} m and time scales of the order of 10^{-10} to 10^{0} sec can be achieved using this technique.

If electronic calculations offer the most accurate description of the interaction between atoms, then at the other end of spectrum is the continuum modeling approach, which offers the most practical method in terms of computing time and length scale. Continuum approach is based on conservation of mass, energy and momentum and is numerically modeled using a series of finite difference and finite elements techniques. Although the most practical from computing time perspective, but it suffers from the same deficiency as KMC, in that the atomistic level of detail is lost and is only indirectly captured in terms of parameters estimation.

Depending upon the objective, each of the approach offers an insight at different level of detail. Past two decades of research, have in fact combined used two or more methodologies to arrive at consistent picture of the physical phenomenon. For most of the work done in this thesis we have used the molecular dynamics approach with empirical interatomic potential, as it offers the best option for developing mechanistically consistent picture for estimating the properties of small defect clusters and at the same time helps us understand the evolution of aggregation process of defect clusters using the same empirical interatomic potential and large scale parallel molecular dynamic approach.

1.5 Thesis Objective and Outline

The objective of this work is two fold; the first is to develop computational tools to extract the detailed atomistic information that can used to parameterize the continuum models, and at the same time be able to directly simulate the physical phenomenon at the atomistic level using large scale molecular dynamic simulations.

The second objective is to apply the computational tools we develop, to study the physical phenomenon of aggregation of vacancy and interstitial aggregates in silicon, and make a direct connection between the experiments and simulations.

The remainder of the thesis is organized as follows. In chapter 2 we introduce a novel computational approach for probing the thermodynamics of defects in solids. We use it to estimate the properties of vacancy clusters. The thermo-physical and morphological properties of vacancy clusters evaluated from detailed atomistic simulations are fed into the continuum model and a direct comparison is made to experimentally observed properties like void nucleation temperature, void density, void size distribution etc. Thus detailed atomistic parameters not just specify the parameters for the continuum level simulations but also provide atomistic level details (mechanistic information) about the physics of void aggregation. In chapter 3 we introduce the large scale parallel molecular dynamics simulations approach to study the atomistic evolution of interstitial clusters from small magic clusters to rod like defects to planar {113}, {111} to large dislocation loops (FDL and PDL). A detailed aggregation landscape is proposed as a function of external hydrostatic pressure and temperature. In chapter 4, we use the computational approach for probing the thermodynamics of defects in solids we

developed in chapter 2 for vacancy clusters for studying individual interstitial clusters. Using this method, a comprehensive picture for interstitial aggregation is proposed to explain the evolution of dislocation loops, planar clusters and rod like large interstitial clusters from small magic clusters, under given conditions of external pressure and temperature. In chapter 5, we present a detailed quantitative model to describe the effect of carbon on interstitial aggregation, by using large-scale atomistic simulations. Finally in chapter 6, we summarize the conclusions of this work and suggest directions for future work.

2 Thermodynamic and Structural Properties of Vacancy Clusters

Clustering of point defects and impurity atoms in crystalline materials is a ubiquitous phenomenon that affects a host of material properties. The growth and processing of crystalline semiconductor materials such as silicon, silicon alloys, and gallium arsenide, for example, is almost completely dominated by rules aimed at minimizing the number of defects such as point defect clusters [53, 132, 133], dislocations [36] and stacking faults[126]. Similarly, in metal alloy systems, the microscopic distribution of the component species can often critically affect the mechanical and chemical properties of the alloy [151]. Given the importance of nucleation and growth of clusters in materials processing, there has been much effort aimed at the development of simulation tools for predicting the relationship between processing conditions and the resultant properties (i.e. cluster size distribution) of a material [134]. Most such tools require as input the thermodynamic properties of the various species in a system as a function of temperature and cluster size and composition.

The properties of small atomic clusters, however, are extremely difficult to measure experimentally. As a result, there has been substantial effort aimed at the structural and thermodynamic characterization of clusters using atomistic simulations; for example self-interstitial and vacancy clusters in silicon have been studied extensively with empirical

potentials [39, 120], tight-binding potentials [18, 19] and density functional theory [46, 96]. Much of the atomistic simulation work on cluster characterization has focused exclusively on minimum energy configurations in order to make a thermodynamic and structural description tractable. On the other hand, processing in both metallic and semiconductor systems is often accomplished at elevated temperature where entropy can be important, particularly vibrational and configurational entropy. In this work we describe a novel framework (that inherently includes the vibrational and configurational entropy) for estimating the free energy of point defect clusters in crystalline silicon, at finite temperature based on an analysis of potential energy landscapes[68, 140] created by clusters. We focus primarily on vacancy clusters in silicon using the Environment-Dependent Interatomic Potential (EDIP)[14, 90] but show that our results and conclusions are applicable to other types of clusters and (classical) potential systems and therefore could have broad implications for the thermodynamic analysis of defects in solids.

2.1 Thermodynamics of Cluster Aggregation Process

Single species aggregation is generally described by a series of coupled, reversible interactions between clusters of different sizes.

$$X_i + X_j \underset{F(i,j)}{\overset{K(i,j)}{\leftrightarrow}} X_{i+j} \tag{2.1}$$

where, X_i is the concentration of clusters of size i, and $K(i,j)$ and $F(i,j)$ are the coalescence and fragmentation kernels, respectively. Coalescence and fragmentation rates depend on both kinetic and thermodynamic factors and the coalescence rate of clusters of size *i*, and *j*. The coalescence kernel is given by

$$K(i,j) = A_{ij}(D_i + D_j)\exp\left(-\frac{G_{i+j\to(i+j)}}{k_B T}\right) \tag{2.2}$$

where A_{ij} is a size and morphology dependent geometric factor, D_i is the mobility of cluster *i*, and $G_{i+j\to(i+j)}$ is the free energy barrier associated with the coalescence of clusters *i* and *j*. The latter is usually expressed as [121]

$$G_{i+j\to(i+j)} = \Delta G_{i+j} - \Delta G_i - \Delta G_j - kT\cdot\ln(\frac{\Omega_2}{\Omega_1}) \tag{2.3}$$

where ΔG_i is the formation free energy of a cluster of size *i*, relative to the perfect crystal state. The last term in eq. (2.3) represents the change in the translational entropy of the system associated with the coalescence event, where Ω_1 and Ω_2 are the initial and final numbers of distinguishable ways of distributing clusters in a lattice containing *N* sites for a given cluster size distribution [122]. As defined here, the translational entropy only includes configuration space associated with the cluster centers-of-mass. Note that for most systems of interest, the cluster size distribution is very dilute and spatial overlap can be neglected, although analytic corrections for overlap can be applied [86].

The free energy of formation of an atomic cluster of size i in a crystal can contain several thermodynamic contributions,

$$\Delta G^i = \left\langle \Delta E^i \right\rangle - T\left\langle \Delta S^i_{vib} \right\rangle - TS^i_{conf} \tag{2.4}$$

where ΔE^i is the formation enthalpy, ΔS^i_{vib} the vibrational entropy of formation, and S^i_{conf} the cluster configurational entropy. The $\langle\ \rangle$ indicate averaging over all the individual configurations that the cluster can possess. The vibrational entropy of formation arises because of the extra vibrational modes that are introduced as a result of the cluster. This quantity can be computed directly with normal mode (quasi-harmonic) analysis [76] and/or thermodynamic integration [57, 58].

The cluster configurational entropy is the number of distinguishable configurations that a particular cluster can possess per lattice site. Note that the cluster configurational entropy is fully excluded from the translational entropy as defined above and therefore the total number of ways of distributing clusters in a lattice is given by $\Omega_{tot} = \Omega_{trans}\prod_i \Omega_i^{conf}$, where the product index is over all clusters in the system. While the (ground state) vibrational entropy contribution in eq. (2.4) is usually accounted for in calculations of the formation free energy of a solid cluster, the configurational entropy is often neglected because it is difficult to estimate analytically except for very simple structures. The concept of configurational entropy is described in more detail in the next section.

2.2 Vacancy Cluster in Silicon

Most continuum models for aggregation that require cluster thermodynamics as input assume that the ground state morphology is a good approximation for describing the properties of clusters as a function of size. For vacancies in silicon the ground state morphology is the so-called Hexagonal Ring Cluster (HRC) configuration, which is formed by maximizing the number of complete hexagonal vacancy rings [56]. Examples of HRC structures are shown in Figure 2.1 for several cluster sizes. The HRC morphology naturally evolves into regular octahedral structures with (111)-oriented surfaces at larger sizes, and in this case the cluster configurational entropy can be assumed to be negligible. These octahedral structures are frequently observed experimentally with TEM in commercial crystalline silicon [82].

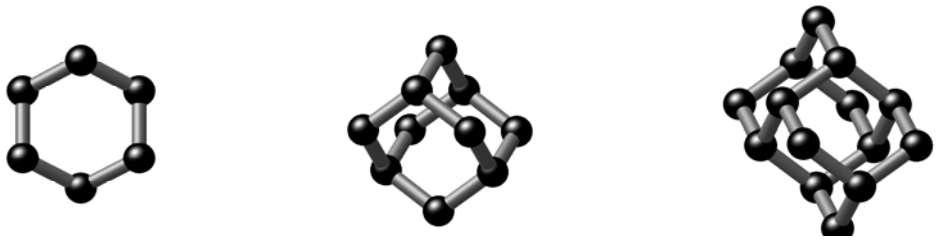

(a) **(b)** **(c)**

Figure 2.1: Hexagonal ring clusters (HRC) containing (a) 6, (b) 10, and (c) 14 vacancies.

While the HRC morphology is a reasonable representation of large clusters at low temperatures, much of semiconductor processing (and obviously crystal growth) takes place at high temperatures. Previous atomistic simulations by Prasad and Sinno, [121,

122] employing the classical EDIP potential [14] demonstrate clearly that vacancy clusters at elevated temperature spend a majority of the time in spatially extended configurations that are much higher in energy than the ground state. The fact that vacancy clusters can assume these extended configurations arises from the large vacancy-vacancy interaction distance, which has been shown to extend up to about 7.8 Å, which corresponds to the 4th neighbor shell along the (110) direction (4NN-110) or the 8th-nearest neighbor shell overall [122]. The driving force for this behavior is now known to be a combination of vibrational and configurational entropy. Only the former has been considered in previous thermodynamic models and it is shown in the following sections that the configurational entropy at high temperature not only dramatically influences the thermodynamics of clusters, but also the aggregation kinetics through a modification of the effective capture radius.

2.2.1 Configurational Entropy

As pointed out in section 2.1, the configurational entropy of a system consists of two terms, the translational and (internal) configurational part, with total number of configurational states given by $\Omega_{tot} = \Omega_{trans} \prod_i \Omega_{conf}^i$. The nature of these terms is demonstrated in Figure 2.2 for the case of a dimer (two vacancies located next to each other) on a two-dimensional (9x9) cubic lattice. For such a system consisting of only the dimer, the total number of states reduces to $\Omega_{tot} = \Omega_{trans}\Omega_{conf}$, with $\Omega_{tot} = 81x2$ being the total number ways of putting the dimer on a 9x9 lattice, where as $\Omega_{trans} = 81$. The dimer

therefore has 2 distinct (energetically degenerate) configurations per lattice site; i.e. $\Omega_{conf} = 2$.

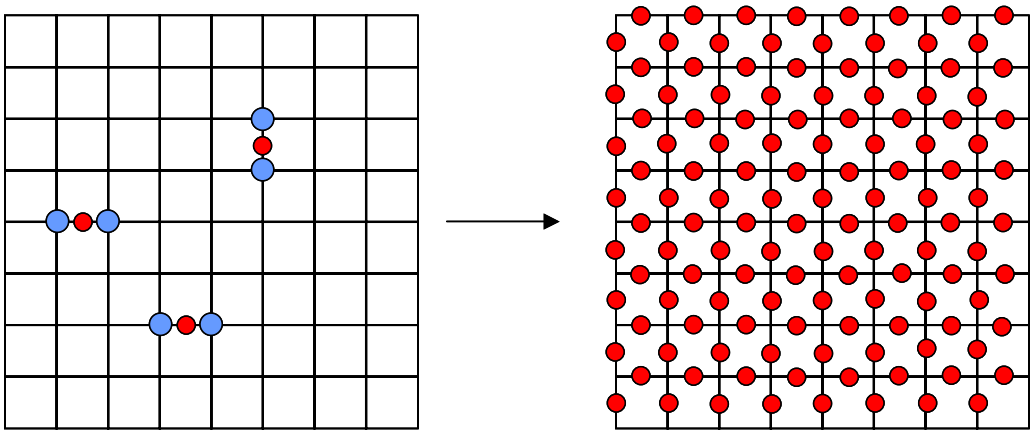

Figure 2.2: (a) Centres of mass of several dimmers on a two dimensional lattice (left). (b) Full center-of-mass lattice for dimmers is twice as dense as that of actual lattice (right).

The situation is far more complex for "real" vacancy clusters in the tetrahedral silicon lattice for several reasons. The first is that long-ranged vacancy-vacancy interactions (up to the 4th nearest neighbor along the (110) directions, or about 7.8 Å) The effect of long-ranged interactions on the cluster configurational entropy is shown in Figure 2.3 in which the schematic dimer shown in Figure 2.2 can now exist in 2nd-nearest neighbor (2NN) configurations as well as the 1NN configuration. The center-of-mass lattice now contains three sites for each of the actual lattice sites and $\Omega_{conf} = 3$ for this case. Note that the energy of the dimer in the 2NN configuration is generally not equal to

that of the 1NN configuration and the microcanonical expression for the entropy is no longer valid because the system has different energy states.

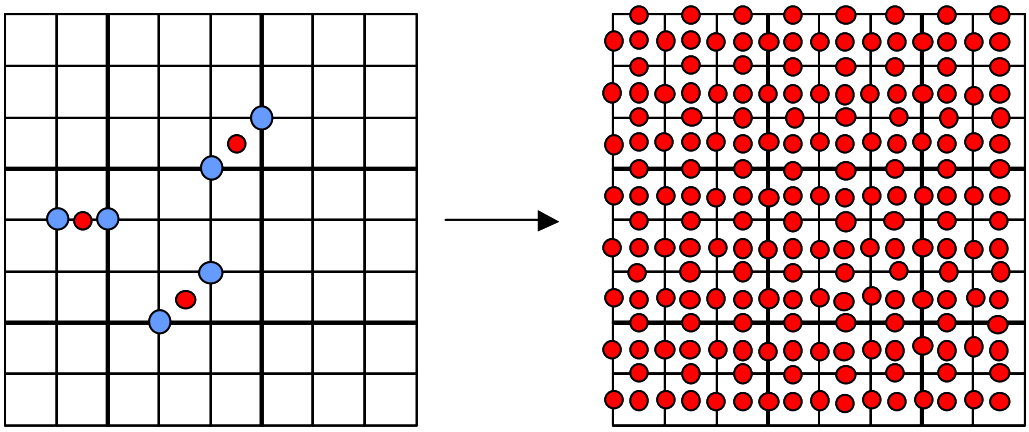

Figure 2.3: (a) Centers of mass of 1NN and 2NN dimers on a two-dimensional lattice (left). (b) Full center-of-mass lattice for 1NN and 2NN dimmers (right).

A second source of large configurational entropy is that cluster configurations in the silicon lattice are not limited to on-lattice structures because lattice atoms can relax around the cluster in a variety of configurations. Both these issues will be discussed further below.

2.3 Cluster Formation Thermodynamics from Potential Energy Landscape

In the following discussion we employ the concept of inherent structures (IS) in a potential energy landscape (PEL) in order to describe the thermodynamics of defect clusters in a crystal. Inherent structures, as introduced by Stillinger and Weber [138], are local minimum configurations in the 3N-dimensional potential energy surface [68] defined by the coordinates of an N-atom system. A *basin* is defined as the set of points in phase space that map to the same IS when the system is quenched using local energy minimization. The basin construct is useful because it partitions the total phase space of the system into a set of non-overlapping local minima connected by saddle points which permit basin-to-basin hopping. At sufficiently low temperature, the system will spend the majority of time in any given basin and only occasionally be able to pass through to another basin (i.e. the basin-to-basin motion is a rare event).

The concepts of inherent structures and potential energy landscapes have existed for a long time [68] and have recently been successfully applied to the study of configurational entropy in supercooled liquids and glasses [128, 129]. In these studies, long equilibrium MD trajectories were periodically quenched to locate the potential energy basins, which were then used to compute thermodynamic properties as shown below. Because of their disordered nature, supercooled liquids and glasses possess a large number of inherent structures, and at sufficiently low temperatures, the basin-hopping picture has been shown to be a good thermodynamic description.

On the other hand, the IS/PEL framework has not yet been applied to the study of defect formation properties in crystals principally because small defect clusters in crystals are generally not associated with substantial configurational entropy. This is especially true for structures that are assumed to primarily exist in on-lattice conformations, such as vacancy clusters. In the following discussion, we briefly outline the IS/PEL thermodynamic framework as applied to the formation properties of defect clusters in crystals. In the following pressure is assumed to be zero, and no distinction is made between the Helmholtz and Gibbs free energies.

In general, the free energy of a system in the canonical ensemble is given by

$$G = -k_B T \ln Z \tag{2.5}$$

where Z is the canonical partition function:

$$Z = \frac{1}{N!}\frac{1}{\Lambda^{3N}}\int \exp\left(-V(\bar{r})/k_B T\right) d\bar{r}^{N} \tag{2.6}$$

In eq.(2.6), $\Lambda = (h^2/2\pi m k_B T)^{1/2}$ is the thermal de Broglie wavelength that arises from integration of the kinetic portion of the partition function, and $V(\bar{r})$ is the potential energy of the system, which depends only on the 3N-dimensional position vector, $\bar{r}$. Applying the IS picture introduced above, the partition function can be rewritten as

$$Z = \frac{1}{\Lambda^{3N}} \sum_{\alpha} \exp\left(-\beta V_{\alpha}\right) \int_{R_{\alpha}} \exp\left(-\beta V(\bar{r}_{\alpha})\right) d\bar{r}^{N} \tag{2.7}$$

where $\beta = 1/k_B T$, V_{α} is the minimum potential energy in basin α, $V(\bar{r}_{\alpha})$ is the potential energy relative to the minimum for a particular configuration in basin α, and R_{α} is the set of configurational phase space points contained in basin α. Further assuming that basins are uniquely characterized by their minimum energy, V_{α}, eq. (2.7) can be rewritten as [129, 138]

$$Z = \frac{1}{\Lambda^{3N}} \int g(V_{\alpha}) \exp\left(-\beta V_{\alpha}\right) \exp\left(-\beta G_{vib}(\beta, V_{\alpha})\right) dV_{\alpha} \tag{2.8}$$

where $g(V_{\alpha})$ is the density-of-states function (DOS) for the distribution of basin energy minima. The temperature-dependent quantity $G_{vib}(\beta, V_{\alpha})$ represents the (vibrational) free energy of a basin with minimum energy V_{α}, i.e. $G_{vib}(\beta, V_{\alpha}) \equiv \left(E(\beta) - TS_{vib}(V_{\alpha})\right)$, and $S_{vib}(V_{\alpha}) \equiv k_B \ln N_{vib}$, where N_{vib} is the number of vibrational states in a basin. Therefore, eq. (2.8) can be rewritten as

$$Z = \frac{1}{\Lambda^{3N}} \int G(V_{\alpha}) \exp\left(-\beta V_{\alpha}\right) \exp\left(-\beta E\right) dV_{\alpha} \tag{2.9}$$

The DOS function $G(V_\alpha)$ represents the distribution of *both* configurational and vibrational states, i.e. $G(V_\alpha) = N_{vib} g(V_\alpha)$. Assuming that in a perfect crystal system only a single configurational state exists, the free energy is then given by,

$$G_p = -k_B T \ln\left[N_{vib}^p / \Lambda^{3N} \exp\left(-\beta(E)\right)\right] = 3Nk_B T \ln\Lambda + E - TS_{vib}^p \tag{2.10}$$

For a system containing a feature such as a vacancy cluster, a similar approach can be used but this time the density-of-states function also must account for multiple configurational states:

$$G_d = -k_B T \ln \int \tilde{G}(V_\alpha) N_{vib}^{ref} N_{conf}^{ref} / \Lambda^{3N} \exp\left(-\beta V_\alpha\right) \exp(-\beta E) dV_\alpha \tag{2.11}$$

where the superscript "ref" indicates a reference configuration for each cluster (to be defined) and the "tilde" notation indicates that the density-of-states is normalized so that it is unity at the reference state, i.e. $\tilde{G}(V_\alpha) = G(V_\alpha) / G(V_\alpha^{ref})$. Employing the definition of vibrational entropy given above, eq. (2.11) can be rewritten as

$$G_d = -TS_{vib}^{ref} - k_B T \ln \int \tilde{G}(V_\alpha) N_{conf}^{ref} / \Lambda^{3N} \exp\left(-\beta V_\alpha\right) \exp(-\beta E) dV_\alpha \tag{2.12}$$

For the specific case of vacancy clusters, the formation free energy of a cluster containing N_V vacancies is

$$\Delta G \equiv G_d - G_p \left(\frac{N_h - N_V}{N_h} \right) \tag{2.13}$$

where N_h is the number of atoms in the perfect crystal reference system. Combining eqs. (2.10), (2.12) and(2.13), the formation free energy for a vacancy cluster is given by

$$\Delta G = -T\Delta S_{vib}^{ref} - k_B T \ln \int \tilde{G}(\Delta E) N_{conf}^{ref} \exp\left(-\beta \Delta E\right) d(\Delta E) \tag{2.14}$$

where ΔE is the formation enthalpy of a cluster and is approximately independent of temperature. Note that the momentum and thermal contributions to the total partition function cancel in eq. (2.14), which is now fully based on formation properties. A similar expression can be written for any type of cluster and eq. (2.14) is the fundamental starting point for our free energy calculations. The probability distribution function $p(\Delta E) \equiv G(\Delta E) \exp\left(-\beta \Delta E\right)$ in eq. (2.14) can be directly sampled with equilibrium molecular dynamics, whereas for discrete, on-lattice systems, $g(\Delta E)$ can be computed directly as shown below in section 2.4.

2.4 On-Lattice Calculations of Cluster Free Energy

The IS/PEL framework generally has been applied to continuous space systems. Here, we extend its application to a discrete on-lattice model for vacancy clusters. On-lattice

vacancy clusters are defined as clusters that are formed by removing a set of atoms from a perfect crystal lattice, followed by lattice relaxation with molecular statics. The PEL in discrete space is similar to one in continuous space at zero-temperature and consists of a collection of infinitely narrow basins separated by inaccessible phase space. Sampling of this space must be accomplished by moves designed to hop directly (athermally) from basin to basin. Equation (2.14) from previous section is directly applicable to this situation except that the vibrational entropy contribution associated with each discrete configuration must be computed separately.

2.4.1 Wang-Landau Monte Carlo (WLMC) Method

The recently developed Wang-Landau Monte Carlo (WLMC) [155] method was used to investigate the thermodynamics of on-lattice vacancy clusters and generate a density-of-states function for each cluster. The WLMC approach was used because of the large energy differences between the various cluster configurations, which would lead to severe sampling bottlenecks in a standard Metropolis Monte Carlo simulation. Although vacancies in a silicon lattice were considered in this particular study, this approach is applicable to any on-lattice cluster. First, an n-vacancy cluster was generated by removing n atoms from a perfect crystal lattice. The configurational density-of-states function for the formation energy, $g(\Delta E)$, and the visit histogram, $h(\Delta E)$, were initialized to unity and zero, respectively. Both $g(\Delta E)$ and $h(\Delta E)$ were discretized using 0.1eV energy bins. A cluster was defined as connected based on the Stillinger criterion [137] and an interaction range of up to 7.8 Å was assumed. The vacancy

positions were identified by comparison of the quenched lattice to a reference perfect lattice at the same density. The positions of reference atoms that were unmatched by corresponding atoms in the actual lattice were assigned to vacancies.

Monte Carlo (MC) moves were performed by moving a single randomly selected atom (vacancy) to another location picked at random from all sites that were within the interaction distance to at least one of the other atoms (vacancies). Moves that led to fragmented cluster configurations (based on the Stillinger definition) were automatically rejected. For the remaining cases, the formation energy of the cluster configuration was calculated by relaxing the lattice statically at constant volume using a conjugate gradient energy minimization scheme [64] and then applying eq. (2.10).

The WLMC acceptance/rejection criterion for accepting a move from formation energy level ΔE_1 to ΔE_2 is given by

$$p\left(\Delta E_1 \to \Delta E_2\right) = \min\left[\frac{g(\Delta E_1)}{g(\Delta E_2)}, 1\right] \tag{2.15}$$

Each time a formation energy level ΔE is visited the current density-of-states value is multiplied by a factor f>1 so that $g(\Delta E) = g(\Delta E)\, f$. The multiplicative factor f is initially set to a value of exp(1) in our simulations, i.e. $f_1 = 2.718282$. Concurrently, the visit histogram is updated by adding one to the value at that energy level so that $h(\Delta E) = h(\Delta E) + 1$. The simulation proceeds until a minimum flatness criterion is achieved in the function $h(\Delta E)$, which is taken here to be 85%. Once this flatness

criterion is achieved, the value of f is reduced according to the schedule $f_{i+1} = \sqrt{f_i}$, where, i represents the number of simulation "stages" and $h(\Delta E)$ is reset to zero for all energy values. Our simulations were executed until $f_1 = 1.000001$.

The WLMC simulation only provides the density-of-states function up to an arbitrary multiplicative constant. In order to compute an absolute free energy from eq. (2.11) it is necessary to specify the absolute number of states in at least a single energy interval and thereby anchor the $g(\Delta E)$ function. The reference state used in all the ensuing calculations in this Chapter is the HRC configuration because it is relatively easy to isolate and possesses relatively few configurations, which can be counted directly.

2.4.2 Validation of WLMC Approach

The WLMC algorithm was validated by comparison to a direct counting approach. The latter simply generates a sequence of configurations using single vacancy hops and counts the number of new configurations by comparison to a stored list of previously observed configurations. Obviously, the direct counting approach is highly limited because of the relatively small number of configurations that can be stored in memory. A comparison between the direct counting and WLMC predictions for the DOS of a nearest-neighbor-connected 6-vacancy (6V) cluster (i.e. the Stillinger interaction distance is set to the 1st-nearest neighbor distance) is shown in Figure 2.4. Both approaches show a three state DOS function where the lowest energy state is the HRC configuration (6-atom ring) that

has two orientations per lattice site. The other two states are substantially higher in energy but possess about 10^3 equivalent orientations.

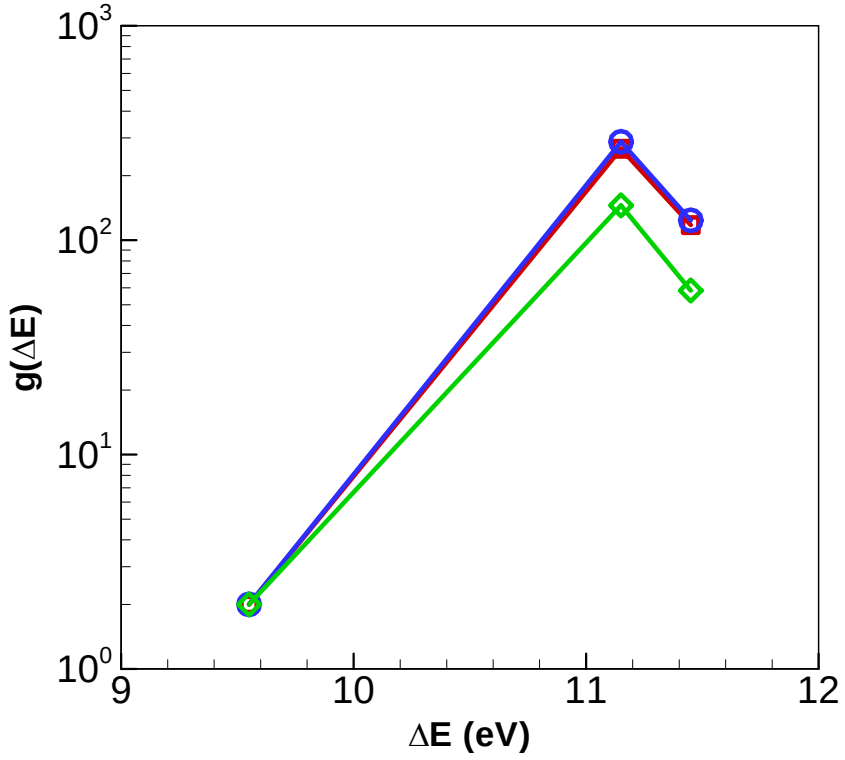

Figure 2.4: DOS for a 1st-nearest neighbor connected 6-vacancy cluster calculated using (a) WLMC (diamonds) and (b) direct counting (circles). Also shown are the results from a corrected-bias WLMC (squares).

A systematic discrepancy is apparent between the results of the direct counting and WLMC calculations, which does not disappear as the visit histogram flatness criterion is increased. The discrepancy arises because of an inherent violation of detailed balance in the simulation move basis set due to the implied constraint imposed by maintaining

cluster connectivity. The constraint that cluster connectivity be preserved before a move can be considered by the WLMC acceptance criterion implies that the number of transitions possible from any given configuration is not uniform. For example, a linear cluster with all monomers arranged at maximum interaction distance can only accommodate moves through its end atoms. On the other hand, a more spherical cluster has many more redundant connections and therefore many more possible "outbound" transitions. In other words, the system can be viewed as a non-uniformly connected graph. A simple example is shown in Figure 2.5 for a 4-state system; the fully connected network is shown in Figure 2.5(a), while a non-uniformly connected version is shown in Figure 2.5(b).

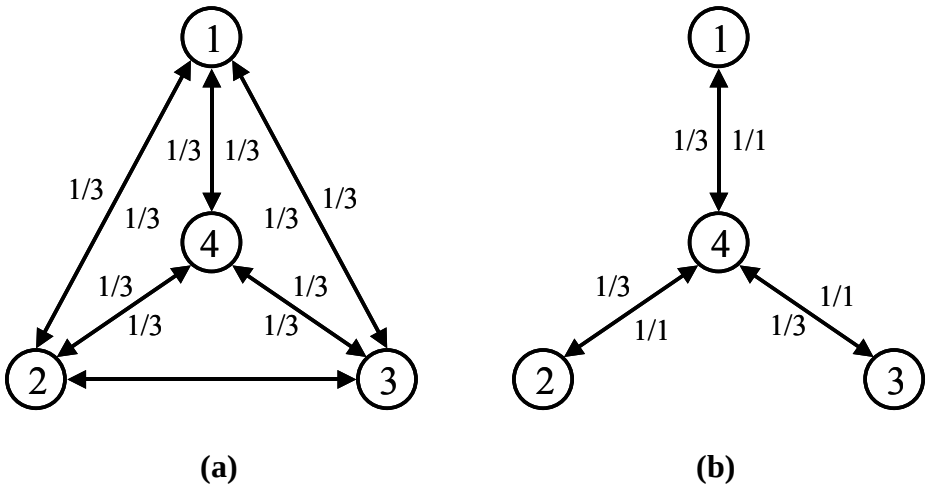

Figure 2.5: Network connectivity and transition probabilities for an energetically degenerate four-state system – (a) Uniformly connected, (b) Non-uniformly connected.

Assuming in both cases that all four states are energetically degenerate, a proper MC algorithm should sample all states equally often. In Figure 2.5(a), each state has three incoming and three outgoing transitions of equal probability (0.33) and using eq. (2.14) would lead to a uniform DOS function. In Figure 2.5(b) however, state 4 has three outgoing transitions (probability of each is 0.33) but the outer states have only one. The outer states could, for example, correspond to cluster configurations that are more extended, and the missing connections therefore represent moves that would lead to fragmentation. Therefore for each of these states, the incoming transition has probability 0.33 of being selected, while the outgoing one has probability 1 of being selected, which clearly leads to a violation of detailed balance. The deviation from detailed balance increases with increasing unevenness in the network connectivity. Using this observation, a bias-corrected WLMC algorithm is generated by modifying the acceptance probability of a transition (eq. (2.14)) so that

$$p\left(\Delta E_1 \to \Delta E_2\right) = \frac{C_1}{C_{\max}} \min\left[\frac{g(\Delta E_1)}{g(\Delta E_2)}, 1\right] \tag{2.16}$$

where C_1 is the number of possible outbound transitions from the state "1" and C_{max} is the maximum number of outbound transitions for any state in the system.

The number of possible transitions is computed by looping over each atom in the cluster and finding the number of locations that it can be moved to while preserving the cluster connectivity. The maximum is estimated at the beginning of the simulation – note that overestimation of this number does not affect the results but only reduces the

efficiency of the simulation by leading to more rejections. The bias-corrected WLMC simulation results for the 6V-1NN cluster are also shown in Figure 2.4 and show excellent agreement with the direct counting results. It should be noted that this issue could generally arise whenever Monte Carlo moves are performed on a non-uniformly connected network, which in this case was due to the cluster connectivity constraint.

2.4.3 Dependence of Density of States on Interaction Distance

As mentioned before, the vacancy-vacancy interaction distance extends substantially beyond the 1st-nearest neighbor distance. The effect of increasing the interaction range between vacancies on the DOS function for the 6V cluster is shown in Figure 2.6. The DOS function is seen to rise dramatically with increasing interaction range and for the 8th-nearest neighbor case has a value of $3x10^{8}$ at 19.5 eV, which is 10 eV higher than the ground state! Obviously, it is not practical to use the direct counting approach for this case. Also note that as the interaction distance increases the form of the DOS function becomes more easily discernable as an exponentially increasing function. The periodic peaks are due to the sudden increase in states as each additional particle is moved away from the cluster core. Also note that as the interaction distance increases, the DOS exponent also increases – the significance of this feature will be discussed in more detail in Section 2.5. Finally, the decay in the DOS at the end is due to the fact that fewer states are available for stretched configurations.

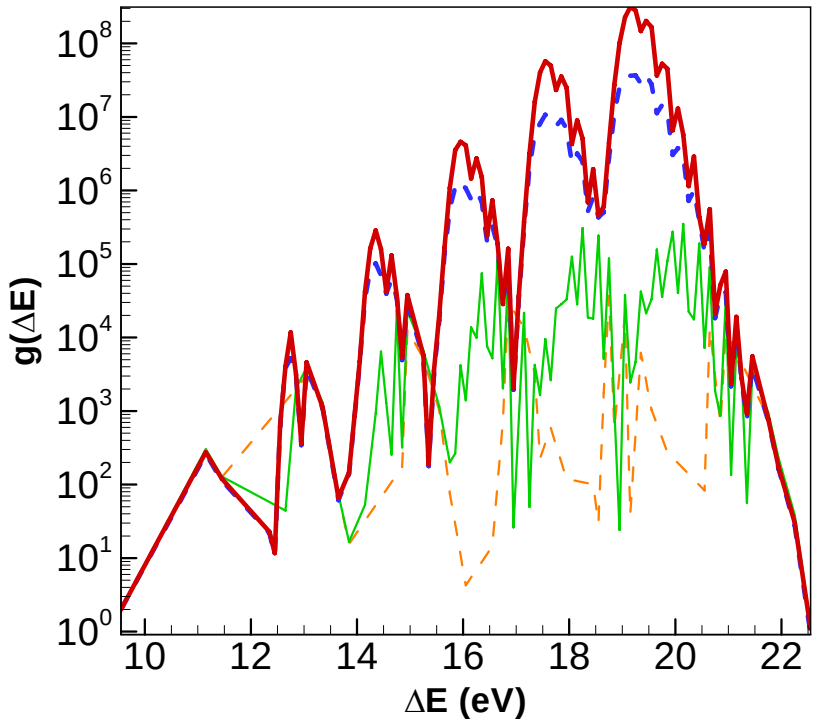

Figure 2.6: DOS for 6V cluster as a function of vacancy-vacancy interaction distance. Lower Dash – 2NN, Thin Solid – 3NN, Upper Dash – 6NN, Thick Solid – 8NN.

2.4.4 Probability Distribution Functions for On-Lattice Vacancy Clusters

The probability distribution function (PDF) for the on-lattice system is given by

$$p(\Delta E) = G(\Delta E)\exp\left(-\beta\Delta E\right) = g(\Delta E)\exp\left(-\beta\Delta E\right)\exp(S_{vib}(\Delta E)/k) \qquad (2.17)$$

Note that the vibrational entropy dependence has to be incorporated explicitly because the different vibrational states associated with each configuration are not sampled with the

on-lattice WLMC simulations. Calculations of the vibrational entropy of formation as a function of cluster configuration and energy are discussed further in Section 2.5. The distribution function in eq. (2.17) can be interpreted as the probability distribution of states obtained from a molecular dynamics simulation that is restricted to only sample on-lattice cluster configurations. The probability distribution, $p(\Delta E)$, for the 6V cluster at 1000K, 1300K, and 1600K is shown in Figure 2.7.

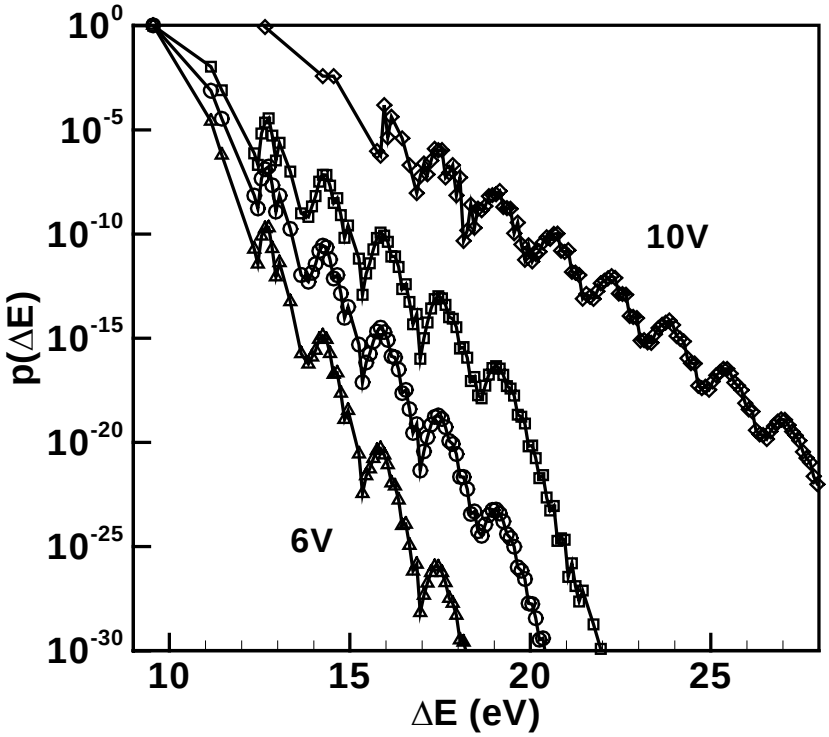

Figure 2.7: Probability distribution functions for the 6V cluster at (a) 1600K (squares), (b) 1300K (circles) and (c) 1000K (triangles) and the 10V cluster (diamonds) at 1600K.

All distributions are arbitrarily anchored so that the probability distribution function is unity at the ground state. While the relative importance of higher energy states increases with increasing temperature, the ground state (corresponding to the HRC configuration) is dominant even at 1600K, which is close to the melting temperature of silicon. The 2nd-lowest energy state (~11eV) is about 100 times less probable at 1600K and $1x10^5$ times less probable at 1000K. States with higher energies are progressively less represented. In other words, even the combination of both the vibrational and on-lattice configurational entropy near the melting temperature is still not sufficient to compensate for the higher energy of any state relative to the HRC configuration. Also shown in Figure 2.7 is the probability distribution for the 10V cluster at 1600 K, which leads to a similar picture, although the decay of the probability distribution function is slower than that for the 6V case, reflecting the faster exponential increase in the DOS function for the 10V cluster. Simulations for clusters up to size 30V fail to show any appreciable impact from non-ground state configurations at all temperatures up to 1600K. Based on these results the total free energy of formation for EDIP vacancy clusters is adequately represented by the free energy of the HRC configuration for all cluster sizes and at all temperatures. In other words, while the on-lattice potential energy landscape does contain a large number of states, the density is not high enough to appreciably contribute to the free energy.

2.5 Off-Lattice Calculations of Cluster Free Energy

Extended EDIP molecular dynamics simulations at 1600K (and to a lesser extent at lower temperatures) show that vacancy clusters spend a majority of time in states that are of

much higher energy than the HRC configuration. This is particularly significant given the predicted high binding energy of the HRC configuration for the 6V vacancy cluster in silicon. Very long NVT-ensemble (zero pressure) MD trajectories of a 1000-lattice site cell containing a 6V cluster were periodically quenched (approx. every 100-200 time steps) to the local energy minimum and the formation energies collected into bins as in the on-lattice WLMC calculation described in the previous section. The resulting PDF is shown in Figure 2.8 and exhibits several fundamental differences relative to the on-lattice MC case.

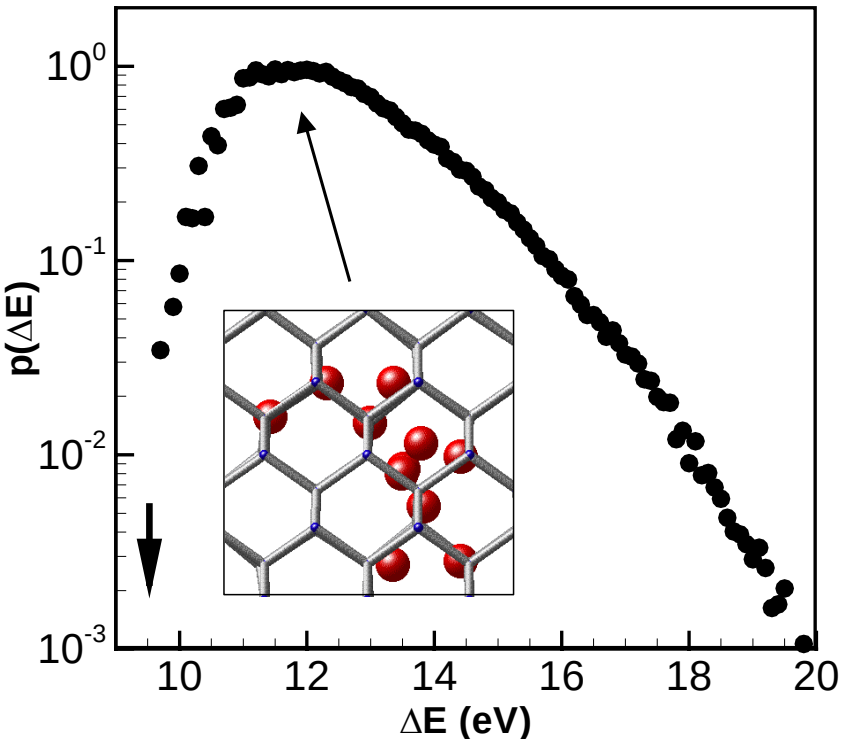

Figure 2.8: Probability distribution function for a 6-vacancy cluster at 1600 K obtained directly from MD. Inset: Spheres represent atoms displaced by more than 10% of a bond length.

Most importantly, the dominant states are now located at approximately 12eV while the HRC ground state is *never* observed during the simulation which was run for about $8x10^7$ time steps or about 50 ns of real time. The distribution also is now much shallower than for the discrete case, which implies that a larger number of configurations contribute to the average thermodynamic properties. Finally, many of the unoccupied bins in the on-lattice case (e.g. states between 9.5eV and 11.0eV) are now populated and the distribution appears to be almost continuous. In fact, the energy spacing between states is less than 0.01eV in some regions of probability distribution function.

An example (quenched) configuration of the simulation lattice in the neighborhood of the 6V cluster is shown in the inset of Figure 2.8. The configuration possesses formation energy in the region of the peak of the distribution (11.8 eV). Several neighboring atoms are significantly displaced from their lattice positions to the extent that it is no longer possible to definitively assign vacancies to particular lattice sites. Other configurations found in the MD simulation show similar off-lattice character and spatial extension, with the higher energy structures becoming increasingly disordered and extended. The increased stability of higher energy structures arises from the tremendous number of possible configurations if substantial off-lattice rearrangements are allowed. Although off-lattice relaxations were permitted in the WLMC calculations during the energy minimizations, these were only sufficient to sample the *local* minimum in the potential energy surface near an on-lattice configuration.

The fact that each configuration sampled using the above procedure corresponds to a well-defined local minimum in the potential energy surface was confirmed by repeated coordinate perturbation followed by re-minimization. Even states that were separated by

less than 0.01eV (the tolerance of our CG minimizations) were reproducibly isolated by energy minimization following coordinate perturbation. Of course, this robustness was observed only if the perturbations did not exceed a certain critical value (about 2-3% of a bond-length) – perturbation magnitudes above this value led to relaxations into different local minima. In general, these local minima possessed substantially different energies (up to ~ 1eV) from the original value. Conversely, states with adjacent formation energies were generally found to correspond to substantially different atomic configurations.

The results above indicate that the potential energy surface contains a large enough density of local minima to substantially alter the thermodynamics of vacancy clusters. This view is schematically represented in Figure 2.9, which contrasts the conventional view (a) of a smooth potential surface experienced by a hopping point defect in a crystal and the present picture (b). The situation in (b) is not unlike the potential energy surface expected in an amorphous solid or supercooled liquid, but here is localized to the vicinity of the defect. Note that these states are introduced into the system by the presence of the point defect and would not otherwise exist in the perfect lattice. In other words they are a property of the defect and therefore modify its thermodynamic properties. The defect clusters therefore act as strong sources of amorphization within the lattice, an idea that has been qualitatively suggested in the literature for many years [130] but has not yet been quantitatively analyzed.

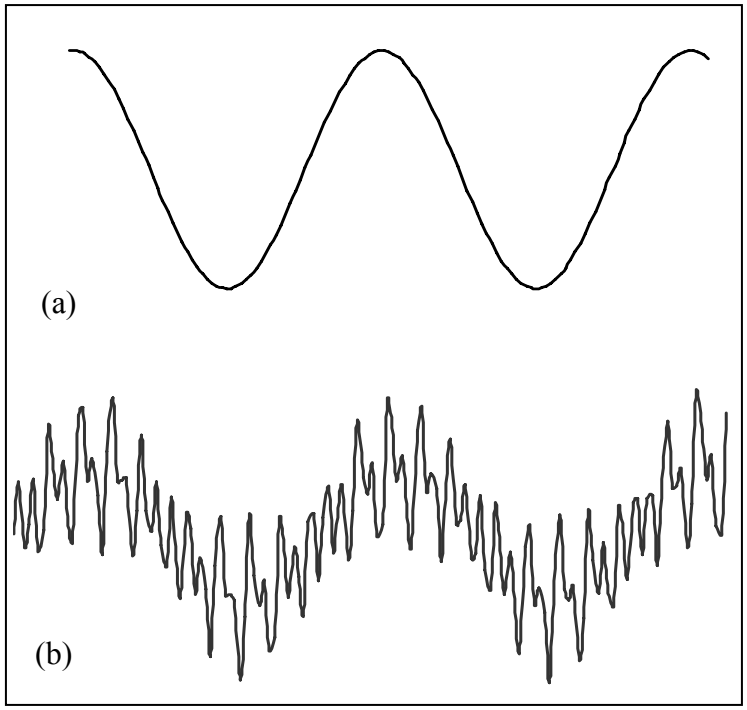

Figure 2.9: Potential energy surface experienced by a single hopping atom in a crystal. (a) without lattice rearrangements, and (b) with lattice rearrangements.

2.5.1 Absolute Probability Distribution and Density of States Functions

The PDFs for several other vacancy clusters containing 2-35 vacancies were also generated using direct MD; examples are shown in Figure 2.10. All distributions have been arbitrarily normalized to unit area. As the cluster size increases, the range of energies sampled by the cluster also increases and, for the 35-vacancy cluster, the difference between the energy at the distribution peak and the HRC structure is about 10 eV or 75 k_BT. Except for dimers and trimers, the distributions are observed to be almost continuous across the entire range of sampled formation energies, with well-defined

peaks at intermediate values. For clusters containing more than 4 vacancies, the HRC configuration was never observed at 1600K, while in the dimer and trimer cases the clusters were observed to revisit the HRC configuration multiple times.

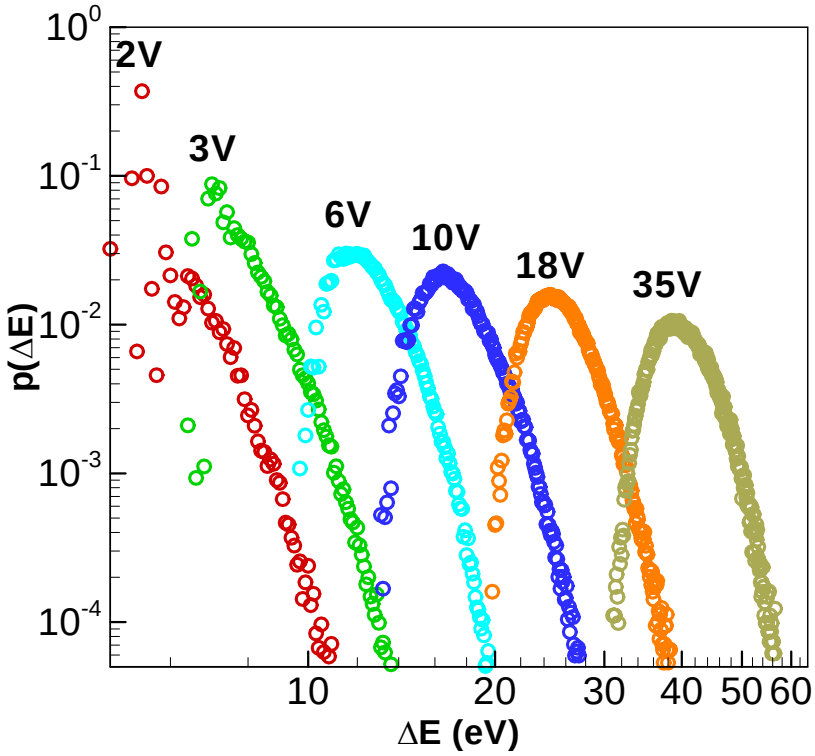

Figure 2.10: Probability distribution functions for vacancy clusters at 1600 K obtained directly from MD.

The PDFs in Figure 2.10 are known only to within a multiplicative constant, which must be determined before they can be used to compute absolute free energies. As in the discrete case, anchoring of a PDF requires knowing the state count in at least one energy bin within the distribution, and in the on-lattice simulations the HRC configuration was

used for this purpose. While the HRC configuration is still a natural anchor for the off-lattice distributions, it is more difficult to utilize it because the 1600K MD simulations do not visit this state as discussed above.

This difficulty was resolved using a second MD simulation at lower temperature in which the HRC structure was sampled adequately while maintaining sufficient overlap with the 1600K distribution. This approach is conceptually similar to umbrella sampling [8] in which distributions across different energy sub-intervals are overlapped to create a complete one. The optimal temperature for the second simulation was determined by balancing the requirement that the HRC configuration be sampled adequately with the need to maximize the overall transition rates to produce a distribution with sufficient statistics in a reasonable amount of CPU time. In fact, the low temperature "anchor" simulations accounted for most the overall computational effort in this study. The high temperature simulations are still required because they sample the cluster configurations much more rapidly and provide better overall statistics over most of the energy range.

Examples of the two-temperature approach are shown in Figure 2.11 for the 6V and 18V clusters. In the 6V case, the low temperature simulation was performed at 1400K while for the 18V cluster a temperature of 1050K was used. Note that for both the 6V and 18V clusters, the distributions are plotted at the low temperature; i.e. the 6V distributions are shown at 1400K and the 18V distributions at 1050K. While almost full overlap between the low and high temperature distributions could be achieved in the 6V case, the large temperature difference between the two simulations used for the 18V case implied that only a relatively small part of the distributions overlapped (~3-4 eV in the formation energy range) and could be used for anchoring the 1600K data.

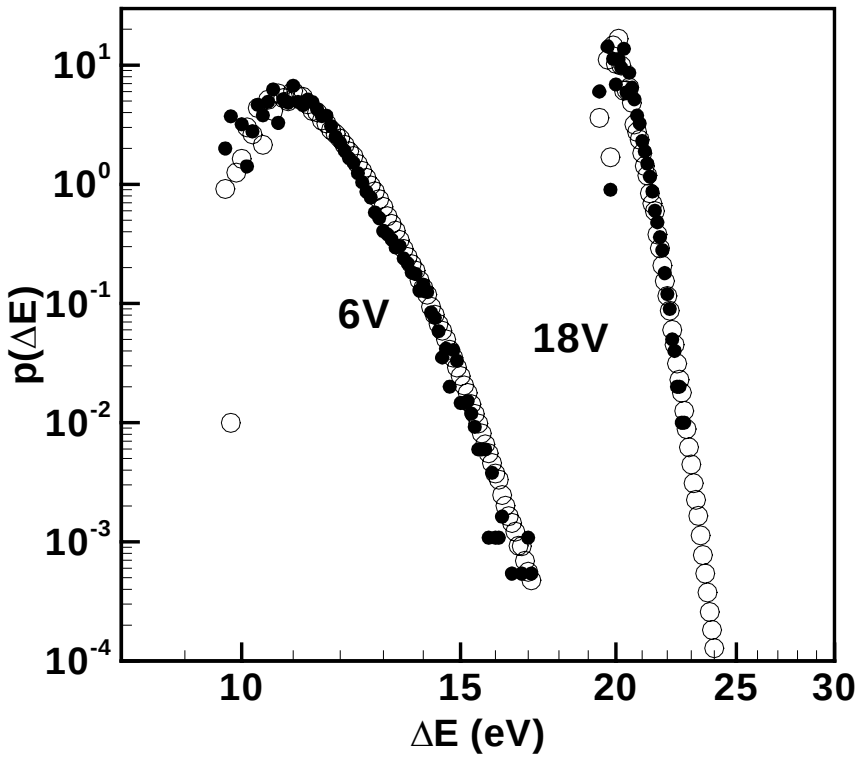

Figure 2.11: Overlap between probability distributions sampled at two different temperatures for the 6V and 18V clusters. Solid symbols – low T, Open symbols – high T. All data shown is scaled to the lower temperature (1400K for 6V, 1050K for 18V).

The corresponding absolute density-of-states functions (obtained by sampling at 1600K) for the various cluster sizes are shown in Figure 2.12. The solid black circle symbols are the (directly counted) density-of-states for the HRC configurations. Also shown for the 6V and 18V clusters are DOS functions obtained from the low-temperature simulations, which are seen to overlap extremely well with the corresponding high-temperature data. Each of the DOS functions rises exponentially after an initial deviation, and appears to be unbounded. This exponential growth in the DOS functions is not inconsistent with the concept of a thermodynamically stable cluster because the

distributions in Figure 2.10 are bounded. In other words, even though DOS functions grow exponentially, the Boltzmann factor decreases with a higher exponent. Physically, the unbounded DOS functions point to the fact that each cluster can spawn an infinite number of higher energy states – in fact, the states near the tail end of the DOS functions in Figure 2.12 possess energies that are higher than a completely dissociated cluster, even though they represent valid Stillinger clusters.

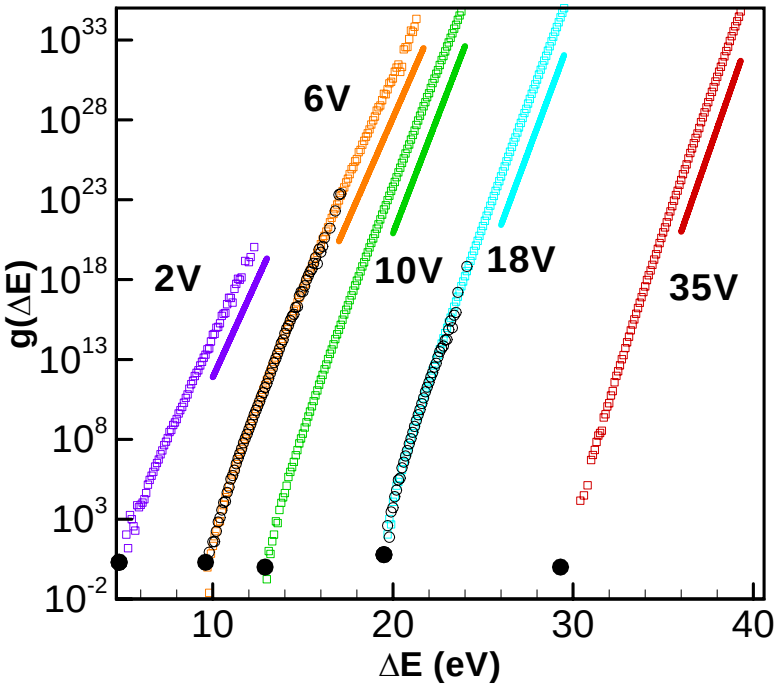

Figure 2.12: Absolute density-of-states functions. Small squares – data derived from sampling at 1600K; Solid circles – directly counted HRC degeneracy; Large open circles – DOS sampled at 1400K (6V) and 1050K (18V); solid lines – exponential fits.

These configurations correspond to the formation of additional defect structures such as Frenkel pairs (interstitial-vacancy pairs) [157] and other types of disordered states, and suggest a mechanism for amorphization and even crystal melting.

A plot of the DOS exponents as a function of cluster size is shown in Figure 2.13 in which the exponents have been expressed as effective temperatures, i.e. $G(\Delta E) \sim \exp(\beta_{eff} \Delta E)$, where $\beta_{eff} \equiv 1/kT_{eff}$ is the fitted exponent for a given DOS. For effective temperatures above the crystal melting temperature (~1520K), the probability distribution, $p(\Delta E) = G(\Delta E)\exp(-\beta \Delta E)$ is bounded and the crystal is stable.

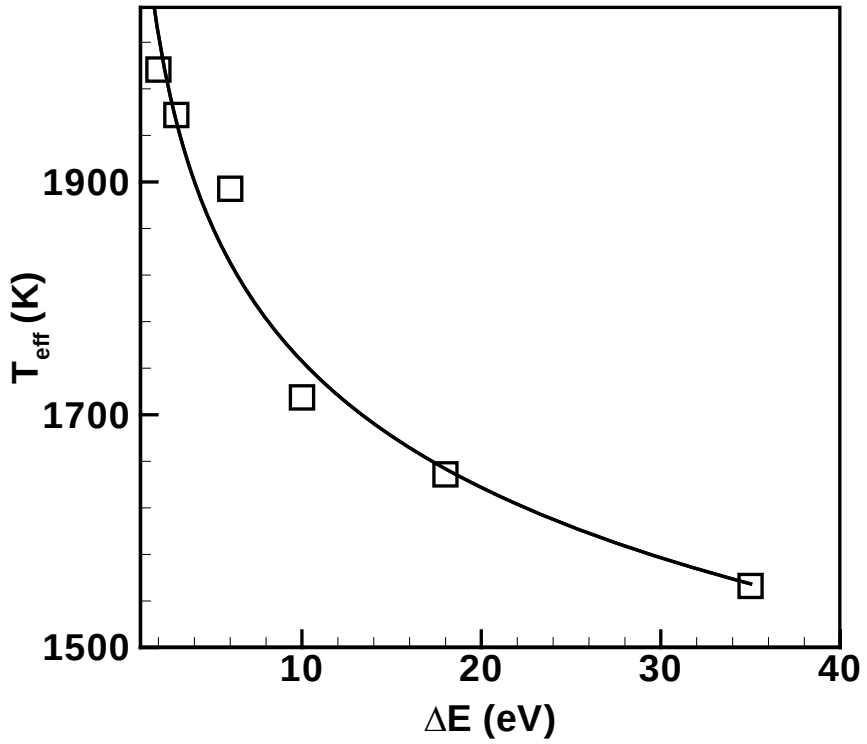

Figure 2.13: DOS exponent dependence on cluster size. Line is a power-law fit.

As shown in Figure 2.13, the effective temperature appears to approach this limit as a power-law in the cluster size over the range studied, although larger cluster sizes would be required to completely determine the limiting behavior. In other words, the additional states introduced by clusters provide a path for crystal melting to occur, and larger clusters produce a higher state density. More work is needed to develop a conclusive relationship between the crystal melting and the effective temperature.

2.5.2 Total Cluster Free Energy Calculations

The distribution functions shown in Figure 2.10 and Figure 2.12 were used to compute free energies of formation for each of the clusters, which are a critical ingredient in continuum simulations of aggregation. The formation free energies were computed as a function of cluster size and temperature using eq. (2.14). Details of the vibrational entropy calculation for the various configurations are given below in Section 2.5.4.

The temperature and size dependence of $\Delta G(n,T)$ is shown explicitly in Figure 2.14 (lower plane) by defining an effective surface free energy as $\sigma = \Delta G(n,T)/\alpha n^{2/3}$, where $\alpha = 2.224$ for a sphere (α increases by about 10% for an octahedron). Also shown is the surface free energy obtained using conventional ground state calculations in which the enthalpy and vibrational entropy of formation for the HRC are computed as functions of temperature (upper plane). Several observations can be made. First, the surface energies computed using both approaches converge at low temperature where the configurational entropy is negligible.

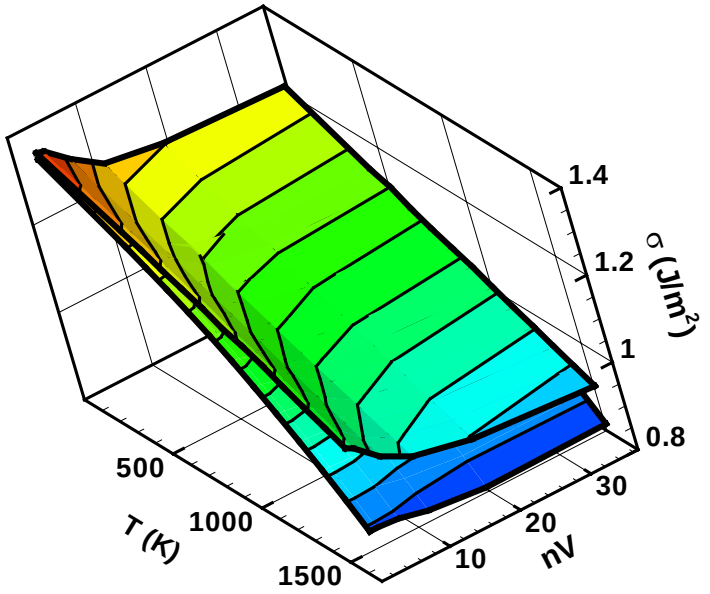

Figure 2.14: Temperature and size dependence of the total effective surface free energy (σ) of vacancy clusters predicted using the EDIP potential. Lower surface: current results including configurational entropy, Upper surface: HRC calculations with vibrational entropy only.

The agreement at low temperature provides a good consistency check because the present results are extrapolated from high temperature using the density-of-states function. At high temperatures, a substantial deviation between the predicted surface energies is apparent because the surface energy predicted by including the configurational entropy decreases more strongly with temperature than the HRC curve. The deviation is greatest for small clusters because the relative effect of configurational entropy is greatest for these sizes.

Interestingly, at high temperatures the effective surface energy predicted in the present work is approximately constant over the size interval 2<n<35, implying that the free energy of formation scales as $n^{2/3}$ for all cluster sizes considered. In addition, based on previous analyses, the 35-vacancy cluster is fully representative of the continuum limit because it is the smallest structure that can assume a perfect (111) faceted octahedral shape [122]. As a result, the present calculations indicate that the surface free energy scales as $n^{2/3}$ for *all* sizes at elevated temperatures. At lower temperatures, however, the smallest clusters clearly possess higher effective surface free energy and deviate from the $n^{2/3}$ scaling law (for both sets of calculations). The observed deviation for small clusters arises because at low temperatures the effect of configurational entropy is negligible and the atomistic (discrete) nature of the clusters leads to a higher effective surface free energy as observed in previous thermodynamic analyses [122]. By contrast, in the HRC calculations, the increase in effective surface energy for small clusters is present at all temperatures because the atomic discreteness of the HRC structure is preserved (by construction).

A more direct comparison between the present calculations and the HRC results is shown in Figure 2.15(a). The contour lines represent the difference between the ground state HRC and total free energy calculations from this work, defined as $(\sigma_{HRC} - \sigma_{FULL})/\sigma_{FULL}$. At low temperatures the configurational entropy is negligible for all but the smallest cluster sizes and a ground state analysis is appropriate, i.e. the error is less than 2%. At temperatures above about 1100K, the deviation between the two approaches increases especially for small clusters: the difference is larger than 20% for 2<n<6 at 1600K! A persistent error of about 12% appears for larger sizes at about

1600K. As mentioned earlier, because the 35-vacancy cluster is a perfect octahedron (comprised entirely of (111) surfaces) this difference is expected to apply to all subsequent sizes.

The "phase" plot in Figure 2.15(b) provides a comprehensive view of the effect of configurational entropy in size and temperature space. The maximum discrepancy for small clusters at high temperature is critically important because small clusters are the primary species present during the early, high temperature stages of nucleation and growth of aggregates during silicon crystal growth. Thus, a ground state analysis of the thermodynamics of these species is incorrect at the temperatures relevant to nucleation.

At temperatures above about 1300K the difference between the ground state analysis and the present one persists at all sizes as mentioned above. The reason for this discrepancy is due to surface melting. Larger vacancy clusters are well approximated by internal (111) surfaces, which melt at a temperature substantially below the bulk melting temperature of 1685K. The (111) surface melting temperature predicted by the EDIP is approximately 1200-1300K, and above this temperature, a vacancy cluster at any size will exhibit some surface melting because of the extremely high density-of-states associated with off-lattice disorder created by this process. Surface melting at temperatures below the bulk melting temperature has important implications during the processing of the silicon wafers because it provides a pathway for cluster dissolution during wafer thermal annealing.

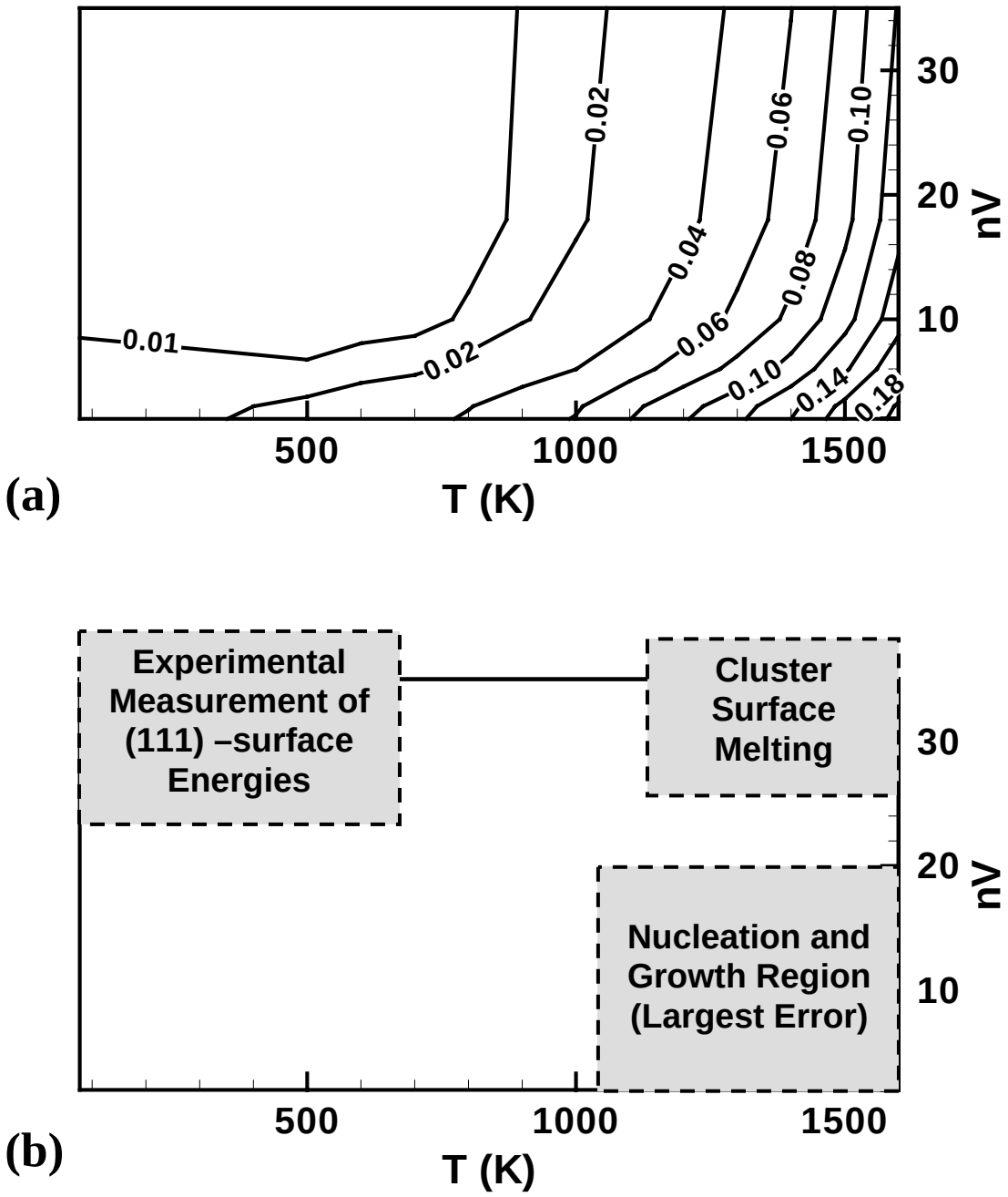

Figure 2.15: Difference ratio, $(\sigma_{HRC} - \sigma_{FULL})/\sigma_{FULL}$, between current ($\sigma_{FULL}$) and HRC ($\sigma_{HRC}$) surface free energy calculations.

2.5.3 Connections to Experimental Data

The heretofore-neglected contribution of the configurational entropy to vacancy cluster free energy is obviously important in the context of modeling microvoid formation during Czochralski (CZ) crystal growth. During this process, vacancy aggregation is initiated at high temperature because of vacancy supersaturation that results from crystal cooling. Continuum models for void formation have shown unequivocally that low (i.e. ~0.75-0.85 J/m^2) values of σ are necessary to predict the correct nucleation onset temperature (approx. 1350-1400K [112]). On the other hand it has been difficult to reconcile this range of values for the cluster surface free energy with experimental measurements of the (111) surface energy at 77 K, which are clustered around 1.25 J/m^2 [39, 65, 83]. As mentioned earlier, the (111) surface is widely considered as a good basis for estimating the free energy of experimentally observed octahedral voids, which consist almost entirely of (111)-oriented surfaces [82]. Our prediction for the effective surface free energy of the 35V cluster, which is entirely comprised of (111) surfaces, decreases from about 1.24 J/m^2 at 77 K to 0.82 J/m^2 at the experimental melting temperature of silicon, 1685 K.

Based on the present results, it is now possible to consolidate both values with a single result. The large clusters that are experimentally observed in commercial single-crystal silicon after cooling are unaffected by configurational entropy, and are well described by the (111) surface energy model (upper left region in Figure 2.15). However, early during the nucleation process, small clusters at high temperature are spatially extended due to a combination of configurational and vibrational entropy and are therefore characterized by

a much smaller surface free energy (lower right region in Figure 2.15**).** A single experimental data point available at 1685 K [153] provides a lowered (111) surface free energy (0.89 J/m^2) at high temperature (upper right region in, and further supports the validity of the present picture.

Finally, it should be noted that the excellent quantitative agreement between EDIP predictions and the experimental measurements in refs. [39, 65, 83, 153] is likely to be partially fortuitous. For example, EDIP under-predicts the melting temperature of silicon by about 10%, which may lead to comparable uncertainty in the predicted temperature dependence.

2.5.4 Explicit Configurational Entropy Calculations

While the configurational entropy is intrinsically taken into account in eq. (2.14), it is not possible to directly compute it from the total free energy. Rearranging eq. (2.4), the configurational entropy for a cluster is given by

$$TS_{conf} = \langle \Delta E \rangle - T \langle \Delta S_{vib} \rangle - \Delta G \tag{2.18}$$

which requires that the configurationally averaged formation energy and vibrational entropy be calculated. The former is directly obtained from the probability distribution functions. As mentioned in Section 2.1, the vibrational entropy of a given configuration was determined using the Quasi-Harmonic Approximation [76] following static relaxation at constant volume. The QHA was performed at 1000K for all configurations,

although it was determined that the QHA computed vibrational entropy did not depend on temperature over a large range.

The configurationally averaged vibrational entropy of formation was computed by repeated QHA analysis for a wide range of configurations (and formation energies) at each cluster size. Figure 2.16 shows the plot of vibrational entropy for 10V and 18V as a function of formation energy of different configurations spanned by each cluster.

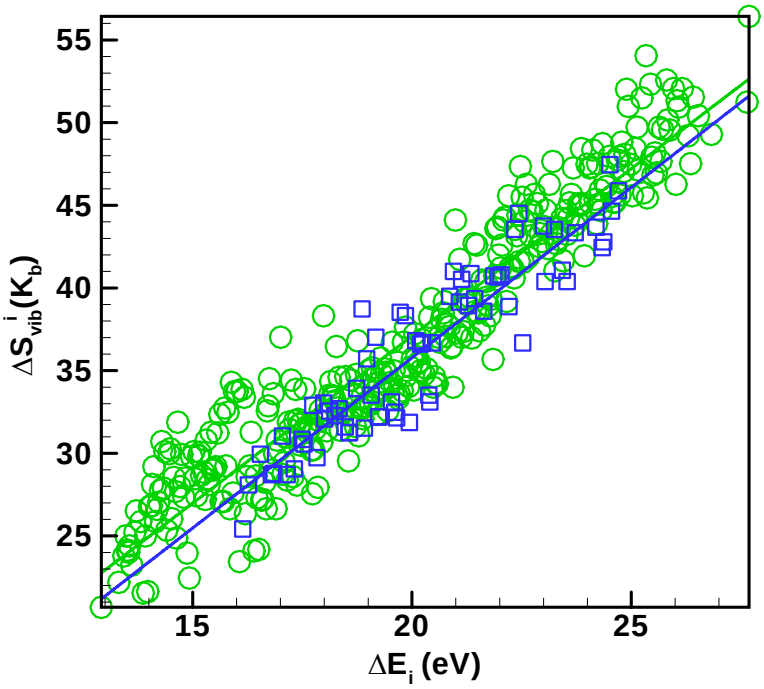

Figure 2.16: Vibrational Entropy as a function of formation energy of various configurations for 10V (circles), 18V (squares) clusters. Lines represent the linear fit to the data.

The resulting formation entropies for each cluster size were then fitted to linear functions of formation energy and the configurational average computed as

$$\left\langle \Delta S_{vib} \right\rangle = \sum \Delta S_{vib}^{i}(\Delta E_i) \times p'(\Delta E_i) \tag{2.19}$$

where $p'(\Delta E_i)$ is the normalized probability distribution function for the formation energies and $\Delta S_{vib}^{i}(\Delta E_i)$ represents the functional dependence of the formation vibrational entropy on the formation energy. The final average contribution of vibrational entropy to the free energy, i.e. $T\left\langle \Delta S_{vib} \right\rangle$ was fitted as a power law,

$$T\left\langle \Delta S_{vib} \right\rangle = a\, n^{2/3} + b \tag{2.20}$$

for different cluster sizes n, where coefficients a and b are function of temperature, and are listed in Table 2.1

Table 2.1: Power law coefficients a and b as a function of temperature for average vibrational entropy contribution to the total free energy

T (K)	a	b
500	0.28	-0.28
600	0.31	-0.31
700	0.36	-0.36
800	0.43	-0.43
900	0.52	-0.52
1000	0.54	-0.54
1100	0.65	-0.65
1200	0.715	-0.715
1300	0.79	-0.79
1400	0.88	-0.88
1500	0.99	-0.99
1600	1.13	-1.13

The temperature dependence of the configurational entropy contribution to the free energy is shown in Figure 2.17 for several cluster sizes. As the cluster size increases, the temperature dependence becomes stronger. Note that at low temperatures, the total configurational entropy for the smaller clusters is larger than that of the larger clusters, but the trend is reversed at high temperature because of the stronger temperature dependence. In fact, in the case of the 35V clusters the entropic contribution to the free energy is negligible below about 1000K. These trends can be explained by the fact that although larger clusters require more thermal energy to substantially fragment because they are more tightly bonded they have a much larger configurational space to explore once sufficient energy is provided.

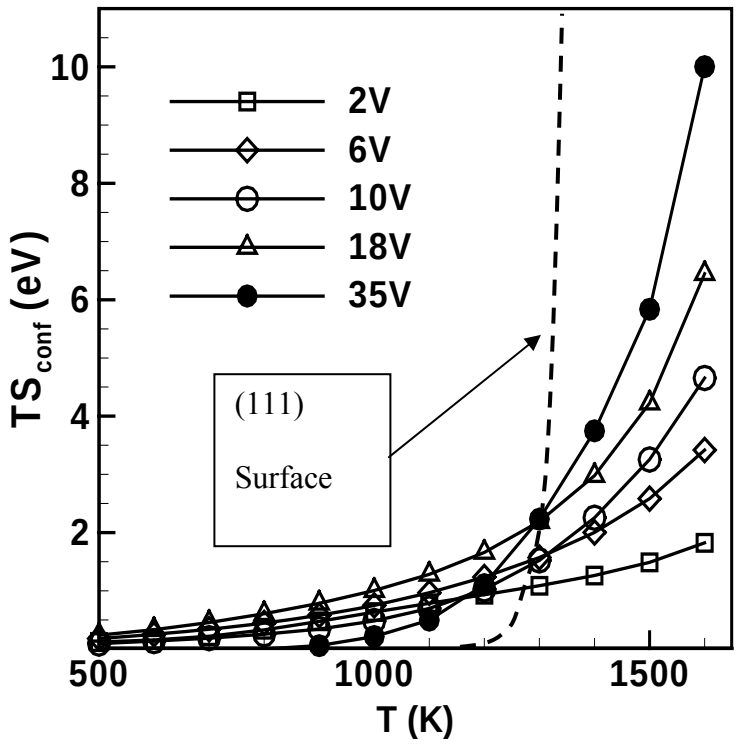

Figure 2.17: Configurational entropy contribution to the free energy of formation as a function of temperature for various cluster sizes. Dash line – limiting behavior for (111) surface melting.

Also shown in Figure 2.17 is the expected limiting behavior for large clusters. The onset of the sudden explosion in the configurational entropy corresponds the melting of the internal (111) surfaces. This picture further supports the hypothesis presented in Section 2.5.2.

2.5.5 Effect of Off-Lattice States on Single Vacancy

The thermodynamics of the single silicon vacancy have been studied numerous times using a wide variety of computational methods. Here we demonstrate that the configurational entropy picture presented in the previous sections can even influence the properties of single point defects. This is a surprising result because the single vacancy thermodynamic properties are generally assumed to be well described by a single ground state. The single-vacancy probability distribution and density-of-states functions for the formation energy are shown in Figure 2.18.

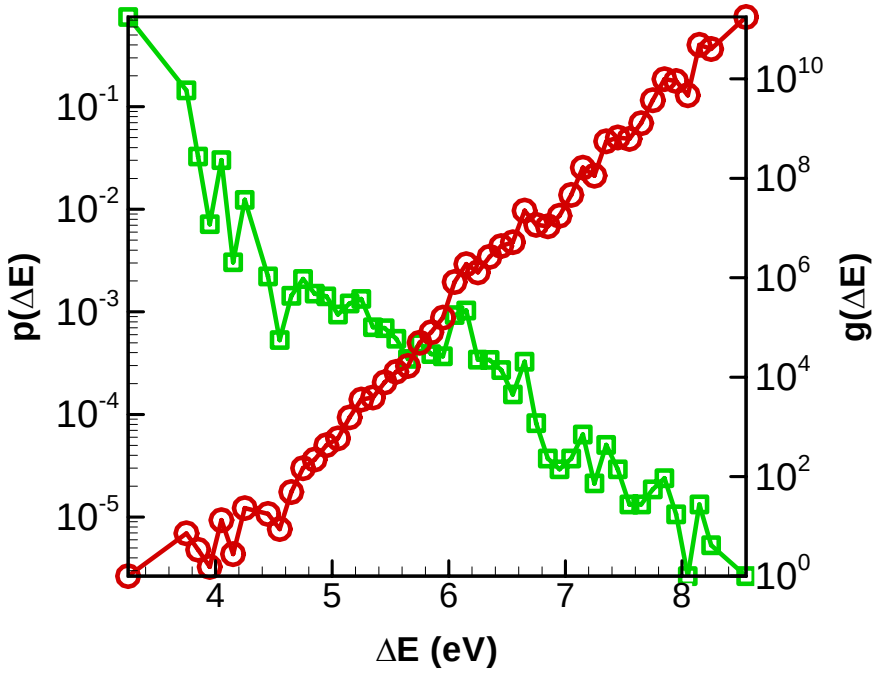

Figure 2.18: DOS (circles) and PDF at 1600K (squares) for the single vacancy.

As in the cluster case, a distribution of formation energies are found, ranging from the ground state value of 3.25 eV found in earlier work with the EDIP potential [122], to values as high as 8 eV which correspond to the additional formation of an interstitial-vacancy complex. While the probability distribution is strongly peaked at the ground state configuration, the total contribution of the first few higher energy states is about 20% of the ground state free energy! This corresponds to a temperature dependent shift in the predicted equilibrium concentration of about 100% at 1600K. Given that the contributing excited states are at only slightly higher energy relative to the ground state, this effect persists as the temperature is lowered.

These results suggest that many defects at high temperature should be characterized thermodynamically as a collection of non-degenerate states, rather than a single ground-state structure. The dense PEL induced by larger structures leads to substantial amorphization, but even single point defects introduce enough states to cause deviation from ground state thermodynamics. In fact, the present approach even can be applied to the perfect crystal, which can be considered to be the ground state configuration in a sequence of progressively higher energy states. This was examined by performing extended MD simulations of a perfect crystal with periodic minimizations. The DOS for the perfect crystal (not shown) indicates that at least one excited state (2.5eV above the ground state) is accessible by direct MD at 1600K. Inspection of the lattice corresponding to this configuration shows that the local minimum corresponds closely to the so-called four-fold coordinated defect recently identified with DFT calculations [67], which was also found to have formation energy of 2.5eV. This correspondence serves to

highlight the generality of the physical picture presented here as well as ability of the EDIP potential to accurately identify and model bulk defects in silicon.

2.5.6 Comparison to Tersoff Empirical Potential

A final test of the generality of our results was performed using the Tersoff potential for silicon. The probability distribution functions for the 6V and 10V clusters at 2700K in Tersoff silicon are shown in Figure 2.19.

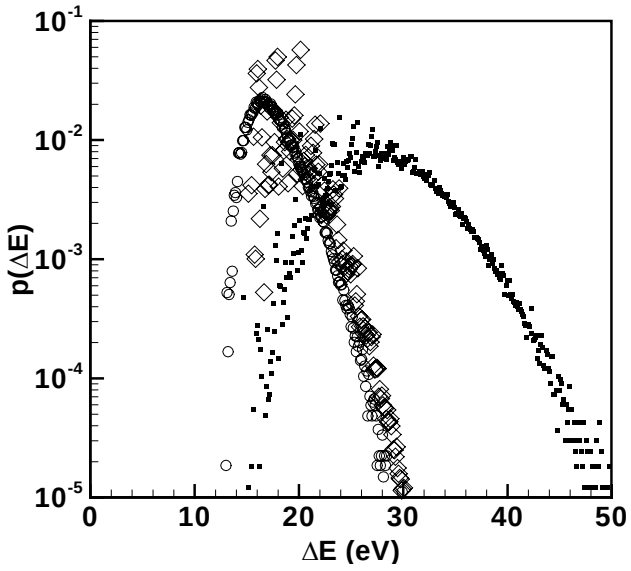

Figure 2.19: Probability distribution function for the 10V cluster. (a) Solid squares – Tersoff potential at 2700K, (b) open diamonds – Tersoff potential at 2650K, and (c) open circles – EDIP potential at 1600K..

This temperature corresponds very roughly to 1600K within the EDIP framework as determined by matching single vacancy diffusion coefficients. A similar picture is obtained in which both clusters are characterized by a distribution of states that are significantly higher in energy than the ground state configuration.

Also shown in Figure 2.19, (open symbols) is the EDIP probability distribution function at 1600K and the Tersoff distribution rescaled to a temperature of 2650K. Note how the small temperature shift leads to a large change in the probability distribution function and the Tersoff distribution function at 2650K is now very close to EDIP curve confirming the reproducibility of the physics across interatomic potentials. On the other hand it is difficult to resolve vacancy diffusion coefficients at 2650K and 2700K because of scatter in experiments. In other words temperature matching using single vacancy diffusion coefficient essentially gives the same result as matching the probability distribution curves and in fact demonstrates the universality of the present results with respect to choice of interatomic potentials..

2.6 Cluster Capture Radius

The only other piece of information that is required to make direct correlation to experiments using a process scale model is the capture radii of vacancy clusters. It has been shown by Prasad and Sinno [121], that the traditional definition based on compact cluster morphology grossly underestimates the cluster evolution at high temperature. In this section we use the detailed large scale MD simulation to estimate the high

temperature cluster morphology as a function of size, and is compared directly to compact cluster morphology.

2.6.1 Cluster Morphological Estimation

In all the crystal growth process models, the radius of each cluster is estimated by assuming that the cluster was a compact sphere (or a regular octahedron) with volume equal to the total number of vacancies in the cluster, *n*, multiplied by atomic volume, V_{vac}. The total capture radius of this "compact" cluster, $R^{tot}(n)$, included one additional bond-length, δ, so that

$$R_{compact}(n) = \left(\frac{3}{4\pi} n V_{vac} \right)^{\frac{1}{3}} + \delta \tag{2.21}$$

While this capture radius model is reasonable for large (i.e. mesoscopic) clusters at low temperature, it provides a substantial underestimation of the effective size of small, high-temperature clusters [122] such as the one shown in the inset of Figure 2.8.

An effective capture radius for each cluster size was calculated using extended MD simulations for a series of clusters in the size interval $1<n<500$. During each simulation, cluster size information was sampled periodically using the following approach. First the atomic coordinates were quenched to the local minimum energy configuration to remove thermal fluctuations. The (zero temperature) displacement of each atom from its nearest equilibrium position was then computed by comparing the

quenched lattice to a reference lattice. The cluster was defined as the union of all atoms that were displaced from their lattice sites by more than a threshold distance, β which is discussed further below. Note that only configurations that led to a topologically connected displacement field were counted. An effective cluster radius was computed from this data by assuming that each cluster configuration is spherical and then taking the average of the sampled radii so that

$$R_{avg} = \left\langle \left(\frac{3V(\beta)}{4\pi} \right)^{1/3} \right\rangle \tag{2.22}$$

where $V(\beta)$ is the volume of all atoms displaced by at least β from their equilibrium positions.

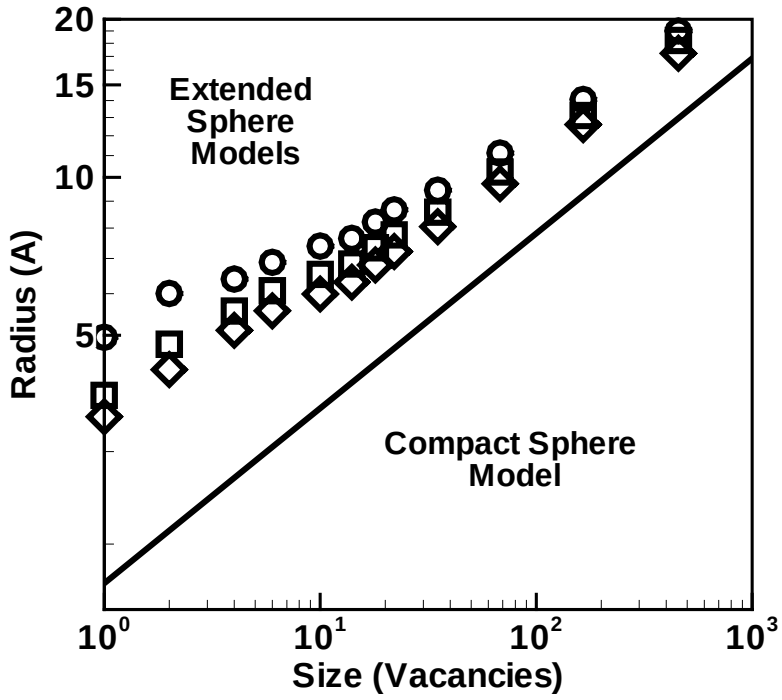

Figure 2.20: (a) Effective Cluster capture radius as a function of number of vacancies for various displacement threshold values: $\beta = 0.178$ Å (diamonds), $\beta = 0.136$ Å (squares), and $\beta = 0.08$ Å (circles).

The cluster capture radii predicted at 1600 K by eq. (2.22) are shown in Figure 2.20 as a function of the number of vacancies in a cluster for several values of the displacement threshold, β. The range of β values considered in Figure 2.20 is based on previous calculations of the vacancy-vacancy interaction distance [122] and $\beta = 0.08$ Å was used in all simulations presented in previous sections. Also shown in Figure 2.20 is the cluster capture radius predicted by eq.(2.21), denoted here as the "Compact Sphere Model". The effects of entropic expansion are most apparent for small clusters, but all sizes considered are somewhat extended by about a constant amount at this temperature.

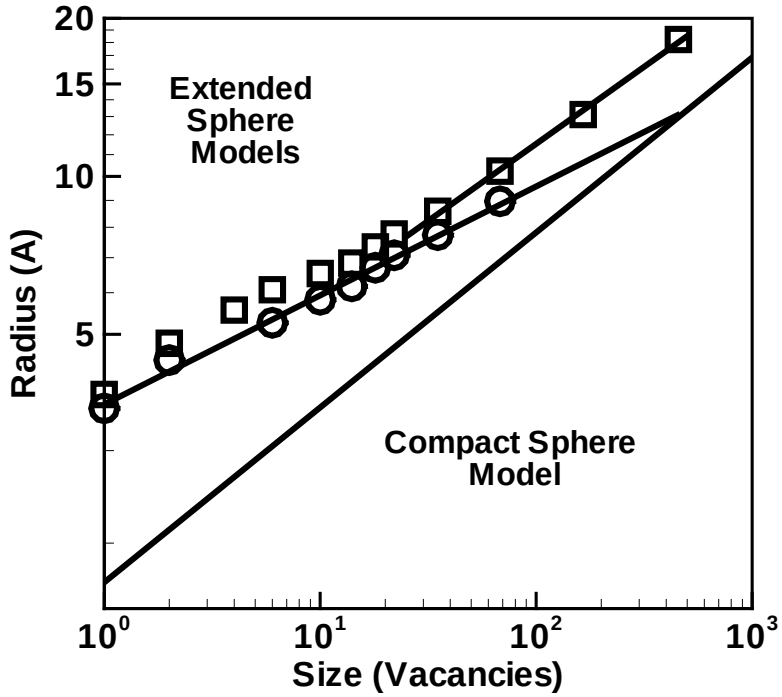

Figure 2.21: Temperature dependence of the cluster capture radius for $\beta = 0.136\,\text{Å}$: T=1600K (squares) and T=1300K (circles). Solid line represents the capture radius assuming compact spherical morphology (eq. ((2.21)).

The temperature dependence of the cluster capture radii is examined in Figure 2.21. While at 1600K all cluster sizes are extended, at 1300K there is a tendency for clusters to become more compact as the number of vacancies increases and extrapolation of the apparent power-law for the 1300K data shown in Figure 2.21 indicates that the compact geometry is approached for clusters larger than about 100 vacancies. This qualitative difference can be explained by the fact that the (111)-surface melting

temperature lies somewhere in between 1300K and 1600K – in the latter case, even large clusters (which are essentially internal (111) surfaces) are extended because their surfaces are destabilized. A schematic summary of the morphological evolution of clusters as a function of size for temperatures below the surface melting point is shown in Figure 2.22.

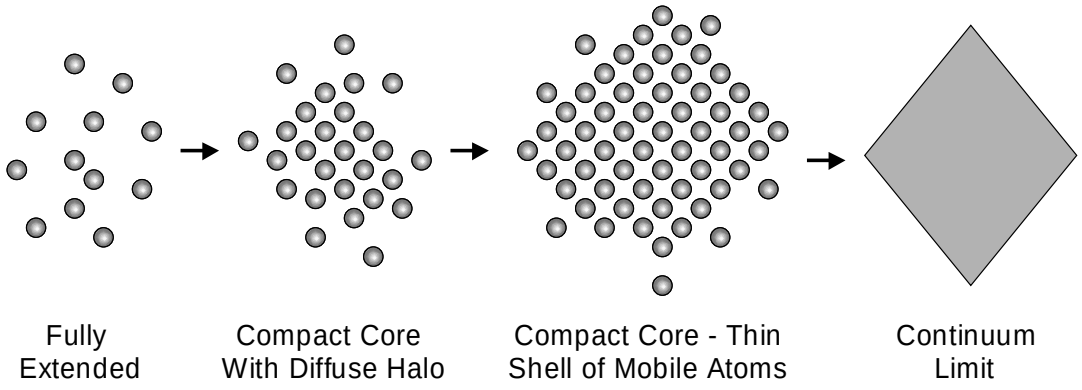

Figure 2.22: Morphological evolution of vacancy clusters as a function of size for temperatures below the surface melting point.

2.7 Conclusion

We have demonstrated that configurational entropy is a qualitatively important contribution to the thermodynamic properties of atomic clusters in crystalline solids, particularly at elevated temperature. The magnitude of this entropic source is strongly underestimated if a lattice-based approach is used because of the presence of an unexpectedly large number of off-lattice local minima in the potential energy surface. The present calculations suggest that any lattice defect should be interpreted as a dense

collection of non-degenerate states, in which the ground state may or may not be relevant at high temperature, which is a fundamentally different view than the traditional approach of basing finite temperature property calculations on the minimum energy structure.

The thermodynamics and structural properties of vacancy clusters, estimated in this work have been incorporated into the process scale models by Freewen et. al.[60, 61] The process scale model is able to reproduce the correct void size distribution, density and nucleation temperature for numerous crystal ingots of different radii grown under a wide range of cooling conditions. The previously neglected configurational entropy is demonstrated to qualitatively alter the nature of small clusters at the high temperatures where nucleation and growth are important. In addition to accurately modeling void formation, the EDIP-derived thermodynamic properties used for vacancy clusters in this work are, for the first time, shown to be entirely consistent with experimental measurements of the silicon (111) surface free energy without the need for adjustable parameters.

The overall picture presented here for the crystalline silicon system is shown to be independent of the empirical potential or the type of defect cluster, and suggests that the computational approach and results presented here should be generally applicable to other solid-state systems. Our results also have implications for multiscale modeling approaches in which molecular dynamics simulations are used to compute properties for coarser models such as on-lattice kinetic Monte Carlo. The loss of degrees of freedom in the latter implies that the configurational entropy associated with the off-lattice states is lost and will substantially alter the thermodynamic properties of the system. Using the inputs from high temperature MD simulations (as carried out in this work), Dai et al [42]

have constructed a lattice kinetic Monte Carlo model that implicitly captures the configurational entropy associated with off-lattice defect configurations.

3 Atomistic Simulations of Self-Interstitial Aggregation

The ion-implantation process, which is used to introduce dopants (e.g. boron or phosphorous) into a silicon wafer, results in a highly non-equilibrium distribution of point defects (self-interstitials and vacancies) and their clusters.[87, 145] While many of these defects recombine almost instantly, a large supersaturation of self-interstitials is typically left behind because of the net excess atoms present within the lattice following implantation, creating a distribution of interstitial clusters.[87, 89, 145] These clusters are now well known to strongly affect the diffusion behavior of the implanted dopant atoms during the subsequent implant damage annealing[23, 25, 29, 32, 44, 88, 142, 158] that is required to heal lattice damage and electrically activate dopant atoms. The diffusion effect is commonly referred to as transient-enhanced diffusion, or TED, because of its strongly non-linear and time-dependent features.[33] Qualitatively, TED is observed because excess self-interstitials effectively increase the mobility of dopant atoms via the "kick-out" mechanism by increasing the fraction of time the latter spend in the mobile interstitial state rather than the immobile substitutional one.

Self-interstitial clusters have been somewhat more difficult to fully characterize than their vacancy-related counterparts, which are commonly found in vacancy-rich Czochralski-grown silicon crystals.[59, 61, 62, 134] While the latter tend to form predominantly

octahedral structures bounded by {111}-oriented planes and with 50-200 nm length scales,[81, 120] self-interstitial clusters have been observed in a variety of different sizes and morphologies. In particular, it has been challenging to connect quantitatively the implantation and annealing conditions to the observed morphologies, several of which may be present simultaneously.[44, 74, 88, 89, 106, 107, 116-118, 142, 158] As a result, there have been numerous studies aimed at experimentally and computationally characterizing the structure, thermodynamics, and dynamical evolution of self-interstitial clusters in crystalline silicon.

The Ion Implantation Group at CNRS[28], in perhaps the most comprehensive publications on the subject, have summarized much of the phenomenology associated with self-interstitial clusters and TED in silicon. An important contribution of the work in refs.[26-28] was to unambiguously demonstrate that the supersaturation of self-interstitials present during TED resulted from a complex combination Ostwald ripening of clusters, out-diffusion of self-interstitials to the wafer surface, and a thermodynamic competition between the various possible cluster morphologies. Earlier studies suggested that the sole source of the excess silicon self-interstitials are dissolving {113}-oriented planar defects formed during the post-implant annealing, which first grow to some maximum size then dissolve during annealing to release mobile Si self-interstitials. The work in refs.[26-28], however, shows that TED is operational even during cluster ripening (growth), and that it is the supersaturation of single self-interstitials in the vicinity of the clusters that is maintained by the Gibbs-Thompson effect which is responsible for TED. Moreover, it was demonstrated that a quantitative description of the

ripening dynamics required that several different cluster morphologies be considered, all of which have been observed experimentally in ion-implanted silicon wafers.

3.1 A Brief Overview of Observed Self-Interstitial Cluster Morphologies in Silicon

In the following section, we briefly summarize the salient features of the various self-interstitial cluster morphologies that have been observed experimentally to date. It should be emphasized once again that the dominant self-interstitial cluster structure found in a particular sample depends strongly on the implant type (i.e. silicon or boron ions, electron irradiation), implant energy and dose, and length and temperature of the post-damage anneal. There are two classes of planar defects commonly found in ion-implanted Si; those that lie on planes normal to the <113> directions, and those that are normal to <111>. These defects are commonly referred to as {113} and {111} defects, respectively, and are often visible simultaneously.[24, 50, 51, 70]. Figure 3.1 shows high-resolution transmission electron microscopy (HRTEM) image of interstitial aggregates created in silicon during in situ-electron irradiation at room temperature.

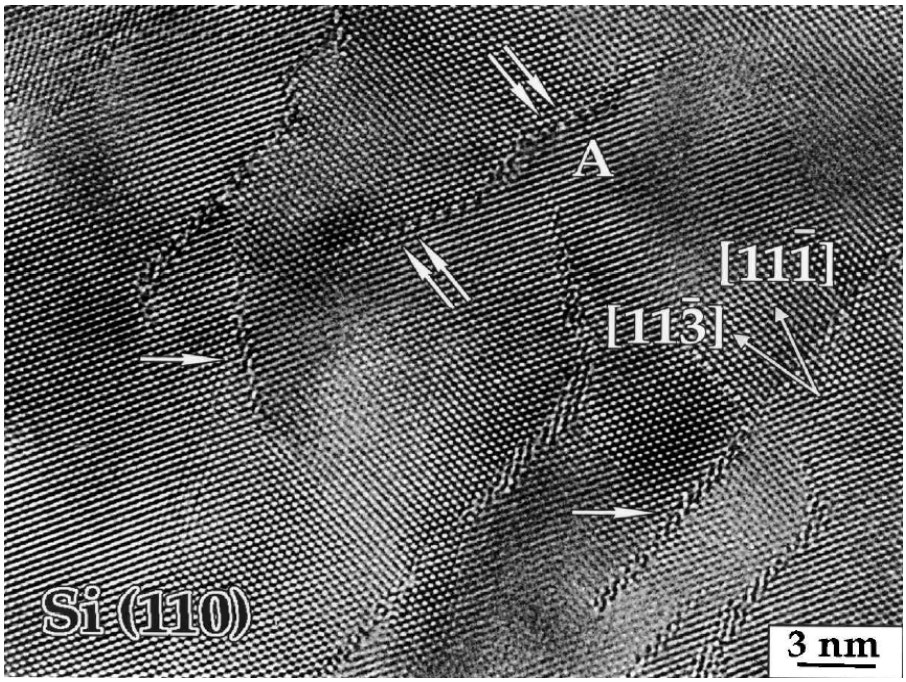

Figure 3.1: HRTEM image of interstitial aggregates created in silicon during in situ-electron irradiation at room temperature. The {113} and {111} defect are marked with single and double arrow [50].

The {113} and {111} defect are marked with single and double arrow. The {113} defects have been the subject of intense investigation because of their uniqueness to Si and Ge, as well as the difficulty associated with their complete atomistic characterization. Their atomistic structure was deduced by Takeda,[143] who showed using HRTEM in Figure 3.2 that these defects are comprised of <110>-oriented interstitial chains aligned in the {113} habit plane.[70, 143]

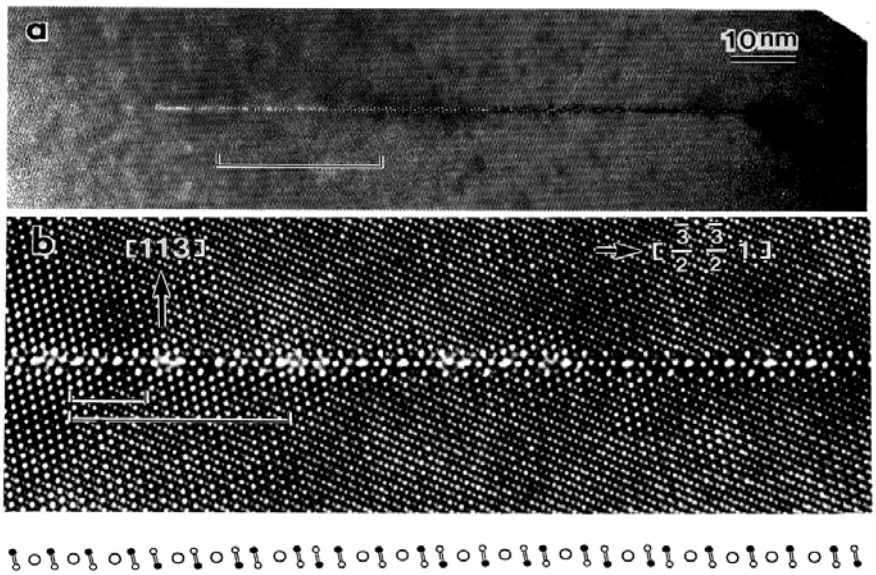

Figure 3.2: HRTEM image of {113} defect in (a), enlarged picture of marked line in (a) is shown in (b). The small open and solid circles represent the interstitials, separated by large open circles (8 membered rings) [34]

Images taken during the early stages of {113} defect (see Figure 3.3) formation indeed show the presence of line interstitial defects (LIDs), which correspond to chains of di-interstitials aligned along the <110> directions.[96, 100, 143] LIDs are surrounded by five, six and seven-membered silicon atom rings. It is believed that these LIDs are the building blocks for planar {113} defects.[70, 96] Growth of LIDs along <110> is energetically favorable relative to assembly in the {113} plane because of the lack of dangling bonds at the LID ends. As a result, ion-implanted Si samples often exhibit a preponderance of rod-like {113} defect morphology but both the rod-like and planar structures are believed to originate from the same process.

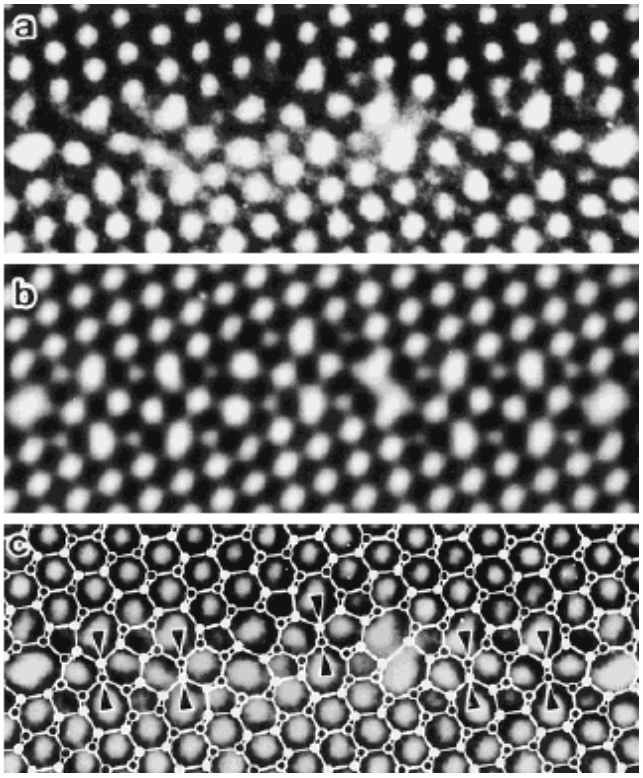

Figure 3.3: A HRTEM observation of single LID (a) HRTEM Image (b) atomic simulated image (c) atomic model superimposed on the HRTEM image. The middle arrowheads represent single LID. Also shown in (c) are two double-LID (two side-by-side single LID)[46]

One complicating factor in the analysis of {113} defects is that the spacing between LID building blocks is not necessarily regular, leading to non-periodicity in the {113} plane and a variable interstitial density.[96] The notation /I/, /IO/, /IIO/, etc. is commonly employed to represent the presence (I) and absence (O) of di-interstitial rows (I) in a particular {113} defect (see Figure 3.4). As expected, the formation energetic and interstitial density of a {113} defect are functions of the specific configuration.[24, 70, 96]

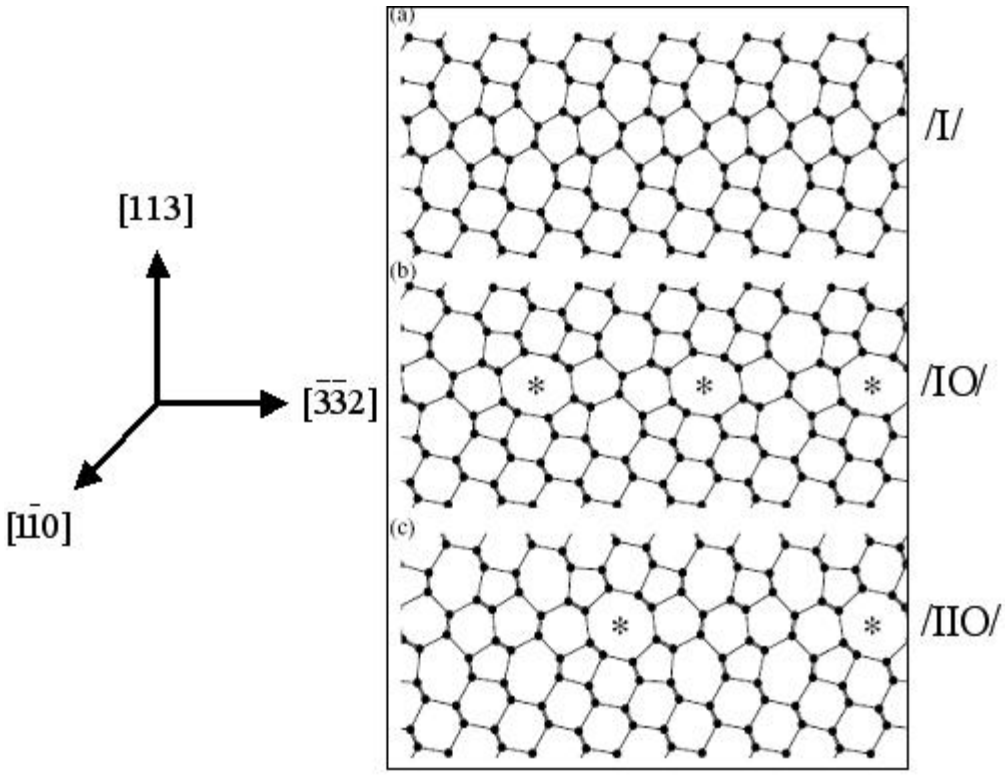

Figure 3.4: Schematic representation of various configurations of {113} based on different arrangements of /I/ and /0/ repeat units. (a): shows /I/ structure where the I chain occurs repeatedly, (b): shows /IO/ structure, where the every I chain is separated by an empty 'O' chain.; (c) /IIO/ structure where 'O' chain separates a pair of 'I' chains. Asterisks or eight membered rings represent 'O' chains in above figure. [48]

The most common {111} planar defects observed in implanted silicon are the Frank partial (FDL) and the perfect dislocation loops (PDL).[116-118] Both planar defects are surrounded by dislocation loops, while the Frank partials also include a stacking-fault comprised of two additional (111) planes of atoms. Under TEM, these defects often appear as either filled (Frank partial) or open (perfect) oval-shaped structures. FDLs are characterized by a dislocation with a {111}-oriented burgers vector, while the PDLs possess dislocations with a [110] burgers vector (see Figure 3.5). These

defects are acknowledged to be the most energetically stable interstitial aggregates in the limit of large sizes; after long time annealing of post-implanted wafers they are generally the only defects remaining.[28]

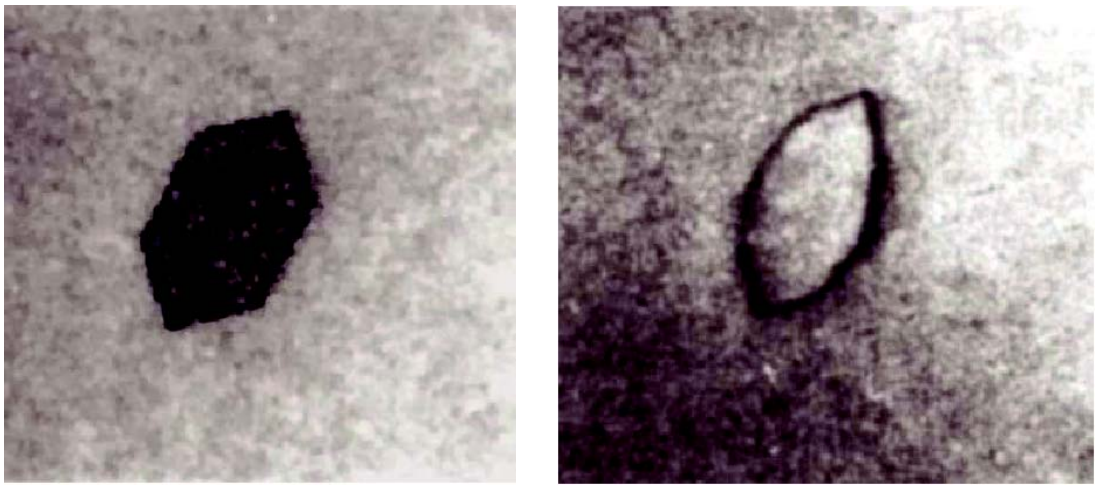

Figure 3.5: TEM of Frank Dislocation Loop (left), and Perfect Dislocation Loop (right). [116-118]

Another type of {111}-oriented defect are the so-called {111} rod-like defects. These structures are significantly less common than the {113} rods (LIDs) but have been experimentally observed in silicon following irradiation.[50, 51] They are characterized by a {111}-oriented chain of interstitials surrounded by alternating five and eight-membered atomic rings as shown in Figure 3.6. Interestingly, electronic structure calculations based on density functional theory (DFT) predict them to be more

energetically favorable than the {113}-oriented rods [70, 72] and additional factors beyond simple energetic are thought to be responsible for their relative scarcity.

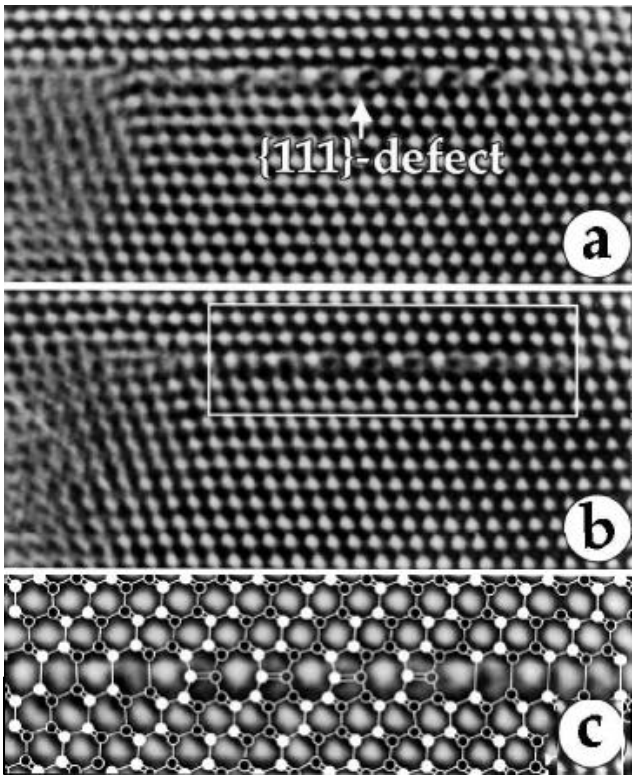

Figure 3.6: HRTEM image of {111}-defect after (a) 30, (b) 35 min irradiation (c) HRTEM superimposed atomic image based on rectangle in (b). [33]

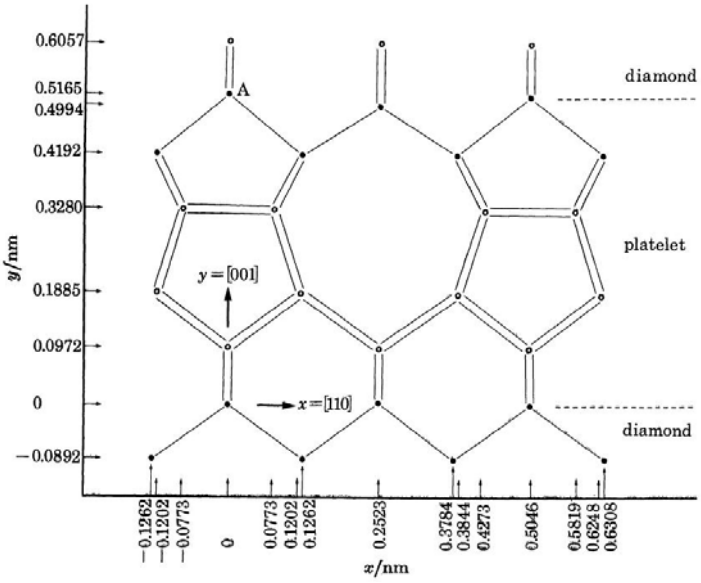

Figure 3.7: A {100} defect based on Humble/Arai 4I structure [52].

Finally, we mention briefly {100}-oriented planar defects.[70, 78] These defects are comprised of {100} planar arrays of the well-known Humble/Arai[9, 31, 78, 102] four-interstitial cluster structure (see Figure 3.7). They are generally not observed in silicon, although have been extensively studied in diamond [78] and germanium.[111] Some evidence for their presence in silicon has been gathered following high-dose boron implantation,[38] but it is thought that the boron may play an important role in this case and that the observed {100} defects are examples of boron-interstitial clusters, or BICs (see Figure 3.8). Once again, it is not clear why pure {100} interstitial defects are not generally observed during damage annealing of silicon given that DFT calculations show them to be at least as energetically favorable as {113} defects.[70]

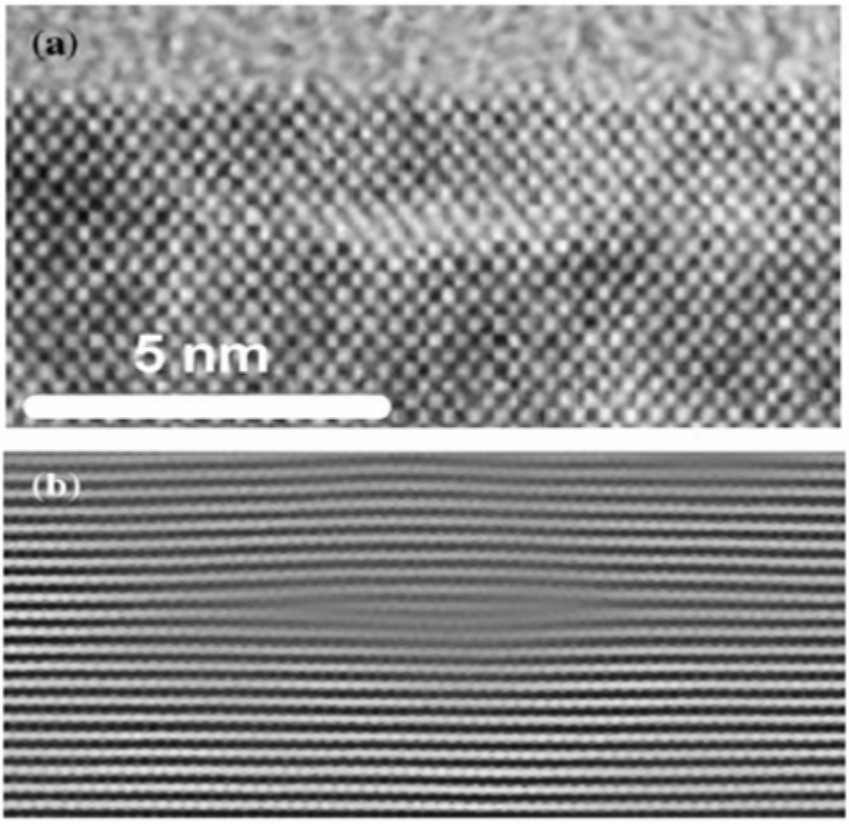

Figure 3.8: HRTEM image of {100} loop under high Boron implant. Vertical Axis is [100]. [55, 56]

Our goal is to first apply the large-scale atomistic simulations based on empirical interatomic potentials in order to directly study the aggregation and growth of self-interstitial clusters under highly supersaturated conditions. Then, we aim to study the thermodynamic properties of individual clusters in order to explain mechanistically the observations in the direct aggregation simulations. We seek to address issues related to how the various cluster morphologies are related, and what the effects of temperature and hydrostatic pressure on these relationships are. These questions are posed with two

primary computational approaches. In this chapter, direct large-scale molecular dynamics simulations of self-interstitial aggregation are performed under prescribed temperature and stress conditions. These simulations provide a detailed transient view of the aggregation process and the resulting aggregate morphologies as a function of temperature and pressure. The results from the large-scale simulations are analyzed in Chapter 4 by studying the thermodynamics and morphology of single clusters using a computational method that we have recently developed in Chapter 2 and applied to the characterization of vacancy aggregates.[92] In this approach, the cluster configurations generated by lengthy molecular dynamics (or equivalently Monte Carlo) simulations are sampled periodically to generate a probability distribution for the formation energies. The formation energy distribution function is directly related to the total classical formation free energy of the cluster, and provides a comprehensive view of cluster thermodynamics at finite temperature and stress. In aggregate, the results of both simulation approaches are combined to infer a comprehensive picture for self-interstitial aggregation.

The remainder of this chapter is structured as follows. In the section 3.2, we discuss the methodological details of the large-scale direct aggregation simulations. In section 3.3, the results of simulations based on the Environment-Dependent Interatomic Potential (EDIP)[14] are presented and discussed in detail. Both temperature and pressure effects are considered. In Section 3.4, additional results are presented using other interatomic potential functions for silicon. These are compared and contrasted to the EDIP results to generate a consistent qualitative picture of the self-interstitial aggregation process. Conclusions are presented in Section 3.5. In Chapter 4, single cluster thermodynamics are probed in detail using techniques for sampling the potential energy

landscape associated with the clusters. These calculations provide a detailed mechanistic view of the effects of temperature and pressure on self-interstitial aggregation and suggest possible explanations for experimental observations.

3.2 Simulation Methodology for Large-Scale Simulations of Interstitial Aggregation

A sequence of parallel molecular dynamics (PMD) simulations were performed using large cubic simulation cells consisting of 39,304-1,000,000 silicon lattice atoms along with 216-1,000 silicon self-interstitials, initially placed in uniformly-spaced tetrahedral positions. While this initialization procedure obviously does not correspond directly to a post-implantation configuration, it does provide a highly supersaturated environment that leads to rapid aggregation. Variations in the initial interstitial positions were not found to provide appreciable effects in the evolution of aggregates, except at extremely short simulation times. The codes and simulation initialization approaches used in these simulations have been adapted from Prasad and Sinno.[121, 122]

The empirical EDIP potential[14] was used in most of the simulations discussed below, but a subset of the runs also were carried out with the Stillinger-Weber (SW)[139] and Tersoff[147] potentials for silicon. Constant-pressure/constant temperature (NPT) PMD simulations at various temperatures and pressures were carried for several nanoseconds (3.8 ns to 38 ns), using the Parrinello-Rahman method[119] to control pressure, and velocity rescaling to control temperature. NPT simulations were performed with hydrostatic pressures ranging from -3GPa to +3GPa and temperatures raging from 1000K

to 1400K (for the EDIP runs – other temperatures ranges were employed for the SW and Tersoff potentials as discussed later in section 3.4). The 5th-order Gear predictor-corrector method with time steps of 1.0-3.2 fs was used to integrate the particle trajectories; convergence of the simulation results with respect to the time step size was checked in each case using short test simulations.

During the course of the PMD simulations, the entire system was quenched periodically to the local minimum energy configuration using a conjugate gradient minimization technique[64] and compared to a reference perfect crystal in order to identify the locations of self-interstitials as a function of time. The unambiguous assignment of self-interstitials within a cluster is difficult because of the substantial local lattice distortion that involves many more atoms than the actual number of self-interstitials.[19] An approach introduced previously[91] is used to identify "defective atoms" (DAs) as those that are more than 0.2Å away from the nearest lattice site in the reference crystal. Once all DAs are identified, they are grouped into clusters based on the Stillinger criterion[137] with a connectivity distance equivalent to the 1st-nearest neighbor distance in the perfect silicon lattice. In each cluster, therefore, the total number of self-interstitials, is known, but the particular atoms that represent these interstitials is not; the self-interstitials are arbitrarily identified as the most displaced atoms. As will be shown, unique assignment of atoms as self-interstitials is not required to analyze cluster morphologies.

3.3 Direct MD Simulation of Self-Interstitial Aggregation – EDIP Results

Throughout the following discussion of direct aggregation simulations, simulation cells initialized with 216,000 lattice atoms and 1,000 self-interstitials were employed unless otherwise noted. Our base case simulation conditions were chosen to be T=1200K and P=0 and the PMD run was allowed to evolve up to 19.2 ns. Snapshots of quenched atomic coordinates at several times are shown in Figure 3.9. Large, dark (red) spheres represent self-interstitials as defined in Section 3.2, while the small, light (green) spheres are lattice atoms that are displaced from their ideal (i.e. perfect crystal) positions by more than 0.2Å. The latter represent a qualitative measure of the strain-field surrounding the self-interstitial clusters. All other atoms are deleted for clarity.

Several interesting features are apparent during the clustering process. First, small three-dimensional aggregates are quickly formed throughout the simulation domain (Figure 3.9a). These clusters grow by ripening (monomer exchange between clusters) and some coalescence due to small cluster mobility at this temperature. Note that at this stage, most of the atoms represent actual self-interstitials; i.e. relatively few atoms beyond the self-interstitials themselves are appreciably displaced from their ideal lattice positions. At time t~3.7 ns (Figure 3.9b), the largest of the three-dimensional clusters exhibits a rapid morphological transformation into a planar configuration oriented along the [111] directions. At even later times, more of the growing cluster transform to planar configurations and both {111} and {100}-oriented platelets are observed; Figure 3.9c.

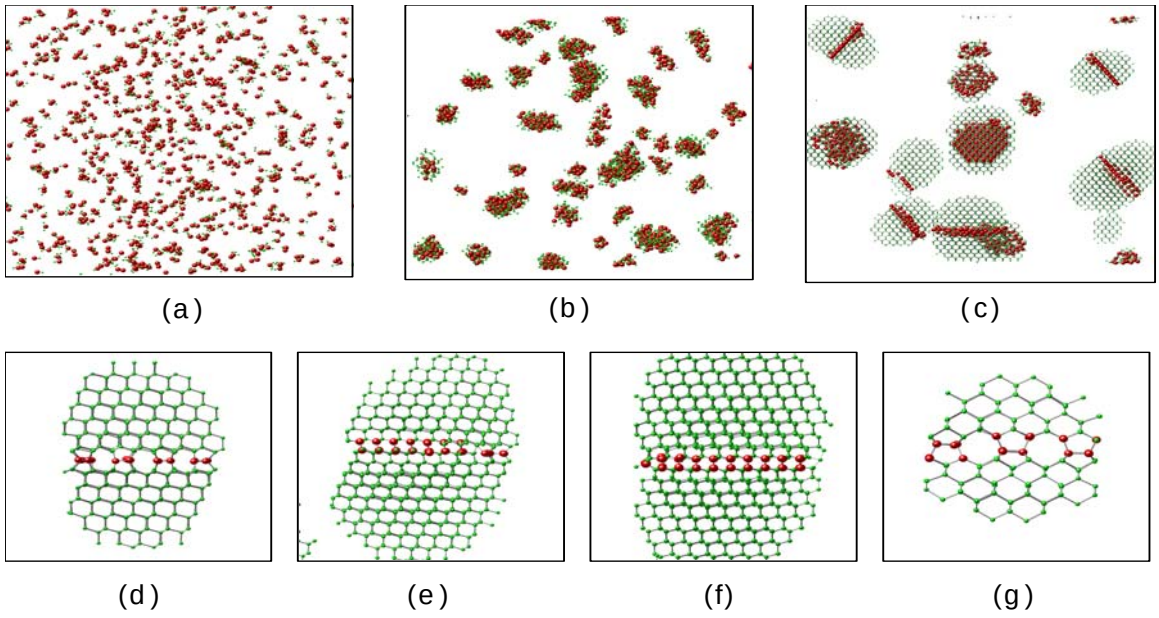

Figure 3.9: (a)-(c) System-wide evolution of interstitial cluster distribution at 1200K and zero pressure; (a) t=0.2ns, (b) t=3.7 ns, and (c) t=19.2 ns. Large (red) spheres denote self-interstitials; small (green) spheres show lattice atoms that are displaced by more than 0.2Å from their equilibrium positions. All other atoms are deleted for clarity. (d)-(g) Detailed view of cluster structures; (d) {111} RLD, (e) {111} PDL, (f) {111} FDL, and (g) {100} planar defect. All panels are oriented so that the horizontal direction is [110]. For figures (a)-(c) and (g), vertical direction is [001], for figures (d)-(e) vertical direction is [111].

Close-up views of the different platelet configurations generated during the simulation also are shown in Figure 3.9d-g. All three types of {111} defects discussed in Section 3.1 are observed: {111}-RLD (Figure 3.9d), a perfect dislocation loop (Figure 3.9e), a Frank partial dislocation loop (Figure 3.9f). In each case, the structure of the planar defect is in excellent agreement with previous literature models obtained by interpretation of TEM images.[24, 27, 28, 50, 51, 70, 77] The {100} planar defects (Figure 3.9g) are also in structural agreement with literature models [70, 78], although as noted earlier, {100} defects are not typically observed in implanted silicon samples. Note

that the strain field around the planar defects is three-dimensional and elongated in the direction normal to the plane of the defect. It is likely, therefore, that the capture volume is similarly shaped, and that the coarsening dynamics of these defects would be best described on the basis of spheres rather than two-dimensional plates. Evidence for this type of behavior has in fact been observed in previous experiments.[117] Although the progression is not obvious from the limited number of snapshots shown in Figure 3.9, we find direct evidence that the {111}-RLDs generally form first by direct collapse of three-dimensional aggregates and then grow to form FDLs and PDLs. It is also worth mentioning here that no evidence of other common defect structures, particularly {113} defects are observed at any stage of the evolution under the prescribed conditions.

Additional simulations performed at higher temperatures show that the collapse from three-dimensional to planar defect structures takes place at increasing sizes as the temperature is increased. Shown in Figure 3.10 and Figure 3.11 are snapshots from simulations performed at 1300K and 1400K, respectively. At 1300K, very large FDLs and PDLs are observed at a t=13.4 ns, while at 1400K no planar defects are apparent by the time the simulation is terminated at t=8.0 ns.

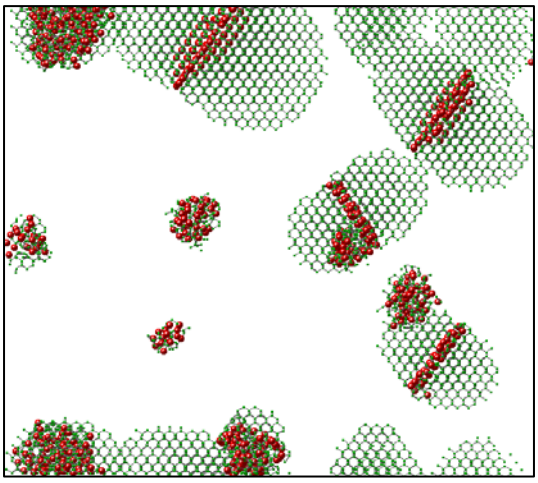

Figure 3.10: System-wide evolution of interstitial cluster distribution at 1300K and zero pressure. Total simulation time is 13.4 ns. Large (red) spheres denote self-interstitials; small (green) spheres show lattice atoms that are displaced by more than 0.2Å from their equilibrium positions. All other atoms are deleted for clarity. Horizontal direction is [110] and vertical [001].

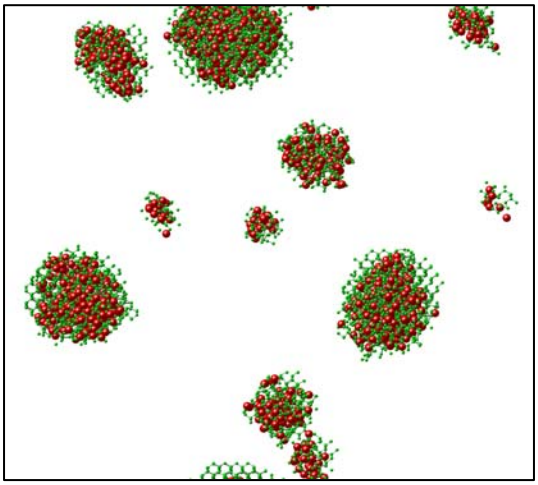

Figure 3.11 : System-wide evolution of interstitial cluster distribution at 1400K and zero pressure. Total simulation time is 8.0 ns. Large (red) spheres denote self-interstitials, small (green) spheres show lattice atoms that are displaced by more than 0.2Å from their equilibrium positions. All other atoms are deleted for clarity. Horizontal direction is [110] and vertical [001].

Using the data at several simulation temperatures (1000K-1400K), we can determine approximately the temperature dependence of the transition size at which amorphous three-dimensional structures collapse to any of the planar configurations; see Figure 3.12.

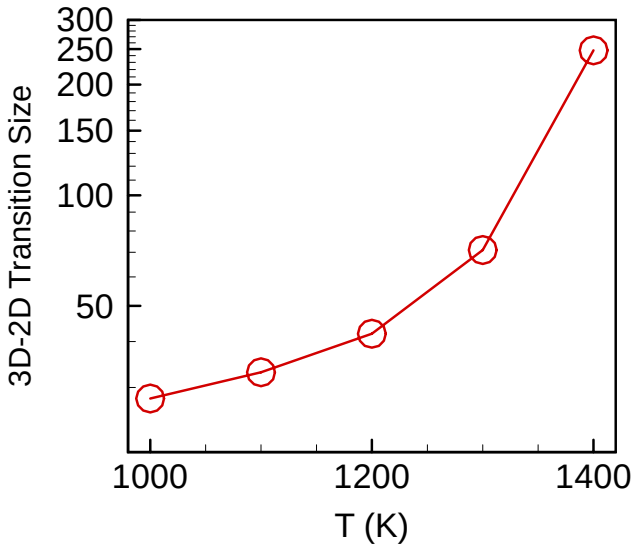

Figure 3.12: Average number of interstitials in clusters transitioning from three-dimensional to two-dimensional morphology as a function of temperature (zero pressure).

As will be discussed in more detail in the following section, the morphological transition from three-dimensional to two-dimensional structures is driven by a balance between the high stress and configurational entropy of the three-dimensional aggregates and the

relatively low energy of the planar defects. Note that the data in Figure 3.12 is approximate because additional interstitials are being incorporated into clusters during the period during which the 2D-3D is taking place. Finally, the lack of any {113} defects is notable; these are not predicted to form by the EDIP potential at any temperature in the range investigated. Test simulations with smaller systems at lower temperatures confirm this finding all the way to about 900K. Even lower temperature simulations were not feasible due to the slow mobility of interstitials.

3.3.1 Effect of Hydrostatic Pressure on the Aggregation Behavior of Self-Interstitials

Next, the effect of hydrostatic pressure on the self-interstitial aggregation behavior was investigated. Although substantial hydrostatic stress is not commonly present in silicon wafer processing, our purpose here is to study the generic influence of stress on defect thermodynamics and aggregation kinetics. Moreover, the transient evolution of the stress state in a wafer during and after ion-implantation is not fully understood; literature evidence exists for the presence of both tensile and compressive stresses that evolve in time, and these are strongly coupled to the dose, type and energy of the bombardment.[11, 12, 45, 124] Future studies will consider the effects of more complex stress distributions including biaxial and uniaxial fields, although some recent atomistic work has addressed the static effects of biaxial and uniaxial stress on individual defects.[17] Further discussion of these results in the context of the present calculations is presented in Chapter 4.

We begin by considering the effect of hydrostatic compressive stress on self-interstitial clustering at 1200K. A pressure of +3 GPa was applied to the simulation box, which produces a compressive (uniformly distributed) strain of approximately -1% in a perfect EDIP silicon crystal. As shown in Figure 3.13, the transformation between three-dimensional and planar defects is essentially inhibited over the time interval accessed by the PMD simulation (~10 ns). Although the transformation size from three-dimensional to planar morphology is about $n_I \sim 42$ at 1200K, several clusters larger than this size are observed to remain in the amorphous three-dimensional state. Otherwise, the three-

dimensional aggregates observed under compression are qualitatively similar to those observed at zero strain.

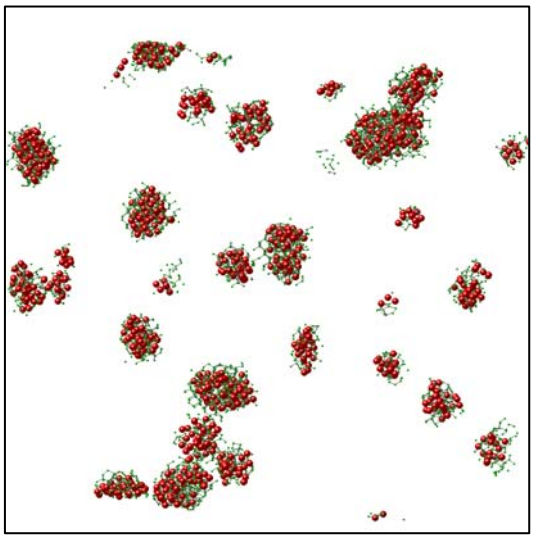

Figure 3.13: System-wide evolution of interstitial cluster distribution at 1200K and 3GPa pressure (approx. 1% compressive strain). Total simulation time is 9.6 ns. Large (red) spheres denote self-interstitials; small (green) spheres show lattice atoms that are displaced by more than 0.2Å from their equilibrium positions. All other atoms are deleted for clarity. Horizontal direction is [100] and vertical is [001].

The effect of tensile stress on the clustering process is much more profound and complex, as shown in Figure 3.14. In this simulation, a tensile hydrostatic pressure of -3GPa was applied at 1200K, resulting in a tensile strain of about +1%. Under these conditions, no {111}-oriented defects are observed to form throughout the entire simulation (~23 ns), although some small {100} defects are still formed.

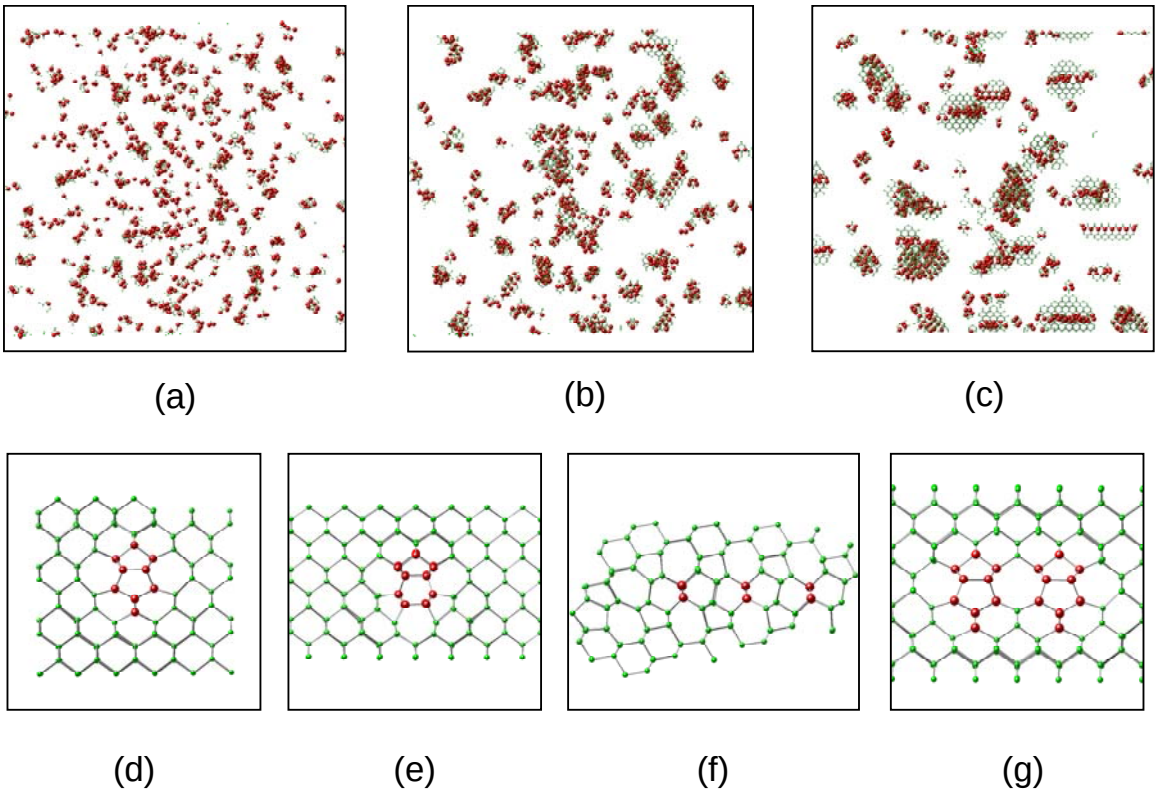

Figure 3.14: (a)-(c) (a)-(c) System-wide evolution of interstitial cluster distribution at 1200K and -3GPa pressure; (a) t=0.2ns, (b) t=4.3 ns, and (c) t=23.2 ns. Large (red) spheres denote self-interstitials; small (green) spheres show lattice atoms that are displaced by more than 0.2Å from their equilibrium positions. All other atoms are deleted for clarity. (d)-(g) Detailed view of individual cluster structures; (d) 4-intersitial Humble/Arai configuration, (e) partially reconstructed LID, a precursor to {113} defects, (f) {113} planar defect comprised of three <110>-oriented interstitial chains (shown), and (g) two Humble/Arai 4-interstitial clusters arranged to form a {100} planar defect. All panels except (f) are oriented so that the horizontal direction is [110] and vertical is [001]. In (f), vertical is [113], horizontal is $[\bar{3}\bar{3}2]$.

Notable qualitative changes relative to the corresponding zero pressure simulation are that the average cluster size is significantly smaller at all times, and that at early and intermediate times (Figure 3.14a,b), a large number of 4-interstitial complexes are present throughout the simulation domain. Closer inspection of the 4-interstitial complexes

(Figure 3.14d) shows that they are exclusively in the well known cage-like configuration that has been identified as the energetic ground state for the 4-intersitial cluster in several previous theoretical studies[15, 104]; we henceforth refer to this configuration as the Humble/Arai structure following refs.[9, 78].

Most interestingly, several instances of {113} defects and their rod-like precursors (the so-called LIDs) are now found in the simulation. In Figure 3.14e, a partially reconstructed LID structure is shown which is surrounded by five- and seven-membered rings. This structure is a precursor to the (110)-oriented interstitial chains that lead to the formation of {113} defects [144]. An example of the latter is shown in Figure 3.14f, which shows how three of the interstitial chains shown in Figure 3.14e can aggregate to form a {113} planar defect. Comparison of the {113} defect shown in Figure 3.14f to literature models (see Figure 3.14) indicates that it is of the type /I/, which has the highest density of self-interstitials[70, 97], relative to /IO/ and /IIO/. In the preceding notation, /I/ represents a sequence of adjacent self-interstitial chains, while /IO/ and /IIO/ represent sequences in which some chains are missing (a missing chain is denoted by "O"); see ref.[100] for more details regarding {113} defect classification. The predicted aggregate is in excellent structural agreement with the results of previous calculations and experimentally derived models. Although the formation energies of the various types of {113} defects are slightly different according to previous calculations,[96, 97, 99-101] it is difficult to extend those conclusions to the present results because the defects formed in the present simulations are finite in size and are likely to be affected by entropic contributions (mainly vibrational). Both of these factors could easily affect the favorability order of the various {113} defect types. Finally, in

Figure 3.14g, two Humble/Arai 4-interstitial clusters are shown in a side-by-side configuration (surrounding an eight-membered ring) that represents the building block for {100} planar defects. In other words, {100} planar defects can be found in both zero pressure and tensilely strained simulations, while {111} and {113} defects are observed only in the absence and presence of tension, respectively.

The effect of temperature on interstitial aggregation under tensile stress is shown in Figure 3.15, which is a snapshot of a system annealed at 1400K and 1% tensile strain for 7.4 ns. Now, large {100} platelets are the predominant clusters throughout the simulation domain. It is therefore clear that the formation of {100} defects is somehow more robust than that of {113} defects, at least with respect to elevated temperature. In fact, out of all the defect structures observed in the preceding simulations, {100} planar defects appear under the widest range of operating conditions; for example, they are the only type of defect to exist both at zero pressure and under applied tension. The reasons for this are not obvious from the present simulations but will be addressed with the thermodynamic analysis presented in Chapter 4.

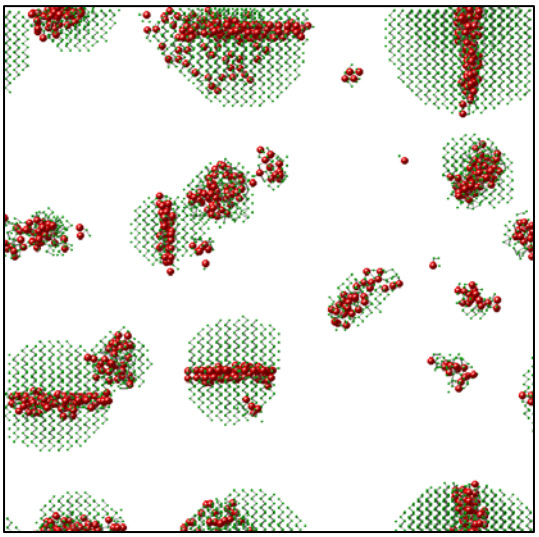

Figure 3.15: System-wide evolution of interstitial cluster distribution at 1400K and -3GPa pressure (approx. 1% tensile strain). Total simulation time is 7.4 ns. Large (red) spheres denote self-interstitials; small (green) spheres show lattice atoms that are displaced by more than 0.2Å from their equilibrium positions. All other atoms are deleted for clarity. Horizontal direction is [100] and vertical is [001].

3.3.2 Kinetic Considerations for the 3D-2D Morphological Transformation

The morphological transformation size data in Figure 3.12 does not lend insight into the kinetics of transformation between the three-dimensional and planar cluster morphologies. In the following simulation, we probe the transformation kinetics by creating large three-dimensional clusters under +3GPa compression and 1200K and then subjecting the system to a rapid decrease in the applied pressure in order to drive the transformation to planar defects. In the results shown in Figure 3.16, an MD simulation of self-interstitial aggregation was carried out at 1200K and +3GPa for 10.0 ns. No transformation into a planar structure was observed for any cluster as expected due to the compression applied to the system. At 10.0 ns, the simulation box was gradually expanded to remove the compressive stress over a time period of 0.3 ns and the

simulation further continued at zero pressure for 6.9 ns. As shown in Figure 3.16, clusters larger than n_I=42, which is the critical size at 1200K (and zero applied pressure), immediately begin to undergo morphological evolution towards the planar {111} configuration (denoted by arrows in Figure 3.16b). The speed of the transformation indicates that any kinetic barrier for the collapse is low, and that the transition sizes reported in Figure 3.12 are equilibrium quantities.

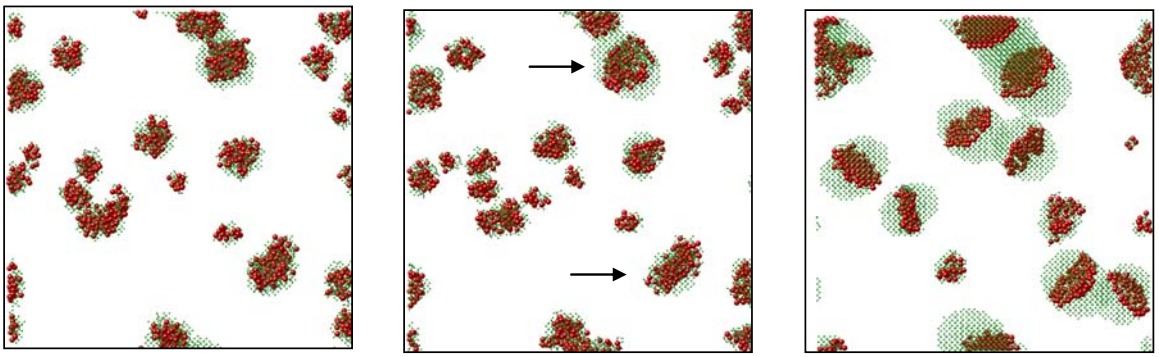

Figure 3.16: Evolution of self-interstitial clusters during strain relaxation at 1200K.(a) After 10 ns at +3 GPa, (b) 0.3 ns later as the pressure was reduced from +3 GPa to 0, and (c) after a further 6.9 ns at zero pressure. Large (red) spheres denote self-interstitials; small (green) spheres show lattice atoms that are displaced by more than 0.2Å from their equilibrium positions. All other atoms are deleted for clarity. Arrows denote onset of 3d-2d transition following pressure drop to zero. For all frames, horizontal direction is [100] and vertical is [001].

There are two key questions that arise from the preceding results of self-interstitial aggregation as a function of temperature and pressure. The first question is one that is generally associated with the use of empirical potentials: are the EDIP predictions

consistent with those from other commonly employed empirical potentials for silicon such as Tersoff and/or Stillinger-Weber? In particular, is the strong effect of lattice strain qualitatively reproducible with another potential model, or is it a peculiarity of the EDIP potential? We address this question in the following section. The second question is: precisely what are the mechanistic roles of strain and temperature in the selection of self-interstitial cluster morphology, and can our results help explain some of the outstanding questions related to morphological selection in implantation experiments? This question is addressed in detail in Chapter 4 by considering in detail the thermodynamics of single clusters under different temperatures and applied pressures.

3.4 Direct MD Simulation of Self-Interstitial Aggregation – Other Potentials

3.4.1 Tersoff Potential Simulations

Several of the large-scale MD aggregation simulations discussed in the previous section were repeated using the Tersoff potential. Similar cell sizes, self-interstitial concentrations, and applied strain were used. One well known limitation of the Tersoff potential for silicon is the very high melting temperature prediction (approx. 2650 K for the parameters given in ref.[147]). The results from the EDIP and Tersoff calculations were thus compared using the ratio of the EDIP and Tersoff melting temperatures, i.e. $T_m^{EDIP} / T_m^{TERS} \sim 0.58$, so that the temperature interval $1900K \le T \le 2250K$ in the Tersoff calculations was approximately mapped onto the interval $1100K \le T \le 1300K$ for EDIP.

First, a sequence of zero pressure simulations was performed at 1900K, 2100K, and 2250K. Snapshots of the atomic distributions at the end of each simulation (total simulated time in each case was approximately 6-7 ns) are shown in Figure 3.17.

At 2250K (Figure 3.17c), the interstitial clusters appear to retain their three-dimensional morphology up to fairly large sizes and do not exhibit a collapse into any type of planar structure during the course of the simulation (the maximum cluster size observed in this simulation is about 90). This result is qualitatively consistent with the EDIP predictions (at 1300K). Unfortunately, shorter Tersoff simulations were necessitated by the fact that the Tersoff potential is computationally more expensive to evaluate than EDIP. However, the Tersoff results at 2100K (Figure 3.17b) confirm that {111} planar defects are in fact predicted by the Tersoff potential at higher temperatures and the 3D-2D transition size appears to be in line with that predicted by EDIP (see Figure 3.12). A more significant deviation in the predictions of the two potentials appears at 1900K (Figure 3.17a). Here, the Tersoff simulations predict an environment quite similar to that observed under tensile conditions (and moderate temperatures) with EDIP. A large number of 4-interstitial clusters in the Humble/Arai configuration are observed, and as expected from the preceding considerations, these are accompanied by the formation of one or two (very small) LID precursors and several small {100}-oriented platelets. Most importantly, no {111}-oriented planar defects are observed by the time the simulation is terminated. In other words, at zero pressure, the Tersoff potential appears to be capable of producing both types of defect morphologies, {111} and {113}/{100}, with variations in the temperature alone. By contrast, tensile conditions were required to stabilize the {113}-related defects within the EDIP simulations.

Nonetheless, it is worth noting that all defect configurations obtained with Tersoff are in very good agreement with those predicted in the EDIP simulations, irrespective of the simulation conditions that were employed to obtain them.

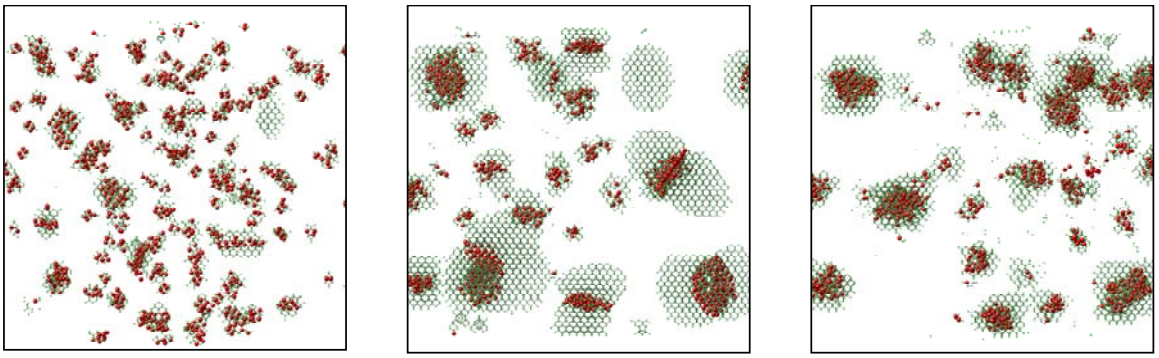

Figure 3.17: System-wide evolution of interstitial cluster distribution at zero pressure and (a) 1900K, (b) 2100K, and (c) 2250K using the Tersoff potential. Large (red) spheres denote self-interstitials; small (green) spheres show lattice atoms that are displaced by more than 0.2Å from their equilibrium positions. All other atoms are deleted for clarity. Horizontal direction is [110] and vertical is [001].

In order to establish whether the 1900K Tersoff results indicate a qualitative discrepancy between the two potentials, which would cast some doubt on the validity of the EDIP predictions discussed above, an additional simulation was performed at 1900K and +3GPa of applied pressure; see Figure 3.18. As with the EDIP simulations, the interstitial aggregation process is again found to be highly sensitive to lattice strain. Under compression, {311}-defect precursor LIDs or {100} platelets are no longer generated and almost no Humble/Arai 4-interstitial clusters are observed. Although most clusters are still three-dimensional at 6.1 ns, transitions to small {111} platelets are

already evident. Qualitatively, at 1900K and 1% compressive strain the Tersoff potential predicts an environment that is similar to that of EDIP at 1100K and zero strain, while the zero strain Tersoff prediction is roughly consistent with that of EDIP under tension. One possibility that has not been addressed directly in our simulations here is that EDIP simulations at zero pressure may indeed also predict the formation of {113} defects but require even lower temperatures than those considered here. However, the reduced mobility of interstitials below about 1000K makes it difficult to access this regime without substantial computational expense.

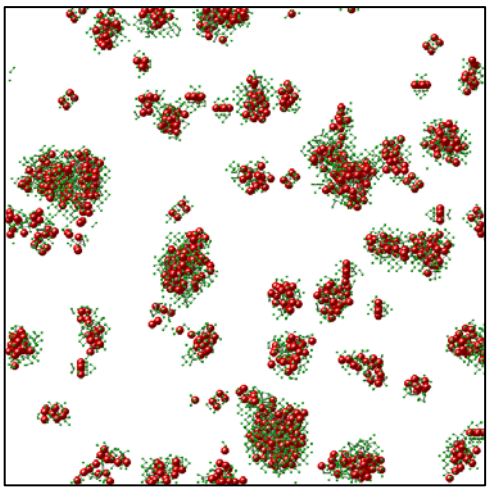

Figure 3.18: Tersoff simulation at 1900 K and +3GPa after 6.1 ns of simulation; no 2-dimensional structures are present for the current cluster size distribution. Large (red) spheres denote self-interstitials; small (green) spheres show lattice atoms that are displaced by more than 0.2Å from their equilibrium positions. All other atoms are deleted for clarity. Horizontal direction is [100] and vertical is [001].

3.4.2 Stillinger-Weber Potential Simulations

The Stillinger-Weber (SW) potential was used to carry out some exploratory simulations to further determine whether the general trends observed with EDIP and Tersoff are reproduced. In Figure 3.19, snapshots from smaller simulations (39,304 host particles and 216 self-interstitials) are shown at two different temperatures, 1330 K and 1500 K, and pressures, zero and -3GPa. A primary reason for employing smaller cells was the additional computational cost associated with evaluating forces with the SW potential. The two temperatures correspond roughly to 1200 K and 1350K, respectively, in the EDIP simulations. In the zero pressure simulations, clear evidence for the formation of {111} planar defects is apparent, with the 1500 K simulation generating a large {111} RLD defect in the center of Figure 3.19 (b). The application of 1% tensile strain at 1500 K (Figure 3.19 (c)) inhibits the formation of {111} defects, and although the system studied is small and the simulation time short, some reorganization into a {100} planar structure is apparent for the defect denoted by the arrow. Again, these trends are qualitatively in agreement with the predictions of the other potentials, demonstrating a remarkable consistency across the three potentials.

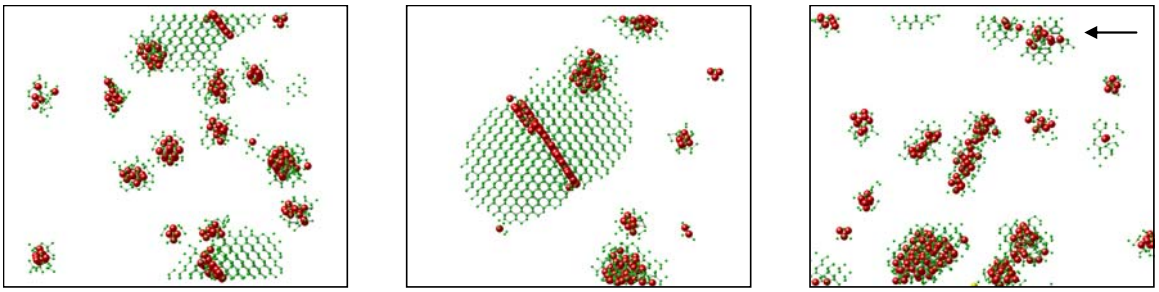

(a) (b) (c)

Figure 3.19: Stillinger-Weber simulations at: (a) 1330 K and zero pressure at 3.3 ns, (b) 1500 K and zero pressure at 2.8 ns, and (c) 1500 K and -3GPa at 1.9 ns. Horizontal direction is [110] and vertical is [001].

3.5 Conclusions

The aggregation of silicon self-interstitials into various cluster morphologies has been studied using multiple commonly-employed empirical interatomic potentials for silicon. Overall, the different potentials provide a coherent picture for self-interstitial clustering, although some differences are apparent. The effects of both temperature and hydrostatic pressure on the self-interstitial aggregation process were considered in the present studies. All three potentials demonstrate similar overall temperature dependence. At high temperature and zero pressure, self-interstitial clusters assume disordered, three-dimensional configurations until they reach large sizes. At lower temperatures, clusters undergo a morphological transition from the three-dimensional state to planar configurations. The critical size for this transition is temperature dependent and becomes smaller as the temperature is decreased, presumably because of reduced entropic favorability of the three-dimensional configurations at low temperatures. Moreover, the

transition appears to be kinetically favorable and no apparent barriers are observed in our simulations.

Both the EDIP and SW potentials predict that {111}-oriented planar defects are dominant at zero pressure. The {111} defects are observed in one or more of three configurations: rod-like defects (RLDs), partial (Frank) dislocation loops (FDLs), and perfect dislocation loops (PDLs). The structures of the various planar defects predicted in the simulations are in excellent agreement with TEM reconstructions and the results of electronic structure calculations. Generally, the EDIP simulations show that RLDs form first, followed by FDLs and then PDLs; these trends are consistent with experimental observations. Also seen in the EDIP simulations at zero pressure are {100}-oriented plate-like defects, which are not commonly observed in real samples, but have been predicted theoretically to be quite favorable relative to other planar defect structures.

A somewhat more complicated picture appears with the Tersoff potential, particularly at lower temperatures. Once again, high temperatures lead to the formation of large three-dimensional clusters, in which the transition to planar morphology is delayed. As the temperature is lowered, {111} planar defects are formed by 3D-2D collapse as seen in the EDIP simulations. However, at the lowest temperature considered (1900 K, or about 1100 K on the EDIP scale), the {111} morphology is no longer observed; instead {100} defects and {113} defect precursors are observed. The latter consist of {110}-oriented interstitial chains that are also commonly observed experimentally in ion-implanted silicon. Associated with this qualitatively different aggregation morphology is a preponderance of four-interstitial clusters, with the majority assuming the well-known ground-state “Humble-Arai” configuration [9, 78].

The apparent difference between the Tersoff and EDIP/SW results can be bridged by considering the effect of hydrostatic pressure on the interstitial aggregation process. In general, it is found that compression, like temperature, stabilizes the three-dimensional morphology relative to any of the planar structures and shifts the transition size to larger clusters. This is observed for all potentials. However, the application of hydrostatic tension in the EDIP and SW simulations at moderate temperature (1100 K - 1200 K) leads to the disappearance of {111} planar defects and favors the formation of {100} and {113} defects, along with the stabilization of the four-interstitial Humble-Arai clusters. As the temperature is increased under tension, the {113} defects tend to be replaced by large {100} planar defects, which is also observed in the Tersoff case. In other words, it is generally observed that the results of the EDIP and Tersoff calculations are essentially equivalent up to a shift in the applied strain – a 1% strain environment in the EDIP (and SW) simulations shows similar behavior to the zero strain Tersoff simulation.

The results in this work suggest an intriguing connection between the strain state of the lattice and the morphology of the self-interstitial defect population, in addition to the expected role of temperature. First, we find that under some conditions, a direct path to the formation of {111} defects is possible, without the previously supposed role of {113} clusters. Here, interstitials aggregate to form three-dimensional structures which spontaneously collapse to form the {111} configurations. Whether this happens or not in the simulations depends strongly on both the temperature and local strain. Under some tension, or at least in the absence of compression (for Tersoff), the formation of {113} defects does indeed appear to be the primary aggregation mode. Under these conditions, previous studies suggest that these defects later transform to {111} structures at larger

sizes, but the size range for this transformation is beyond the scope of the present simulations. In the chapter 4, we study the thermodynamics of the various structures obtained here and provide a detailed mechanistic picture for self-interstitial aggregation and its dependence on temperature and hydrostatic stress.

4 Thermodynamics Analysis of Self-Interstitial Clusters

In Chapter 3 it was shown that direct, large-scale molecular dynamics simulations based on empirical interatomic potentials were able to spontaneously generate many of the complex self-interstitial cluster morphologies found in ion-implanted silicon samples. The various predicted structures were found to be in excellent structural agreement with microscopy observations and electronic structure calculations.[24, 28, 35, 36, 70, 96, 104] Overall, the three different potentials employed, namely the environment-dependent interatomic potential (EDIP)[14], Tersoff[147], and Stillinger-Weber (SW)[139], all predicted consistent overall trends, leading to a qualitatively coherent picture for some aspects of self-interstitial clustering in silicon. In particular, it was found that cluster morphology is sensitively dependent on both the temperature and stress within the lattice. At high temperature (>0.85 Tm) and in the absence of stress, self-interstitial clusters tend to assume three-dimensional disordered structures that grow to large sizes (i.e. hundreds of interstitials) before suddenly transforming to planar defects aligned along the {111} directions. The {111} defects observed include rod-like defects (RLDs), partial dislocation loops (FLDs) and perfect dislocation loops (PDLs); these structures have all been observed in experiment under various annealing conditions. The 3D-2D transformation appears to be facile and proceeds rapidly without being subject to

significant kinetic barriers. In the EDIP and SW simulations, lowering the temperature reduces the transition size but maintains the overall morphological evolution.

Under uniform tension for the EDIP and SW models, and at zero stress/low temperature for Tersoff, the {111} structures are no longer favored; instead, planar structures oriented along the {113} and {100} directions are found, with the {100} defects becoming increasingly favorable at higher temperatures. Although the {113} morphology is commonly observed in silicon samples, the {100} is not, even though it has been found to be about as stable as the other morphologies. Moreover, {100} platelets are common in germanium[111] and carbon.[71, 78] In aggregate, our results appear be in good agreement with many trends found in implantation experiments, but also suggest that self-interstitial clustering may be somewhat complicated by the presence of multiple aggregation pathways that depend on both temperature and stress.

4.1 Formation Thermodynamics for Self-Interstitial Clusters

In this chapter, we attempt to shed light on the various observations discussed in Chapter 3 by studying in detail the thermodynamics of individual clusters. Previously reported analyses of self-interstitial cluster thermodynamics generally have focused on cluster energetics at zero temperature.[9, 15-17, 19, 24, 70, 95-97, 100-102] These studies have employed a broad range of theory to describe interatomic interactions, ranging from empirical potentials (EP), [15, 24, 100] to tight-binding (TB),[9, 97, 101] to electronic density-functional theory (DFT).[16, 17, 70, 95, 96, 102] While there are some discrepancies between the various studies regarding the precise values and ordering of the

predicted formation energies, some general conclusions can be drawn. First, it is clear that on a per-interstitial basis, and in the limit of infinite size, the formation energy of all {111} planar defects is lower than either {100} or {113} defects.[24, 70] Moreover, for clusters larger than some transition size, PDLs are the most stable of the {111}-oriented planar defects because of a lack of a stacking-fault. Both of these results are consistent with the experimental observation that self-interstitial clusters eventually tend to coarsen into FDLs and then PDLs under most annealing conditions.[28, 38, 88, 105, 116-118] On the other hand, the absence of {100} planar defects in silicon wafer annealing experiments cannot be explained on the basis of simple energetics as these are found to possess formation energies that are very similar to the various configurations of {113} defects. For example, Goss[70] employed DFT within the local density approximation (LDA) to compute the formation energies of infinite {100} and {113} defects and found that the {100} defect was in fact slightly favored over the {113}. Chou et al.[24], using SW, find the reverse trend but again the difference is too small to explain the consistent lack of {100}-oriented planar structures in ion-implanted silicon wafers.

Using a combination of experimental observations, kinetic model regression to experimental data, and analytical models for defect energetics, the work in refs.[25-28, 37, 38] built a comprehensive picture for the formation energies of the various self-interstitial cluster morphologies that is largely consistent with atomistic simulation results. Overall, a sequential process was described, which begins with the formation of small compact clusters of self-interstitials. These grow to form LIDs and {113} planar defects, the latter being the most energetically favorable up to cluster sizes of several hundred interstitials. At even larger sizes, the {113} defects transform into the more

favorable {111} planar defects; first FDLs are formed and then PDLs. No explicit consideration of {111} RLD defects was given in the energetic picture of ref.[27, 28]; all rod-like defects were assumed to be of the {113} type.

One important feature that emerged from ref.[36] was that the model regression of compact cluster energies in the size interval $1 < n_I < 15$ strongly suggested that the formation energies per interstitial are non-monotonic in size. In particular, certain cluster sizes (n_I=4, and 8) were found to possess substantially lower formation energies per interstitial than neighboring sizes. Recently, Lee and Hwang[104] performed a comprehensive series of density functional theory (DFT) calculations, which provide some indication of energetic favorability at *n*=4 and *n*=8, but the effect shown was quite weak relative to the strong trends observed in ref.[36], particularly at *n*=8. The building block responsible for the apparent energetic stability at *n*=4 and *n*=8 is a fully fourfold coordinated four interstitial cluster with *D*2*d* symmetry, which has been identified in previous studies on Si (ref.[9]) and diamond;[78] we henceforth refer to this building block as the "compact"Humble/Arai structure. Thus, the ground-state eight interstitial cluster identified in Ref. [104] is comprised of two adjacent Humble/Arai four-interstitial units. However, it is well known that there exist multiple structural motifs for building self-interstitial clusters. In addition to the compact four-interstitial building block, various types of elongated (110)-oriented chainlike structures are also favorable. These appear to be nearly degenerate with the compact structures in the size range of $5 < n < 12$.[96, 104] In fact, Kim *et al.*[96] found, also using DFT, that at *n*=8 an elongated chainlike structure is slightly more favorable than the compact structure, which is in contrast to the predictions in ref. [104]. In either case, it is difficult to infer any significant special

energetic stability at *n*=8, especially given the strong apparent stability inferred experimentally in ref.[36]. Other calculations with tight binding and empirical potentials have also not demonstrated evidence of special energetic stability at these sizes.[19, 96] In this section, we attempt to explain this discrepancy with molecular dynamics (MD) simulations based on the empirical environment-dependent interatomic potential (EDIP).[14]

4.1.1 Formation Energy Calculations for Self-Interstitial Clusters – Ground State Configurations

We first computed formation energies for the structures identified in refs. [96, 104] by periodically quenching (with a conjugate gradient method) atomic coordinates generated by long NVT-ensemble MD simulations at 1100 K and selecting those that matched the structures shown in ref. [104]. The formation energy of an interstitial cluster was defined as $E^f = E_d - (N_d / N_p)E_p$, where d represents the system with the cluster and p represents the perfect reference crystal. The MD simulations were performed using fifth order Gear predictor-corrector integration with a time step of 0.8 fs. Note that numerous structures corresponding to different local minima in the overall potential energy landscape (PEL) were found at each cluster size, but here we focus on the particular structures identified in refs.[96, 104]. The overall energetic trends predicted by the EDIP potential are in excellent agreement with the previous DFT results, although the absolute

values are somewhat higher; note that similar differences exist between the two sets of DFT results (Figure 4.1).

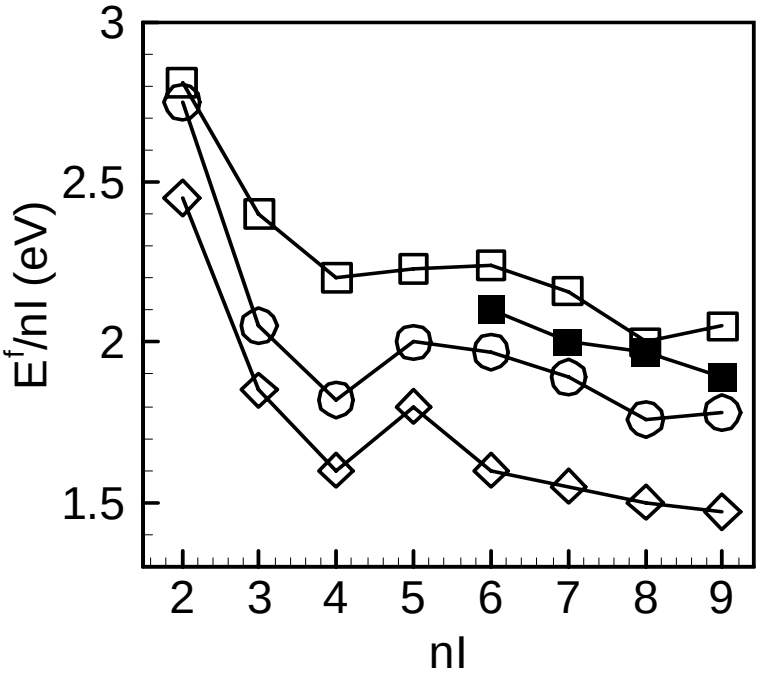

Figure 4.1: Formation energies (E^f) per interstitial as a function of cluster size (n_I). Squares: EDIP results for the structures corresponding to those identified in refs. [96] and [104].; for $n_I \geq 6$, formation energies for both compact (open squares) and elongated (filled squares) are shown (see text for definitions). Circles: DFT results from ref. [104]. Diamonds: DFT results from ref. [96].

For $n \geq 6$, formation energies for both the compact and elongated chainlike structures were calculated. The elongated structures were found to be slightly more energetically favorable, in qualitative agreement with the results of Kim *et al.*, [96]

whereas Lee and Hwang [104] found the compact structure to be at least as favorable until *n*=9. All three sets of calculations show the same overall trend: some special stability at *n*=4 but very little to none at *n*=8, which are in qualitative contrast to the experimentally regressed energies obtained in ref.[36]. The above analyses, however, all neglect the role of entropy, which we suggest here can be significant especially in light of the fact that the experimental data in ref.[36] were obtained at moderately high temperatures $900K < T < 1100K$.

4.1.2 Formation Free Energy Calculations for Self-Interstitial Clusters – Ground State Configurations

We consider first the vibrational entropy associated with the individual structures discussed in Figure 4.1. Formation free energies, defined as $G^f(n) = E^f(n) - TS^f_{vib}(n)$, were computed at 1100 K within the quasiharmonic approximation (QHA)[76] and are shown on a per interstitial basis in Figure 4.2. Increased special stability is now observed at both *n*=4 and *n*=8 for the compact structures (open squares). Note that the free energy of the compact eight-interstitial cluster is significantly lower than that of the corresponding elongated structure (filled squares), while the free energies of the two configurations at the other sizes are comparable. The vibrational entropy is shown explicitly in the inset of Figure 4.2 and is substantially higher for the compact clusters (open circles), relative to the corresponding elongated structures (filled circles) for $n \geq 6$.

Moreover, the peaks at *n*=4 and *n* =8 show that the perfect Humble/Arai structure is the source of this entropy.

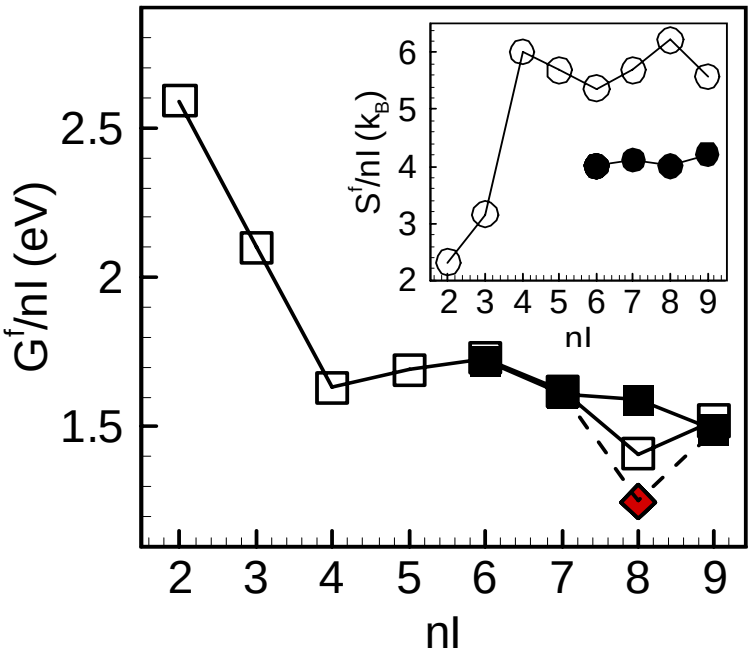

Figure 4.2: EDIP formation free energies (G^f) as a function of interstitial cluster size at 1100 K. Open squares: compact structures. Filled squares ($n_I \geq 6$): elongated structures. Diamond symbol shows free energy including the estimated configurational entropy (see text). Inset: QHA-EDIP formation vibrational entropies as a function of cluster size at 1100 K. Open circles: compact structures. Filled circles: elongated structures.

It is difficult to precisely identify the features of the compact four-interstitial building block that lead to the increased vibrational entropy, but the unique nature of the near-ideal bond angles associated with the cluster is likely to play a role. Previous

electronic structure calculations [31] identified additional vibrational modes that are associated with the compact four-interstitial cluster. In summary, these variations in vibrational entropy imply that selection between compact and elongated morphology during self-interstitial cluster growth at finite temperature cannot be determined solely based on the formation energy.

Vibrational entropy is not the only possible source of entropy for self-interstitial clusters. Configurational entropy may arise from the presence of numerous mechanically stable configurations of the defect cluster, each of which corresponds to a distinct local minimum in the multidimensional PEL. The notion that a crystal defect can exist in several (not necessarily degenerate) configurations is not surprising, but whether there are enough of these configurations to imply a significant contribution to the defect entropy has only recently been suggested.[92] The rotational symmetry of the *D*2*d* Humble/Arai[9, 78] four-interstitial building block is 4, leading to 16 degenerate (rotational) configurations per pair for the eight-interstitial cluster in the compact configuration. Additionally, there are many nearly degenerate ways in which the second Humble/Arai[9, 78] four-interstitial cluster can be placed relative to the first; some of the configurations obtained within our MD simulations are shown in Figure 4.3. This large number of translational degrees of freedom is unique to compact structures comprised of multiple Humble/Arai[9, 78] clusters. Clearly, the strong binding between the two Humble/Arai four-interstitial building blocks is preserved over several neighbor shells. It is difficult to count manually the total number of nearly degenerate possible

configurations N_{conf}, which increase the entropy of any cluster according to the relation $S_{conf} = K_B \ln(N_{conf})$.

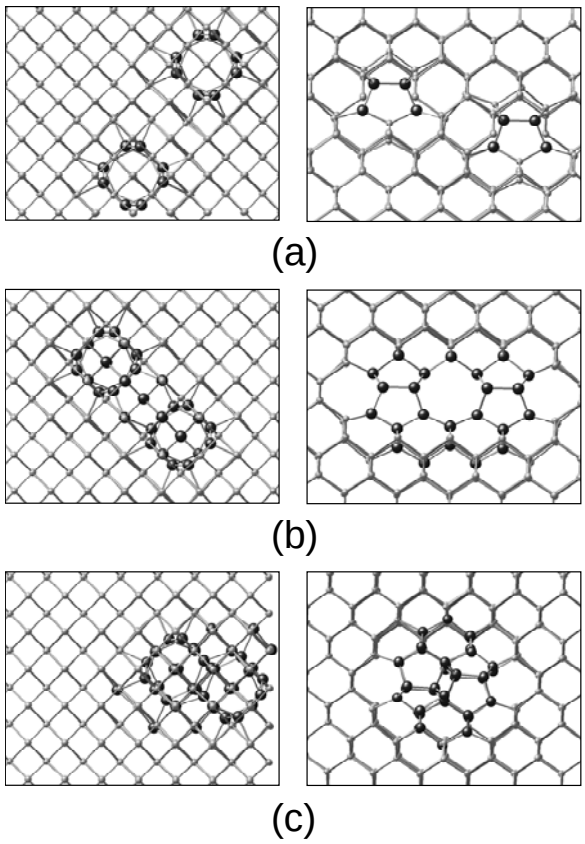

Figure 4.3: Nearly degenerate configurations for the compact eight-interstitial cluster based on combinations of two Humble/Arai four-interstitial building blocks. Left-hand panels are projections normal to [100], right-hand panels are projections normal to [110]: (a) Ef =16.23 eV, (b) E^f =15.95 eV, and (c) E^f =15.86 eV.

Nonetheless, based on the configurations in Figure 4.3, the eight-interstitial cluster appears to be strongly bound up to the fourth or fifth neighbor shells defined within the (100) projection. Moreover, additional degeneracy is obtained by varying the relative vertical positions of the two four-interstitial clusters (see right-hand panels in Figure 4.3). Every 400–500 such configurations (of approximately equal formation energy and vibrational entropy) would lead to a reduction of about 0.1 eV in the per interstitial formation free energy of the compact eight-interstitial cluster at 1100 K (see diamond symbol in Figure 4.2). Note that the special degeneracy for compact eight-interstitial cluster is uniquely large because of high symmetry of the four-interstitial building block and the degeneracy of neighboring sizes is likely to be much lower. The combination of vibrational and configurational entropies favors the compact over the elongated configuration of the eight-interstitial cluster for temperatures above 600–700 K, i.e., the compact structure is likely to be dominant at typical annealing temperatures. In summary, the two sources of entropy, vibrational and configurational, appear to substantially affect the thermodynamics of small self-interstitial clusters at finite temperature. Both entropic sources are particularly large for structures comprised of the Humble/Arai four interstitial building block, which is the building block for self-interstitial clusters in the compact configuration, and provide a compelling explanation as why very strong stability at n=8 has been extracted from experiments at moderate annealing temperatures but not yet confirmed by literature calculations of formation energies to date. It should be stressed that the extracted parameters in ref.[36] are effective *free* energies rather than simple energies because they are a measure of the overall probability of observing each size. As such, all entropic sources should be

considered in calculations attempting to make a direct connection to these data. The temperature dependence introduced by entropic contributions suggests a possible mechanism for explaining the different morphologies that have been observed in self-interstitial clusters at different annealing temperatures. We analyze this hypothesis further in the following sections using a more general thermodynamic framework, and also investigate how these features tie into the temperature and strain response of the aggregate morphology observed in Chapter 3.

In the section 4.2, we briefly review the methodological details of a computational approach for analyzing the total (classical) free energy of defect clusters; we developed in Chapter 2 for estimating the thermodynamics propertied of vacancy clusters. In Section 4.3, the results of calculations based on the EDIP are presented and discussed in detail. We place special emphasis on the analysis of entropic contributions, which have been largely ignored in the literature to date, but which can be extremely important in setting defect behavior at high temperature.[92, 93] We also make mechanistic connections to the results obtained in Chapter 3. Some of the calculations are repeated in Section 4.4 using the enthalpy rather than the energy to define the distributions. In Section 4.5, additional results obtained with other silicon empirical potentials are presented; these are primarily used to validate some of the principal conclusions drawn from the EDIP simulations. Finally, conclusions and a mechanistic picture for self-interstitial aggregation are presented in Section 4.6.

4.2 Computational Framework for Single Cluster Thermodynamic Analysis

We have recently demonstrated in Chapter 2 that the total (classical) free energy of defect clusters in crystals can be modified substantially by configurational and vibrational entropy, particularly at elevated temperature.[61, 92] Configurational entropy arises from the presence of numerous mechanically stable configurations that a given defect cluster can assume within the lattice. Each of these configurations, α, (so called *inherent structures*) can be identified by a local energy minimum, V_α, in the multidimensional potential energy landscape (PEL) that defines the overall system.[68, 137] For solids and certain fluid states, the system can be assumed to spend the majority of its time in one of the local minima, only occasionally making excursions over the saddles separating the minima. Based on these ideas, as applied in previous work on supercooled liquids and glasses,[128, 129] a direct computational approach for measuring the total (classical) free energy of a defect cluster has been developed; a brief discussion of the method is provided here and further details are given in ref.[92]

In general, the total (classical) Helmholtz free energy of a system is given by $G = -k_B T \ln(Z)$, where Z is the canonical partition function. Assuming that the system of interest satisfies the assumptions described above, the partition function can be expressed as

$$Z = \exp\left(-\frac{G}{k_B T}\right) = \frac{1}{\Lambda^{3N}} \int g'(V_\alpha) \exp\left(-\beta V_\alpha\right) dV_\alpha , \qquad (4.1)$$

where $\Lambda = (h^2 / 2\pi mk_B T)^{1/2}$ is the thermal de Broglie wavelength. The quantity $g'(V_\alpha)$ represents the density-of-states (DOS) or degeneracy of minima with an energy V_α and includes both configurational and vibrational states, i.e. $g'(V_\alpha) \equiv N_{vib}^{\alpha} g(V_\alpha)$, where $g(V_\alpha)$ is the configurational DOS and N_{vib}^{α} is the number of vibrational states in basins with energy V_α, i.e. $S_{vib}^{\alpha} = k \ln N_{vib}^{\alpha}$. Knowledge of the function $g'(V_\alpha)$ therefore directly leads to the free energy of the system; note that $g'(V_\alpha)$ is independent of temperature and can be used to compute free energies for all temperatures with application of eq.(4.1).

In order to enumerate the local minima in the PEL, lengthy MD simulations of the system of interest (i.e. a bulk crystal containing a defect cluster) are performed. The local minima are found by periodically quenching the atomic coordinates generated by MD to the local minima; intervals of 100-200 time steps were used throughout the present work. Only configurations corresponding to connected clusters, as defined by the Stillinger criterion[137] are considered in the analysis. The occurrences are histogrammed into energy bins of width 0.1eV. The resulting histogram is in fact the probability distribution function for the states of the system, i.e.

$$p(V_\alpha) = g'(V_\alpha) \exp(-\beta V_\alpha), \tag{4.2}$$

from which the DOS can be obtained directly.

As shown in Chapter 2 (ref.[92]), the above procedure can be applied to systems with and without defects and the formation energy for a particular defect configuration is

then given as $\Delta E_\alpha \equiv V_\alpha^d - (N_d / N_p)V^p$, where V^p is the energy of the perfect crystal, and N_p and N_d are the numbers of atoms in the perfect and defective systems, respectively. Finally, the total formation free energy of the defect is given by

$$\Delta G = -T\Delta S_{vib}^{ref} - k_B T \ln \int g(\Delta E) \exp\left(S_{vib}(\Delta E)/k_B\right) \exp\left(-\beta\, \Delta E_\alpha\right) d(\Delta E_\alpha), \quad (4.3)$$

where "ref" denotes some reference configuration for the defect and $\Delta S_{vib}^{ref} = S_d^{ref} - (N_d / N_P)S_p$. A reference configuration is only required for computing absolute free energies.[92]

MD simulations for PEL sampling were carried out in either the NVT or NPT ensembles. In the former case, the system volume was chosen (using short NPT simulations) to provide the desired value of the hydrostatic pressure. Unless otherwise explicitly stated, the NVT ensemble was used as the default ensemble. Depending on the cluster size of interest ($1 \le n_I \le 20$), simulation cells containing up to 8000 silicon lattice atoms were used. The 5th-order Gear predictor-corrector method[8] with time steps of 1.0-3.2 fs was used to integrate the particle trajectories; convergence of the simulation results with respect to the time step size was checked in each case using short test simulations.

4.3 Thermodynamic Analysis of Single Self-Interstitial Clusters – EDIP Results

4.3.1 Probability Distribution Functions for Small Clusters at Zero Pressure

The probability distribution functions (PDFs) of cluster formation energies were computed for several small interstitial clusters ($3 \le n_I \le 8$) at 1100K and zero pressure using NVT simulations; these are shown in Figure 4.4 (a). It is important to emphasize once again, that the probability of observing any given configuration includes all entropic and enthalpic contributions, and that the total (classical) free energy of the defect cluster is proportional to the integral of the PDF. In general, the formation energy distributions are fairly broad, spanning several eV, and peak at some intermediate value demonstrating that at 1100K, the most likely configurations are not necessarily those with the lowest formation energy. The general form of the PDFs is similar to that for vacancy clusters, which was discussed in detail in our previous work.[92]

The origin of the broad peak at intermediate formation energies in each case is best understood by considering eqs. (4.2) and;(4.3) it is simply the point at which the exponential decay of the Boltzmann factor is balanced by the exponential growth of the degeneracy (i.e. the density-of-states, or DOS) as the formation energy increases. The exponential growth of degeneracy with increasing formation energy (see Figure 4.4 (b)) arises from the fact that higher formation energy configurations are increasingly spatially extended and therefore can generate more local minima in the potential energy landscape.[68, 137]

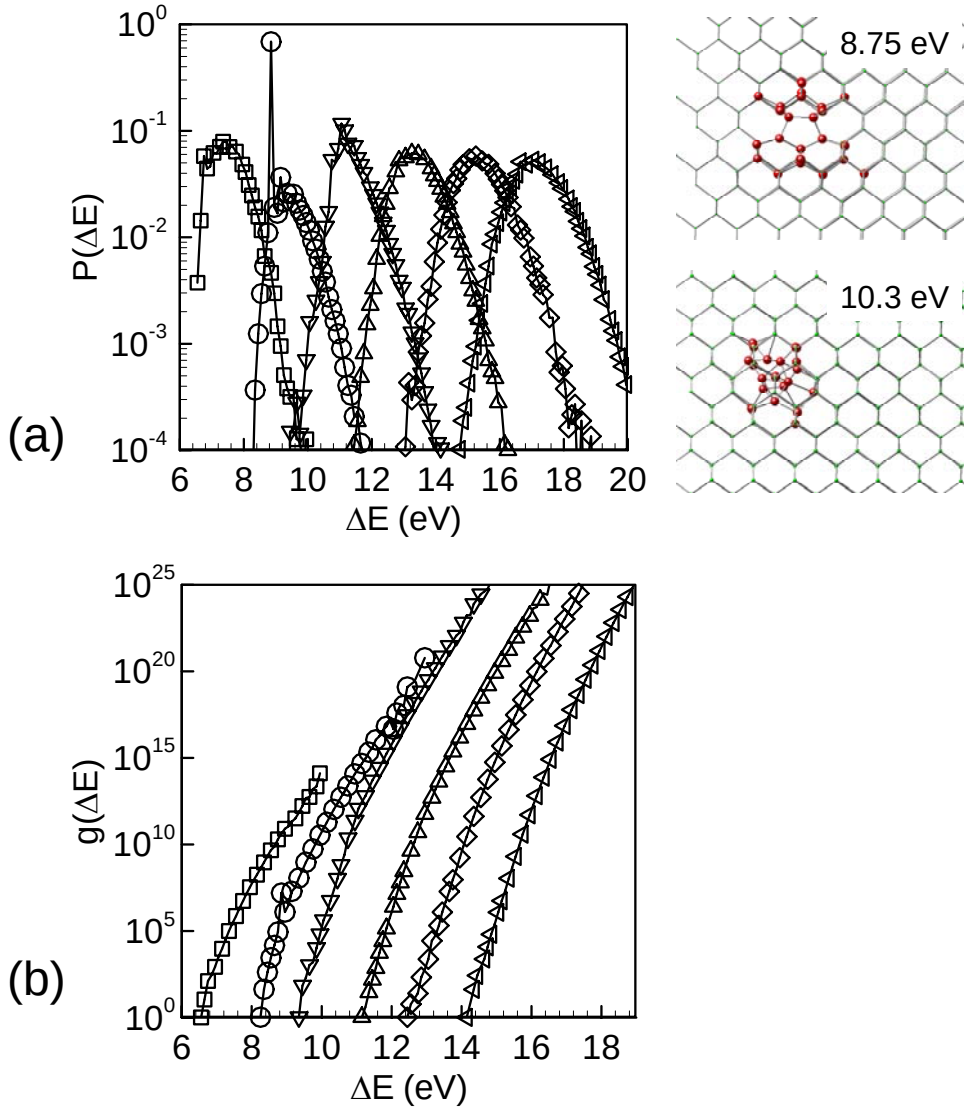

Figure 4.4: (a) Formation energy PDFs (at 1100 K), and (b) DOS for small interstitial clusters in the size range $3 \le n_I \le 8$ computed with the EDIP potential. For both panels, squares represent $n_I = 3$, circles $n_I = 4$, gradients $n_I = 5$, deltas $n_I = 6$, diamonds $n_I = 7$, and left triangles $n_I = 8$. Insets in (a) show two configurations for the 4-interstitial cluster; upper – Humble/Arai configuration, lower – extended, higher energy configuration.

Several of the relaxed configurations for a given cluster were manually verified to correspond to well-defined local minima within the energy landscape. These configurations were perturbed by introducing small random atomic displacements, and subsequently re-relaxed to the same local minimum. Obviously, sufficiently large disturbances were able to move the system away from a given configuration.

The PDF for the 4-interstitial cluster in Figure 4.4 (a), however, exhibits an unusual feature – a sharp spike in the probability at $\Delta E = 8.75$ eV that dominates the entire distribution. In other words, under the conditions of 1100K and zero stress, the equilibrium 4-interstitial cluster spends over 80% of its time in configuration(s) with formation energy that lie in the interval $8.7 \le \Delta E \le 8.8$ eV. In fact, the single configuration that resides in this energy interval is the Humble/Arai configuration discussed in Chapter 3 and ref.[93]; see the upper inset in Figure 4.4(a). Other inherent structures for the 4-interstitial cluster predicted by the EDIP potential are more disorganized; an example is shown in the lower inset in Figure 4.4(a). Note that the anomalous spike corresponding to the Humble/Arai configuration in the 4-interstitial probability distribution is not energetic in nature; neighboring configurations with almost the same formation energy are much less likely (by about a factor of 100) to be observed. Moreover, the EDIP potential actually identifies a few (low probability) configurations that have slightly lower formation energies than the Humble/Arai structure, a fact that is at odds with recent DFT results that predict this to be the energetic ground state structure[104]; this issue will be addressed in more detail later.

One possible reason for the very high probability of observing the Humble/Arai configuration is that it possesses larger formation entropy (which may be vibrational

and/or configurational in origin) than any other configuration of the 4-interstitial cluster. In order to test this hypothesis, the vibrational formation entropy, defined as $S_{vib}^{f}(k_B) = (\Delta E - \Delta A)/T$, was computed within the Quasi-Harmonic Approximation[76] for a large number of energy-minimized configurations for the 4- and 5-interstitial clusters; see Figure 4.5. Two vacancy clusters (n_V=6 and n_V=10) also were considered for comparison. As shown in Figure 4.5, all four clusters exhibit qualitatively similar behavior; overall the vibrational entropy of formation increases approximately linearly with formation energy, reflecting the tendency of more extended defects to produce a larger number of additional vibrational states into the crystal. The variability in the trend is somewhat larger for the self-interstitial clusters, which could arise because of their more complex morphologies. Closer inspection of the 4-interstitial case, however, does confirm the suggestion that vibrational entropy is responsible for the special stability of the Humble/Arai configuration. The Humble/Arai configuration, denoted by the single large circle possesses vibrational entropy of formation that is at least 5-6 k_B higher than neighboring configurations, which readily accounts for the 100-fold increase in probability for this particular configuration, i.e. $\exp(5) \sim O(10^2)$. In the remaining cases, no single configuration exhibits this anomaly, and as a result the PDF varies relatively smoothly across the entire formation energy range.

It is notable that the 8-interstitial cluster, which can assume configurations corresponding to two adjacent Humble/Arai building blocks, does not exhibit the sharp spike structure in its PDF (see Figure 4.4(a)), even though these configurations also are

expected to possess large vibrational entropy. The reason for this apparent anomaly will be discussed in the following section.

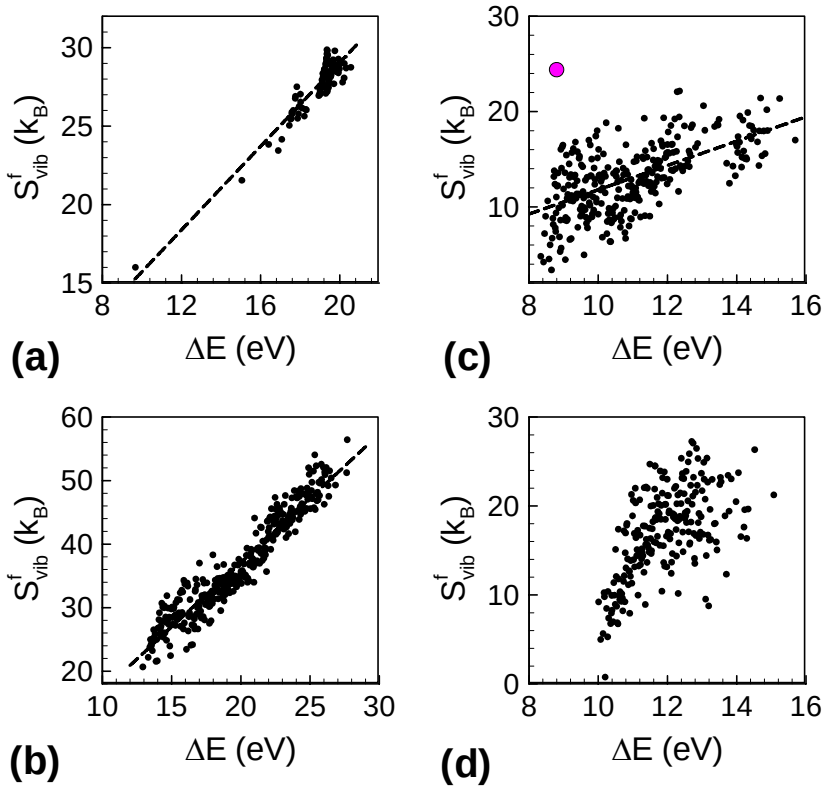

Figure 4.5: Vibrational entropy of formation for (a) 6-vacancy, (b) 10-vacancy, (c) 4-interstitial, and (d) 5-interstitial clusters as a function of formation energy. Each symbol represents a QHA calculation for a single configuration of a given cluster. Large circle (purple) in (c) represents the Humble/Arai configuration. Dashed lines are guides only.

The entropic nature of the stabilization of the Humble/Arai configuration of the 4-interstitial cluster would suggest that it is insensitive to the effect of temperature. Indeed, the probability spike in the 4-interstitial PDF persists as the temperature is increased, as

shown in Figure 4.6. Although the overall PDF for the 4-interstitial cluster shifts to the right with increasing temperature, the Humble/Arai spike remains due to the increasing importance of its high vibrational entropy of formation. As a result, it is expected that the Humble/Arai configuration should play an important role in self-interstitial clustering kinetics, even at the elevated temperatures typically employed in damage annealing. This conclusion can be contrasted starkly with the more common case of energetic stabilization of "magic" cluster sizes, such as for vacancy clusters.[120] In the energetic stabilization case, clusters of particular sizes are favored relative to others at low temperature because certain configurations minimize the formation energy (e.g. by the minimization of dangling bonds). However, at elevated temperature, this effect is obscured by entropic contributions and the formation free energy per vacancy is found to decrease almost monotonically with cluster size.[92, 122] Stated another way, magic sizes of silicon vacancy clusters (and any other energetically stabilized cluster) are not important at the high temperatures relevant to crystal growth and wafer annealing, whereas in the case of self-interstitials, such "magicness" appears to be largely entropically driven and therefore can be relevant at any temperature.

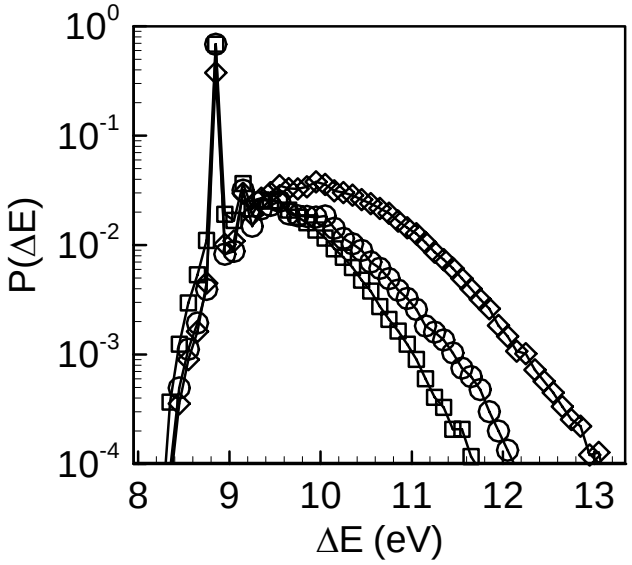

Figure 4.6: 4-interstitial cluster PDFs as a function of temperature. Squares – 1100K, circles – 1200K, diamonds – 1300K.

4.3.2 The Effect of Hydrostatic Lattice Strain on the Thermodynamics of Small Interstitial Clusters

While the entropic stabilization of the 4-interstitial cluster renders it relatively insensitive to temperature, it is surprisingly sensitive to lattice strain. Shown in Figure 4.7 (a) are the area-normalized PDFs at 1100K for the 4-interstitial cluster at zero pressure (zero strain), +3 GPa hydrostatic compression (-1% strain), and -3 GPa hydrostatic tension (1% strain). The peak related to the Humble/Arai configuration is seen to become even more pronounced under tension, and is now predicted to be the absolute lowest energy structure, i.e. the few (low-probability) local minima in the PEL to the left of the Humble/Arai peak observed at zero pressure disappear under applied tension.

Conversely, under compression, the Humble/Arai peak completely disappears and the 4-interstitial PDF becomes smoothly varying as for the other cluster sizes shown in Figure 4.4 (a).

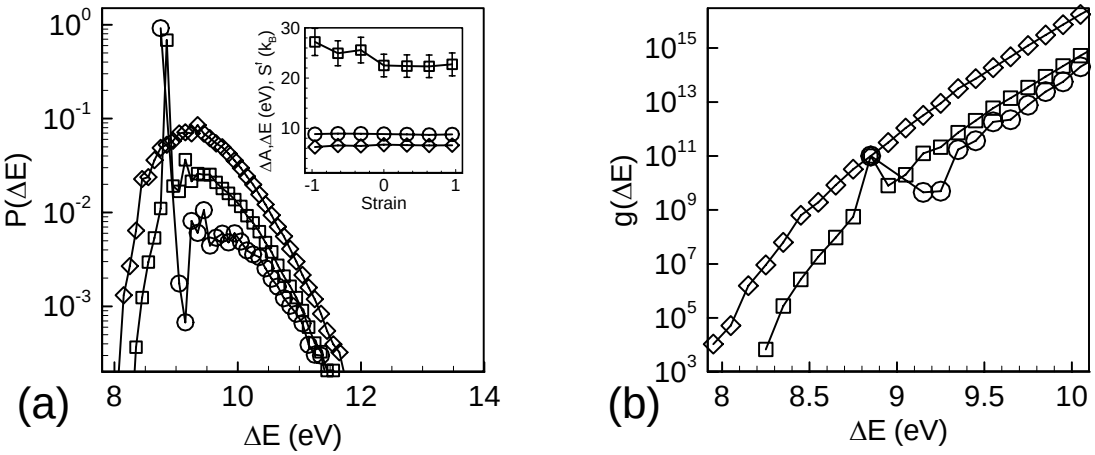

Figure 4.7: (a) PDF for the 4-interstitial cluster as a function of hydrostatic pressure (lattice strain): squares – zero stress; circles – -3GPa applied pressure (1% tension); diamonds – +3GPa applied pressure (1% compression). Inset: formation thermodynamics for the 4-interstitial Humble/Arai configuration as a function of strain (diamonds – free energy, circles – energy, squares – vibrational entropy). (b) 4-interstitial DOS as a function of hydrostatic pressure (lattice strain) anchored to the Humble/Arai configuration (see text): squares – zero strain; circles – 1% tension; diamonds – 1% compression.

At first glance, it would seem that these results indicate that the formation thermodynamics of the Humble/Arai structure for the 4-interstitial cluster depend strongly on hydrostatic pressure (lattice strain). The formation enthalpy, vibrational entropy and total free energy were computed for the Humble/Arai structure as a function

of lattice strain and are shown in the inset of Figure 4.7(a). Clearly, the formation thermodynamics of the Humble/Arai configuration are essentially independent of lattice strain. The slight apparent increase in the formation entropy under compression is mostly a result of scatter in the data, and in any case, would predict that the Humble/Arai structure is increasingly dominant under compression, i.e. opposite to the trend in Figure 4.7(a).

The interesting effect of strain on the stability of the Humble/Arai configuration observed here instead arises from the density-of-states function for the 4-interstitial cluster, $g'(\Delta E)$ shown in Figure 4.7 (b), where $g'(\Delta E) = p(\Delta E)\exp(\beta \Delta E)$. The three curves shown represent the DOS at each of the three strain conditions and have been anchored to each other on the basis of the formation energy interval containing the Humble/Arai structure. Assuming that the formation energy bin containing the Humble/Arai configuration (centered at $\Delta E = 8.75$ eV) is entirely comprised of that single state, the DOS functions for the three curves must be equal at that value of formation energy. Further assuming that the configurational degeneracy of the Humble/Arai configuration is O(1) based on the D2d symmetry of the structure, the total number of states in that energy interval must arise entirely from vibrational contributions, i.e. $g'(\Delta E) \sim N_{vib}$, where $N_{vib} = \exp(S_{vib}/k_B) \sim 1 \times 10^{11}$ (S_{vib} : $25k_B$) for the Humble/Arai configuration. These considerations allow us to anchor the three DOS curves to absolute values and make quantitative comparisons between them. Further details regarding the anchoring of DOS curves is provided in ref. [92]

Comparison of the three DOS functions in Figure 4.7(b) shows clearly that the overall density of states increases with increasing hydrostatic pressure. The apparent decreased stability of the Humble/Arai structure under compression therefore arises because additional states (i.e. local minima in the PEL) are introduced by the compression, reducing the probability of observing that particular configuration. Conversely, tension appears to lower the overall density of states and increases the dominance of the Humble/Arai configuration relative to all others. Interestingly, all local minima with energies below that of the Humble/Arai structure become mechanically unstable under 1% tensile strain and the Humble/Arai structure now is predicted to the be ground state structure. *Thus, we find that it is not the formation thermodynamics of the Humble/Arai configuration that depend strongly on strain, but rather the density of all other configurations that collectively compete with this special configuration.*

The mechanism by which the overall DOS is affected by lattice strain is not immediately obvious. It is plausible to suppose that as atoms are brought into closer contact by compression, increasing the number of neighbors-per-particle, the PEL predicted by the EDIP interatomic potential becomes more complex (i.e. rougher) and the number of local minima in a given energy interval increases. Whether this is generally true for other interatomic potentials such as Tersoff will be addressed in Section 4.5.

The effect of isotropic hydrostatic pressure (lattice strain) on other cluster sizes (n_I=5, 8, 12) is shown in Figure 4.8 for comparison. For each cluster size the formation energy PDF is shown for zero pressure/strain (small filled squares) and at -3GPa hydrostatic tension (1% tensile strain- large open circles); all PDFs are normalized to unit area.

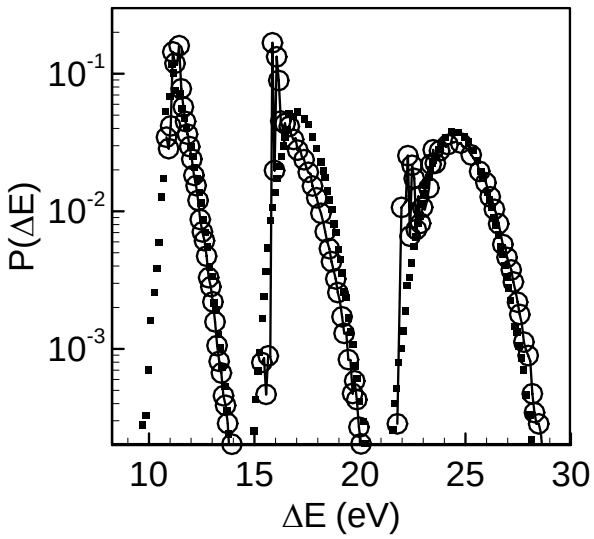

Figure 4.8: Effect of isotropic tensile strain on the probability distribution functions for the 5-, 8-, and 12-interstitial clusters (shown left to right, respectively). Filled squares denote zero strain, open circles denote 1% tensile strain (-3GPa applied pressure).

For the 8-interstitial and 12-interstitial clusters, a significant change is observed in which a spike similar to that observed for the 4-interstitial case appears under tension. By contrast, the 5-interstitial distribution is essentially unresponsive to strain. Once again, the effect of tension on the 8-interstitial and 12-interstitial PDFs arises from a reduction in the overall DOS, thereby increasing the significance of a few cluster configurations that possess increased stability relative to the rest within the distribution. The 8- and 12-interstitial clusters are expected to possess similar behavior to that of the 4-interstitial cluster because they are able to assume configurations that are comprised of integer multiples of the Humble/Arai building block. Because these special structures are absent in the 5-interstitial case, no effect is observed on the overall PDF. Thus, even though the

overall density of states may be reduced by tensile hydrostatic pressure (lattice strain), the DOS is reduced evenly across the energy spectrum and the areal normalization maps them onto each other.

Examples of the special configurations for the 8-interstitial cluster that become dominant under lattice tension are shown in Figure 4.9, along with their assignments to various locations in the 8-interstitial PDF at -3GPa hydrostatic pressure (1% tensile strain).

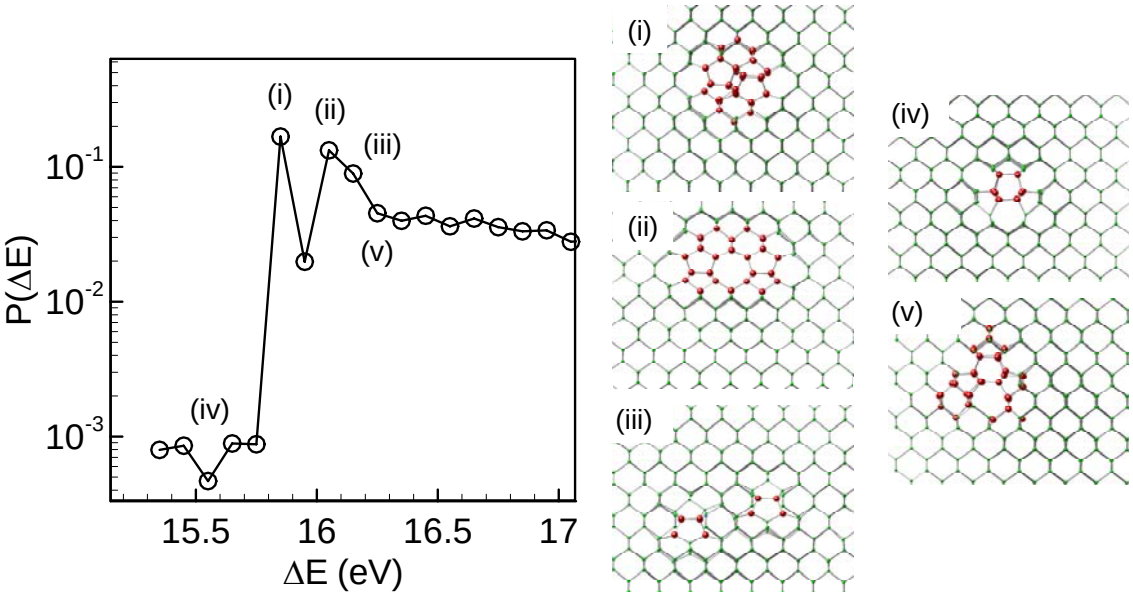

Figure 4.9: Formation energy PDF for the 8-interstitial cluster at 1100K and -3GPa applied pressure (1% tensile strain) highlighting the distribution at low values of formation energy. The 8-interstitial configurations that correspond to the various numbered locations on the PDF are shown in the insets on the right-hand side of the figure.

The two peaks located at formation energies $\Delta E = 15.86\ eV$ and $\Delta E = 16.05\ eV$, labeled by (i) and (ii) in Figure 4.9, respectively, correspond to configurations comprised of two adjacent Humble/Arai 4-interstitial blocks (see insets). Another such configuration (iii) appears at formation energy $\Delta E = 16.23\ eV$. Note that the configuration (ii) is essentially a very small {100} defect showing clearly the alternating 5 and 8-membered ring structure found in our PMD simulations in Chapter 3 and section 4.1. Each of these three configurations is stabilized by the high vibrational entropy associated with the Humble/Arai structure, which explains their high probability of being observed in the PDF for the 8-interstitial cluster. Collectively, they also suggest yet another source of entropy which is configurational in nature. As discussed in section 4.1, there are in fact a large number of possible (and nearly degenerate) ways to arrange two Humble/Arai 4-interstitial building blocks to form a cluster of size 8. Based on a very rough estimation, this configurational entropic source can additionally lower the free energy of the 8-interstitial cluster by a few tenths of an electron volt per interstitial.[93]

Configurations labeled (iv) ($\Delta E = 15.56\ eV$) and (v) ($\Delta E = 16.26\ eV$) in Figure 4.9 represent a fundamentally different arrangement of the 8 interstitials within the cluster. Both of these configurations are comprised of a single row of interstitials aligned in the {110} direction and are in fact LIDs that have not yet fully reconstructed.[144] In other words, structures (iv) and (v) are building block for planar {113} defects. Configuration (v) is higher in energy due to rearrangement in the atomic position surrounding the interstitial row, but is otherwise essentially the same structure as (iv). Although the LID

configuration is approximately energetically degenerate to the Humble/Arai configurations, they appear at substantially lower probabilities; in fact, structure (iv), although lowest in formation energy, possesses very low probability. The difference in probability of observing the {100} precursors (i.e. (i), (ii), or (iii)) versus the {113} precursors (i.e. (iv) or (v)) is entirely attributable to the special vibrational entropy of configurations based on the Humble/Arai motif. As shown in Figure 4.2, configuration (i) possesses up to 2 kB of additional vibrational entropy per interstitial relative to configuration (iv), which is amply sufficient to explain the almost 1000-fold increase in probability associated with the former structure relative to the latter. Similar vibrational entropy enhancement is attributable to the various different arrangements of two Humble/Arai building blocks. These arguments are expected also to apply to the case of 12-interstitial (and larger) clusters, which simply include additional Humble/Arai building blocks.

The interplay between energetic and entropic stabilization of the {100} and {113} precursors suggests an explanation for some of the observations in chapter 3. There, it was found that {100} and {113} were generally found together, but that {100} defects were more likely to form at higher temperatures and {113} were only found at lower simulation temperature. The above considerations indicate that in order to observe these special structures, the overall density-of-states must be low enough to allow them to be dominant; for the EDIP potential at least, this is accomplished by presenting a tensile environment within the lattice. The propensity for forming {100} defects at higher temperatures arises because of the additional vibrational entropy associated with the Humble/Arai motif. On the other hand, at lower temperatures, the lower formation energy

of the {113} precursor could dominate. The one thing our results do not appear to resolve is why the {100} planar defects are not more frequently observed in experiment – these structures are both energetically and entropically favorable.

Finally, we note that as the cluster size increase, the overall density-of-states should increase, reducing the dominance of the {100} and {113} precursors relative to the disordered configurations. This is in fact why the 8-interstitial cluster requires tension to present structure in the DOS, while the 4-intersitial cluster does not. As shown previously in Figure 4.8, the spikes in the PDF corresponding to {113} and {100} precursors for the 12-interstitial cluster are seen to be relatively small compared to the remainder of the distribution at -3GPa hydrostatic pressure (1% tensile strain). In other words, as the cluster size increases the possible dominance of single configurations becomes increasingly unlikely. However, as the cluster size increases, the morphology of the cluster is likely to already be well-established and further growth would be directed within the {100} or {113} motifs.

4.4 Calculation of Formation Enthalpy PDFs

In the preceding sections, NVT MD calculations were employed to compute the probability distribution functions for the cluster formation energies. Although the system volume was chosen to correspond to a desired applied pressure, this condition is generally not achieved in an NVT simulation unless the formation volume[10] of all cluster configurations, defined as

$$\Delta V_\alpha = V_\alpha^d - (N_d / N_p) V^p , \tag{4.4}$$

is equal. In eq.(4.4)), the "d" and "p" superscripts denote the defective and perfect systems respectively, which are both held at the same pressure. For the general case where the formation volumes are variable, configurations that have large formation volume magnitudes may be subject to tension or compression, altering their formation *enthalpies*; this effect would not be captured in the formation *energy* distributions calculated in the prior sections. Moreover, the energy minimization for each configuration also was performed at constant volume, which generally leads to the generation of additional tension in the final structures because the average lattice parameter is larger at high temperature than it is at zero temperature.[20, 30]

In order to assess whether these assumptions materially affect the results presented in the previous sections, we repeated the calculations of the PDF for the 4-interstitial cluster at 1100 K within the NPT ensemble. NPT simulations also provide direct access to formation enthalpy distributions. In these calculations, all energy minimizations also were performed at constant pressure (i.e. the simulation box was allowed to change size during energy minimization) in order to ensure that the final formation enthalpy was defined at the intended pressure. The LAMMPS code [3] with our implementation of the EDIP potential was used for these calculations. Shown in Figure 4.10 are the formation energy PDFs for the 4-interstitial cluster at zero pressure using both the NVT and NPT ensembles. The excellent agreement between the two simulations suggests that the effect of induced tension during energy minimization at

constant volume is negligible, and also that the formation volume change across the PDF is not large. The slight deviation of the two distributions at higher energies may be the result of bias introduced by the constant volume calculations, but the absolute value of the probabilities are small in this region.

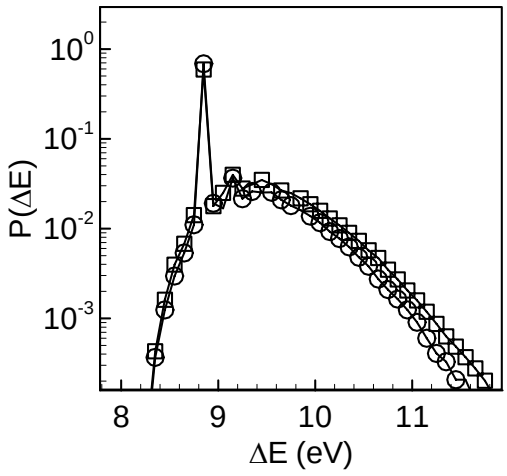

Figure 4.10: Formation energy PDF for the 4-interstitial cluster at 1100K and zero applied stress/strain: squares – NPT MD with constant-pressure energy minimization; circles – NVT MD with constant-volume energy minimization.

Next, formation energy PDFs were computed at three different pressures (-3GPa, 0, and +3GPa) using the NPT ensemble; see Figure 4.11. The location of the peak related to the Humble/Arai configuration is clearly unaffected by pressure, although the overall distributions are modified by the introduction (or removal) of states as discussed earlier in Section 4.3.2. Again, these results are in excellent agreement with those obtained

using the constant volume calculations in Section 4.3.2. We note here that recent DFT calculations[16] appear, in contrast to our present findings, to demonstrate very significant dependence of the formation energy on hydrostatic strain for the Humble/Arai configuration of the 4-interstitial (at zero temperature). The apparent discrepancy can be resolved simply by noting that the formation properties computed in ref.[16] were defined so that the reference and defective simulation cells were held at the same *strain*, rather than stress. In general, the introduction of a defect into the simulation cell alters the effective elastic coefficients within the cell (in a size-dependent manner). Therefore, the application of equal strains in the reference and defective cells leads to a pressure differential that in turn modifies the calculated formation energy in a cell size-dependent manner.

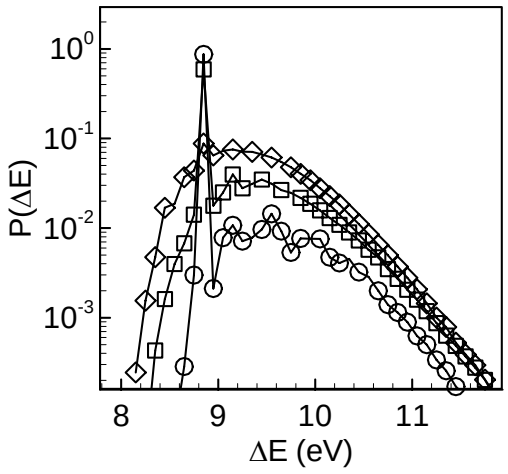

Figure 4.11: Formation energy PDFs for the 4-interstitial cluster at 1100K as a function of applied pressure (NPT MD): squares – zero pressure, circles – -3GPa (approx 1% tensile strain), diamonds – +3GPa (approx. 1% compressive strain).

To further clarify this issue, the formation enthalpy distributions at three different pressures were computed using our NPT framework at 1100K. Here, the formation enthalpies for a particular configuration, α like the corresponding formation energies, were computed based on the relationship

$$\Delta H_\alpha(P) \equiv H_\alpha^d(P) - (N_d / N_p) H^p(P). \qquad (4.5)$$

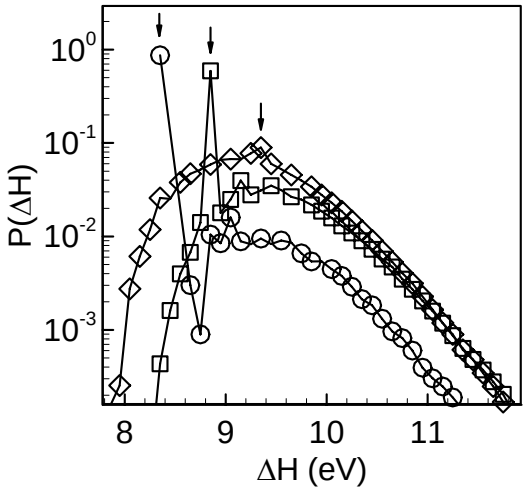

Figure 4.12: Formation enthalpy PDFs (NPT MD) for the 4-interstitial cluster at 1100K as a function of applied pressure: squares – zero pressure, circles – -3GPa (approx 1% tensile strain), diamonds – +3GPa (approx. 1% compressive strain). The arrows indicate the location of the enthalpy bin containing the Humble/Arai configuration.

As shown in Figure 4.12, the formation enthalpy of the Humble/Arai configuration shifts by about 0.5 eV in either direction when 3GPa of pressure (approx.

1% strain) is applied. Since the formation energy is constant, this shift is entirely attributable to the PV contribution arising from the non-zero formation volume of the defect. Thus, for the Humble/Arai configuration, the formation volume is approximately 20 A^3. A plot of the formation volume as a function of formation energy for numerous configurations of the 4-interstitial cluster is shown in Figure 4.13; these values were computed at 1100K and zero pressure.

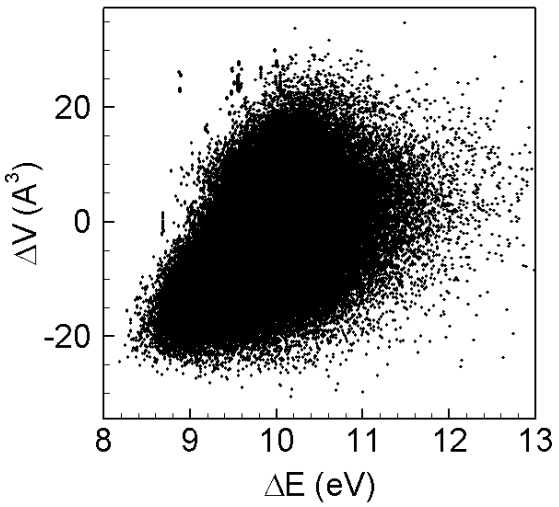

Figure 4.13: Formation volume as a function of formation energy for 4-interstitial configurations at zero pressure.

Although the formation volumes tend to increase with formation energy, they are generally small across the range of formation energies accessed in the calculation. Interestingly, many configurations exhibit negative formation energy, i.e. they occupy

less space than the perfect crystal on a per-atom basis. This is not unexpected given the relative openness of the diamond lattice, as compared to close-packed lattices such as fcc. A consequence of our results is that the formation enthalpy of the various 4-interstitial configurations, including the Humble/Arai one, are only weakly dependent on stress.

4.5 Tersoff Potential Results

In chapter 3 it was shown that the overall self-interstitial cluster morphological evolutions predicted by EDIP, Tersoff, and to a lesser extent SW, were essentially consistent. The primary discrepancy that was noted between the EDIP and Tersoff results was that Tersoff appeared to favor the formation of {100} and some {113} defects at zero applied strain and low temperature, while EDIP requires applied tension before stabilizing any {113} defect precursors (i.e. LIDs). Here we compare the formation energy probability distributions for the 4- and 8-interstitial clusters in order to explain this difference.

The Tersoff-generated formation energy PDFs for the 4- and 8-interstitial clusters at 1900K are shown in Figure 4.14. Both zero and +3GPa applied pressure (1% compressive strain) cases are considered. In the 4-interstitial case, the compressive strain does not appear to substantially reduce the probability of observing the Humble/Arai configuration ($\Delta E = 8\ eV$), although small shifts in the probabilities of higher energy configurations are observed. This is in contrast to the EDIP case (Figure 4.7) where 1% compression led to the disappearance of the Humble/Arai peak in the PDF. On the other hand, the 8-interstitial cluster behavior is qualitatively similar to that of the EDIP case, whereby the peaks associated with Humble/Arai configurations and (110)-oriented

interstitial chains (LID precursors) are substantially reduced by the application of compression.

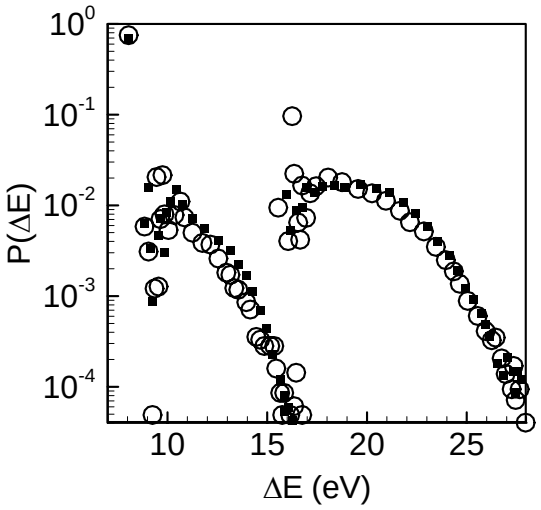

Figure 4.14: Tersoff generated (NVT MD) formation energy PDFs for the 4-interstitial (left) and 8-interstitial (right) clusters at 1900K as a function of applied strain: open circles – zero pressure, small filled squares – +3GPa applied pressure (approx. 1% compressive strain).

Overall, the effect of hydrostatic pressure (strain) on the density-of-states observed in the EDIP case is reproduced in the Tersoff calculations indicating that this is a general phenomenon. However, the dominance of the Humble/Arai configuration for the 4-interstitial cluster in the Tersoff model appears to be more pronounced than that in EDIP, which explains the increased propensity to observe {100} and {113} related structures in the 1900K Tersoff simulations reported in chapter 3. These observations

suggest a qualitative difference in the potential energy landscape roughness predicted by the two models, although a more quantitative analysis of this statement would require more detailed calculations that are beyond the scope of the present study. In other words, the EDIP potential landscape associated with self-interstitial clusters may be rougher that that of the Tersoff one, thereby making it more difficult for a single configuration to dominate even if it possesses uniquely favorable properties such as high vibrational entropy. In both cases, compression appears to increase the roughness of the landscape, eventually drowning out peaks associated with special structures.

4.6 A Mechanistic Summary and Conclusions

The results presented here and in chapter 3 suggest an intriguing mechanistic picture for morphology selection in self-interstitial clustering in which lattice strain, and its effect on entropy rather than energy, potentially plays an important role. We identify two broad situations that are largely consistent across both the EDIP and Tersoff potentials:

4.6.1 Low temperature and/or tensile lattice strain

Under these conditions, special configurations of certain cluster sizes such as n_I=4,8,12 are favored over other possible rearrangements by a combination of low formation energy and large vibrational entropy. For n_I=8 and 12, two main types of distinguishable configurations are possible, which are directly related to the formation of {113} and {100} planar defects. The former is an elongated chainlike structure aligned along the

(110) direction and has been discussed at length in previous experimental and theoretical studies.[27, 28, 36, 96, 97, 100, 101, 143, 144] The latter is much less well studied within the silicon literature because of the scarcity of {100} planar defect observations in ion-implanted silicon, although these are commonly observed in diamond and germanium.[78, 111] This configuration is particularly favored by its high vibrational entropy because it is comprised of an integer number of Humble/Arai building blocks. The growth of both types of structures leads to the eventual formation of {113} and {100} planar defects, both of which were directly observed in the large-scale simulations presented in chapter 3. It is not possible to extend our simulations to the point at which {113} defects evolve by unfaulting into lower energy {111} defects, but previous work shows that this transition is expected at around n_I=500.[22, 28, 38]

4.6.2 Higher temperatures with no compression

Here, the overall density of states associated with interstitial clusters at most sizes (except n_I=4) is sufficiently large so as to "drown out" the special configurations that lead to the {100} and {113} planar defects. As a result, most small clusters assume three-dimensional amorphous configurations up to a certain (temperature and pressure dependent) critical size at which point they collapse into {111}-oriented planar defects of various types including RLDs, FDLs, and PDLs, all of which have been observed experimentally. In this growth mode, the transition to {111} defects is much earlier than that associated with the {113}-{111} transition suggested in ref. [22, 28, 38], and {113} defects are never formed. However, note that even at zero strain, {100} defects are still

observed because of the large vibrational entropy associated with the Humble/Arai configuration.

Our results therefore suggest that lattice strain can dramatically alter the pathway by which self-interstitials aggregate to form the various types of cluster morphologies observed in the literature. A key aspect of this mechanism is that lattice strain acts by modifying the overall density of states distribution of formation energies associated with a cluster, rather than by strongly modifying the formation thermodynamics of a particular cluster structure. Thus, although the particular cluster configurations responsible for {113} and {100} motif formation are entropically stabilized relative to other configurations, this stabilization can become overwhelmed by the large number of other possible (usually higher energy) configurations. Unfortunately, our results do not explain the apparent dearth of {100}-oriented defects in damaged, interstitial-rich silicon; in agreement with previous calculations, these are found to be both energetically and now, also entropically, favorable. A temperature-size evolution map for the morphology of self-interstitial clusters is shown in Figure 4.15 that summarizes much of the results obtained in the present work.

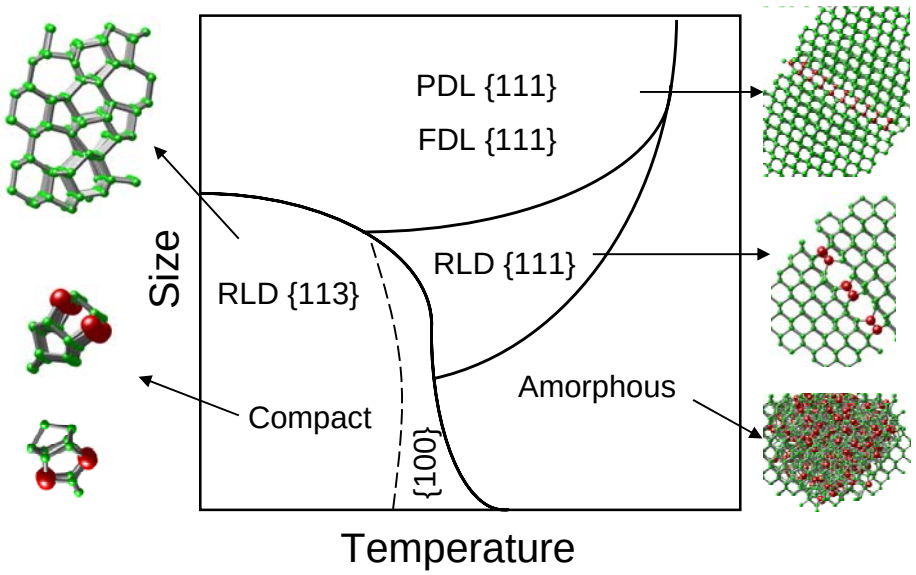

Figure 4.15: Evolution map for self-interstitial aggregation as a function of cluster size and temperature. In most cases, the effect of hydrostatic pressure is qualitatively similar to increasing the temperature.

The speculation on the possible role of strain/stress will require further study. Although hydrostatic stress is generally not engineered into the systems of interest, the implantation process itself can generate complex and transiently varying stress fields that depend in a complex fashion on the implant dose, type and energy.[87-89] Future work in this area might be required to determine whether the stresses arising from implantation and damage annealing can influence the clustering process. On the other hand, biaxial and uniaxial stress fields are more common and further work will be required to characterize the effect of these fields on self-interstitial clustering. Recent DFT calculations show that in some cases the differences may be important and may lead to additional heterogeneities in the cluster distribution.[16]

Finally, we note once again that the preceding conclusions depend substantially on the validity of the empirical EDIP and Tersoff potentials. It should be emphasized that all defect structures that were generated spontaneously in the simulations in chapter 3 are largely consistent with structures that have been verified by high resolution TEM as well as DFT calculations. This includes the small compact clusters (e.g. n_I=4, 8), the elongated, rod-like clusters (n_I=8, 12), and the various planar structures formed in the large-scale aggregation simulations. Comparing the formation energies of small, compact clusters to DFT estimates in ref.[104] further demonstrate that these empirical potentials are able to at least qualitatively capture much of the general picture associated with self-interstitial clustering, if not the precise thermodynamic properties.

5 Carbon Mediated Self-Interstitial Clustering in Silicon

The growth and dissolution of silicon self-interstitial clusters in the presence of carbon have attracted much attention recently because of the role of self-interstitials in the transient-enhanced diffusion (TED) of boron during post-implantation annealing and activation.[33, 127] The occurrence of TED has been unambiguously attributed to the presence of supersaturated self-interstitials, which are formed during ion-implantation of dopants such as boron. The supersaturated self-interstitials are stored in clusters, which can possess a variety of morphologies, depending on the processing conditions. The most commonly observed structures are typically {311} defects[136] and dislocation-loop networks,[44] but three-dimensional clusters are also possible, especially if clustering occurs at high temperatures, such as during crystal growth from the melt.[53]

Once formed, these clusters can become thermodynamically unstable during wafer thermal annealing, which is required to anneal the lattice damage produced by boron ion-implantation and also to activate the boron atoms (i.e. allow them to occupy substitutional sites within the lattice). Cluster dissolution then leads to the observed temporary boron diffusion enhancement via the kick-out reaction $B_i \leftrightarrow B_s + I$, where B_i and B_s represent interstitial and substitutional boron atoms, respectively, and I is a silicon self-

interstitial.[34, 115] This TED effect leads to broadening of implanted boron profiles and poses a challenge for future CMOS device scaling goals.

The presence of high carbon atom concentrations (> 10^{19} cm^3) in the region of the self-interstitial supersaturation has been shown to greatly inhibit TED in several experimental studies, either using highly C-doped layers grown by molecular beam epitaxy (MBE)[110] or carbon co-implantation with the boron.[21] While the use of carbon to inhibit TED continues to be plagued by technological difficulties [110], promising new approaches currently are being evaluated that make a fundamental understanding of carbon-mediated TED of immediate importance [113]. A recent example is to implant carbon atoms and create an embedded layer that does not interact with the surface device-active region, alleviating the previously reported detrimental effects of carbon on the electrical properties of microelectronic devices.

As pointed out in section 1.3.1, numerous simulations of TED-related phenomena have been reported in the literature. These studies have employed approaches ranging from macroscopic rate equation simulations [110], to kinetic Monte Carlo calculations (KMC),[85] to detailed atomistic studies of the energetics and structure of various carbon-silicon complexes [108]. A lot of assumptions have gone into these models, however still no conclusive quantitative picture has emerged on the effect of carbon on self-interstitial clustering in silicon.

In this work, an alternative approach based on parallel molecular dynamics (PMD) is presented that allows for a detailed analysis of the effect of carbon on self-interstitial aggregation without the need to consider every cluster composition or configuration individually. In essence, the averaging over composition and configuration space is

automatically performed within the MD simulation assuming that a sufficient number of atoms are considered for a long enough time. Concurrently, full atomic resolution is provided throughout the entire simulation, and no assumptions, other than the validity of the interatomic potential, are needed. The remainder of the Chapter is organized as follows. The details of the MD simulations and basic results are described first in Section 5.1. Also discussed in this section are the major assumptions of the approach, with emphasis on the choice of the multicomponent Tersoff interatomic potential.[148-150].The results of the atomistic aggregation simulations are presented and discussed in Section 5.2. In Section 5.3, the parallel MD results and additional atomistic simulations of cluster mobility are interpreted in the context of a mean-field model which suggests that it might be possible to treat the carbon-in-silicon system as a quasi-single component system where the carbon atoms are considered implicitly through their effects on the properties of the self-interstitial clusters. Sensitivity analysis of our predictions with respect to the choice of empirical potential and the identification method of interstitial clusters is presented in section 5.4. In Section 5.5, the continuum rate equation methodology developed by Prasad and Sinno[121] is extended to study the aggregation of self-interstitial in presence of carbon. Finally, conclusions are presented in Section 5.5.

5.1 Large Scale Parallel MD Simulation of Carbon and Silicon Self-Interstitial Aggregation

Two large-scale parallel MD (PMD) simulations were carried out using systems of 216,000 silicon atoms, each containing an additional 1,000 self-interstitials initially

placed in uniformly spaced (and therefore initially isolated) tetrahedral sites. In the second simulation cell, 2,000 randomly selected silicon lattice atoms were replaced with substitutional carbon atoms, corresponding to a 0.9% carbon concentration or 4.6×10^{20} cm^{-3}. These large concentrations of self-interstitials and carbon atoms were chosen to allow the systems to exhibit sufficient aggregation in the short MD time scale (nanoseconds). While the high concentrations do affect the overall rate of aggregation, it should be noted that there is no reason to expect that the fundamental micro-processes predicted by the interatomic potential should be altered in a qualitative way. As a result, we expect that to within the accuracy of the empirical potential, our results are directly applicable to the more dilute conditions typically realized in experiments. This issue is addressed further in a later section.

5.1.1 Simulation conditions

In both NVT simulations, the temperature and pressure were fixed at 2650 K and zero, respectively. The Tersoff set of empirical potentials for silicon are well-known to greatly overestimate the melting temperature, and 2650 K was found to be about 600-800 K below the mechanical melting point of pure Tersoff silicon.[147] A direct comparison of this temperature to experimental annealing temperatures (typically around 900 ºC) is not possible, but a consistent estimate can be made based on the self-interstitial diffusion coefficient. A very good estimate for the self-interstitial diffusivity recently has been provided by model regression to several experimental observations including the diffusion of zinc into Si wafers at various temperatures and the formation of the so-called

interstitial-vacancy boundary during Czochralski crystal growth.[59] Comparison of this value to the Tersoff prediction indicates that 2650 K is approximately equivalent to an actual temperature of 1000 ºC, which is in the neighborhood of typical annealing temperatures in TED experiments. Note that this is not a unique assignment of the simulation temperature, but is a relevant one for a study of self-interstitial diffusion and aggregation phenomena.

A time step of 0.38 fs was used in all MD simulations and time integration was performed using the Gear 5thorder predictor-corrector method. The small time step was required to ensure energy conservation in the presence of relatively light carbon atoms and very high temperatures.

5.1.2 Validity of the Tersoff multi-component empirical potential

The multi-component Tersoff potential[148] was used for all simulations, along with the potential parameters specified by Tang and Yip[146]. This potential is one of very few available for multicomponent Group IV systems, and, given the relatively small number of studies of multicomponent systems (relative to pure silicon, for example), it is somewhat difficult to estimate the uncertainties in the following simulations.

However, several previous studies employing this empirical potential have shown that it is surprisingly accurate at predicting structure and properties of silicon-carbon complexes. In an excellent recent study of carbon-silicon defect complex formation, Mattoni et al,[108] used a combination of empirical potential MD and DFT (in the Local Density Approximation - LDA) calculations to investigate energetics and reaction

pathways. Steps of the reaction sequence $C_S + I \rightarrow C_I + C_S \rightarrow C_S C_I + I \rightarrow C_I C_I$ were analyzed in detail by computing system energies as each pair of species were brought together. In each case, the energy profile for the reaction path obtained with LDA-DFT and the empirical Tersoff potential were qualitatively similar, and in some cases almost quantitatively identical. Local energy minima in the first and third reactions shown above predicted by the LDA-DFT calculations also were captured by the Tersoff potential. These results indicate that this empirical potential should be suitable for use in the current study. Additional evidence supporting the qualitative accuracy of the multicomponent Tersoff potential was suggested by the calculations of Tersoff,[149] in which the formation energies and diffusivity of carbon complexes in silicon were found to be in excellent agreement with experimental solubility data.

5.2 Characterization of Interstitial Clusters

5.2.1 Identification of interstitial clusters

Aggregation during the two PMD simulations was monitored periodically using snapshots of the entire configuration of each system. For each snapshot, the configurations were first quenched using conjugate gradient energy minimization in order to make identification of the defect clusters easier. The quenched coordinates were then used to identify individual clusters and generate a size distribution at each time point. A substantial difficulty in the identification of interstitial clusters arises because of the extent of lattice distortion in the vicinity of interstitial atoms. In fact, up to several atoms

can be substantially displaced from their equilibrium positions in the presence of a single silicon self-interstitial [19] and, for the compact structures that were generated in our simulations, the displacements do not follow a regular pattern. Furthermore, it was readily apparent that these displacements were equal in magnitude to the distance of a self-interstitial from the nearest lattice site – i.e. in a cluster of self-interstitials; it is not possible to uniquely identify which atoms are interstitials and which ones are simply displaced atoms.

This issue was addressed by the identification of *Defective Atoms* (DAs), defined as Si or C atoms that are at least $\theta = 27\%$ of a bond length (the latter is about 2.35 Å) from the nearest lattice position. For a given value of the parameter θ, DAs were identified by comparison of the quenched simulation coordinates to a perfect lattice at the same density. Subsequently, the DAs were assigned to individual clusters using a recursive algorithm that determines the connectivity between each DA in the system. The assignment of atoms to individual clusters requires that an interaction distance, β be defined; i.e. sets of atoms that are connected by β belong to the same cluster. For given values of θ and β, a cluster size distribution based on defective atoms can be defined – note that this is not equivalent to the *interstitial* cluster size distribution. The latter was computed by isolating each defective atom cluster and comparing its atomic coordinates to a reference lattice. The number of excess atoms in the cluster gave the number of interstitials contained within the cluster. This number was then used to recompute the interstitial cluster size distribution. Finally, note that this method of identification is

similar to the one presented in Chapter 4 for detecting the interstitial, except that no distinction was made between carbon and silicon interstitials in the carbon-doped case.

Previous atomistic investigations [108] have suggested that the interaction distance between a silicon self-interstitials and a substitutional carbon extends to the 3rd-nearest neighbor (3NN) distance. In the present case, however, this interaction distance is not directly applicable because of the ambiguity in defining interstitial atoms. Note, however, that once the DA interaction distance, β is specified and a cluster identified, the interstitial interaction distance is no longer relevant because all the interstitials in that cluster are automatically assumed to be connected. We have performed a detailed sensitivity analysis of the effect of β and θ on the resulting size distribution that will be presented in Section 0. Here, we simply note that the resulting distribution is only weakly dependent on the choice of these parameters, at least within physically reasonable bounds.

5.2.2 Structure of interstitial clusters

The quenched configurations at 3.46 ns for the pure silicon and 0.9 % carbon-in-silicon simulations are shown in Figure 5.1(a) and Figure 5.1(b), respectively. Shown are *Defective Atoms* (DAs), as defined by $\theta = 0.63\,\mathring{A}$ and $\beta = 4.82\,\mathring{A}$, corresponding to the 3NN distance. The pure silicon case shows substantially greater cluster size evolution with fewer, but much larger, clusters as compared to the 0.9% C-doped case. This result is consistent with the notion that carbon reduces the effective diffusivity of self-

interstitials and therefore inhibits the cluster ripening (or dissolution) process. This effect also has been observed in the float-zone growth of silicon crystals, where carbon doping was observed to increase the density, but decrease the size, of interstitial-type aggregates[52]. For a better perspective, three dimensional snapshots of the interstitial clusters at 3.46 ns for both with and without carbon are also shown in Figure 5.2 and Figure 5.3.

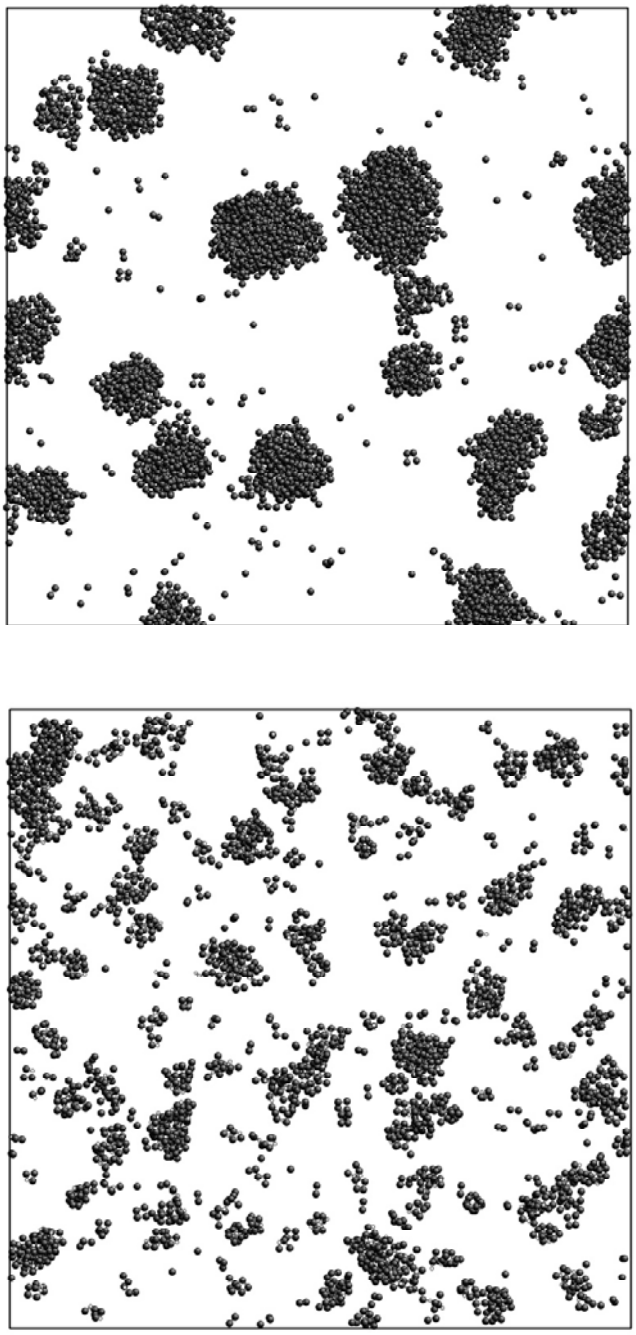

Figure 5.1: Distribution of Defective Atoms (DAs) at $t = 3.46$ ns. (a) pure Si (4337 DAs), and (b) 0.9% C-doped Si (3164 DAs). Note that the number of DAs is much greater than the number of interstitials (1000) because of lattice strain effects.

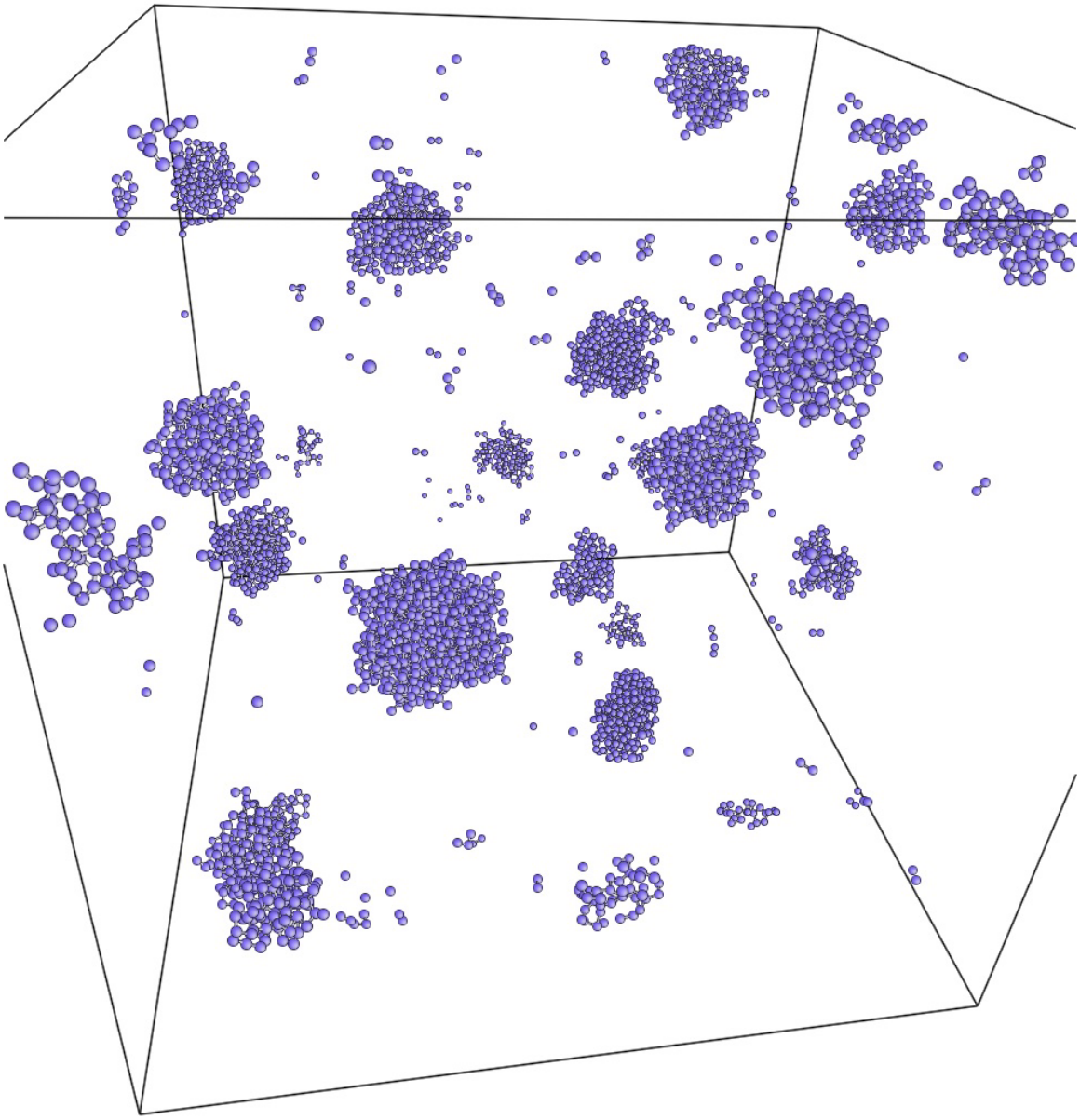

Figure 5.2: Defective atom distribution in pure Silicon at 3.46 ns.

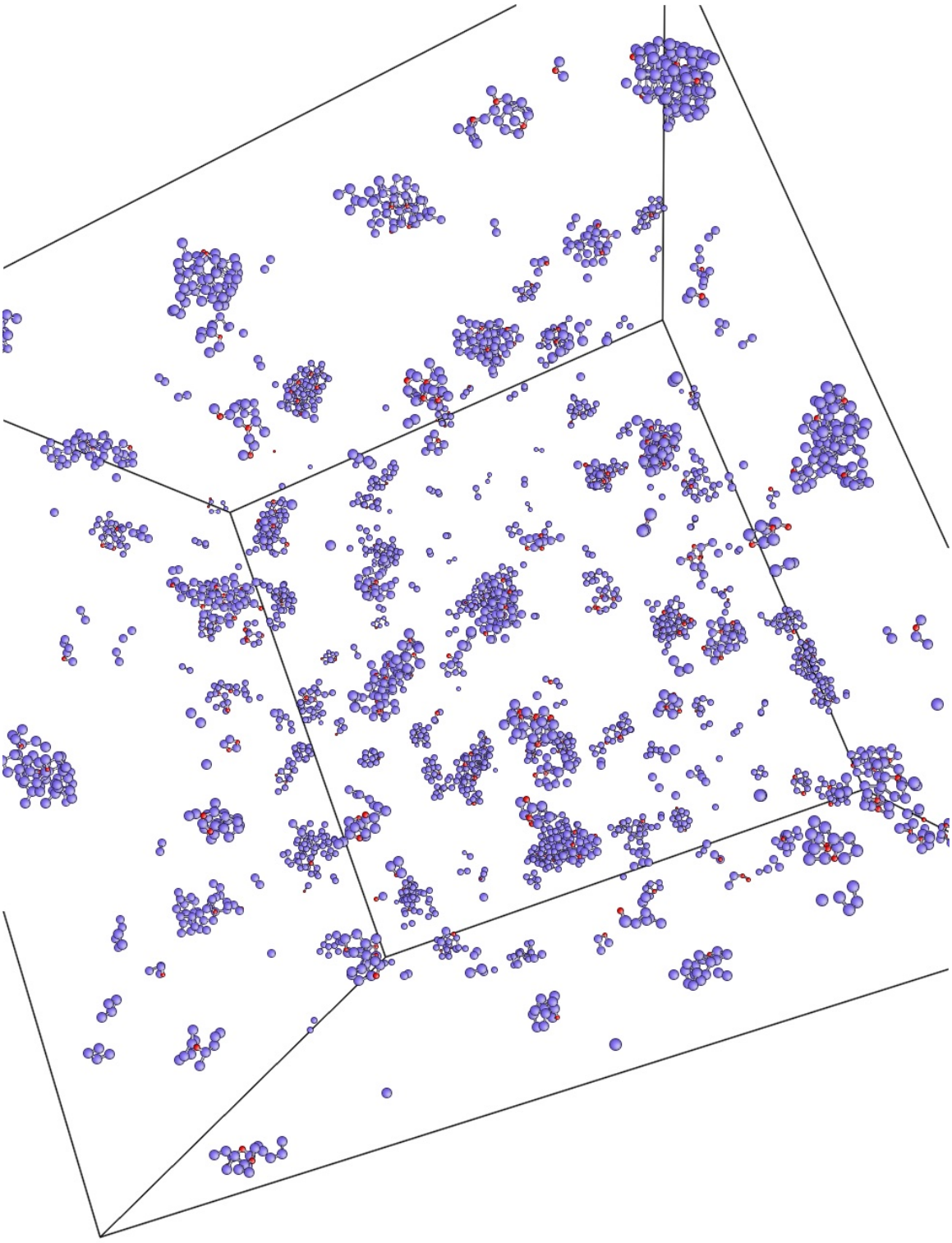

Figure 5.3: Defective Atom Distribution in 0.9% C-doped Silicon at 3.46 ns.

The structure of the DA clusters in Figure 5.1 appears to be different in the two simulations, with the clusters in the pure Si case appearing to be more spherical. The radius of gyration for each cluster about the 3 principal axes[69] was computed. The ratios of the maximum to the minimum radius of gyration (i.e. the aspect ratio) are plotted in Figure 5.4 for both cases.

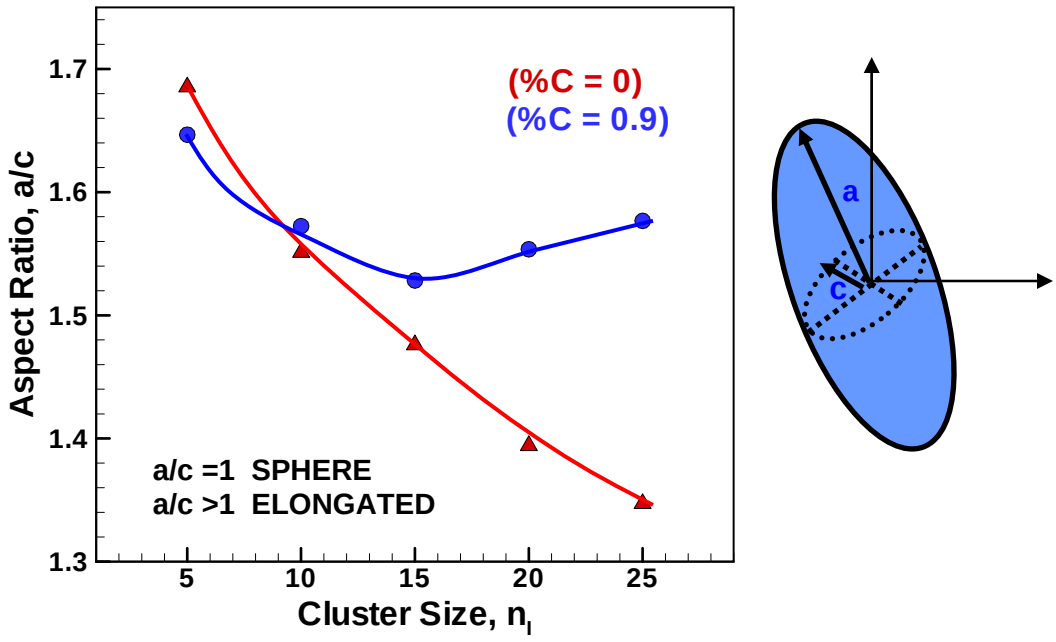

Figure 5.4: Aspect Ratio, maximum to minimum Radius of Gyration about the two principal axes for pure Si (triangles), 0.9% carbon-doped (circles).

The data for each cluster was averaged over all occurrences of a given cluster size and then binned into cluster size intervals of width five. It is clearly seen that the pure Si

clusters are indeed more spherical (i.e. lower aspect ratio) than in the carbon-doped case, particularly for clusters containing more that 15 interstitials. While the larger clusters in the pure-Si case become increasingly spherical with size, the carbon doping leads to increasingly elongated structures. A possible explanation, which will be verified later in this Chapter, is that the carbon atoms locally pin regions of a cluster and prevent it from rearranging to minimize its surface area, at least in the timescales accessible to MD simulation.

The number of DAs in each simulation is not a conserved quantity and can evolve in time. The number of DAs per cluster n_{DA} is shown below in Figure 5.5 as a function of interstitial cluster size, n_I for both carbon concentrations. In both cases, n_{DA} is well represented by a power-law evolution across the entire interstitial cluster size range ($1 < n_I < 120$) but interestingly, has an exponent larger than one: approximately 1.17 for the pure Si case, and 1.07 for the carbon-doped case. The slightly lower exponent for larger clusters in the carbon-doped case is likely due to the compressive strain relief that carbon atoms provide because of their smaller size. The non-linear increase of n_{DA} with cluster size implies that as the size distribution coarsens, the total number of DAs increases and therefore should provide a driving force against coarsening at later times, which could eventually lead to self-limiting of the coarsening process. It is possible that this process might provide a driving force for the hypothesized morphological transformation of compact clusters to dislocation loop networks – the latter are the only observed structures in interstitial-rich silicon grown from the melt [52, 53], but longer simulations will be needed to further investigate this effect.

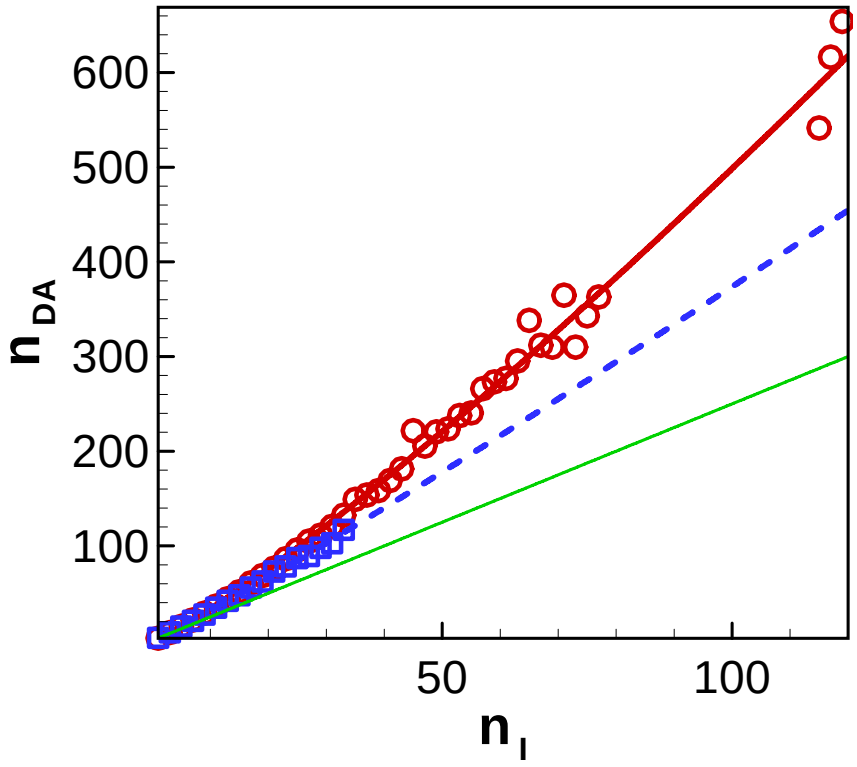

Figure 5.5: Number of defective atoms (n_{DA}) as a function of number of interstitials in a cluster (n_I): pure Si (circles with thick solid line), 0.9% carbon-doped (squares with dash line). The thin solid line shows linear evolution for reference.

5.3 Mean Field Scaling Analysis

5.3.1 Size Distribution Evolution

The time evolution of the average interstitial cluster size for the pure silicon and carbon-doped MD simulations are shown in Figure 5.6. The average cluster size is defined here as M_2 / M_1, where $M_q = \sum_n n^q X_n$ and X_n is the number of clusters of size n.

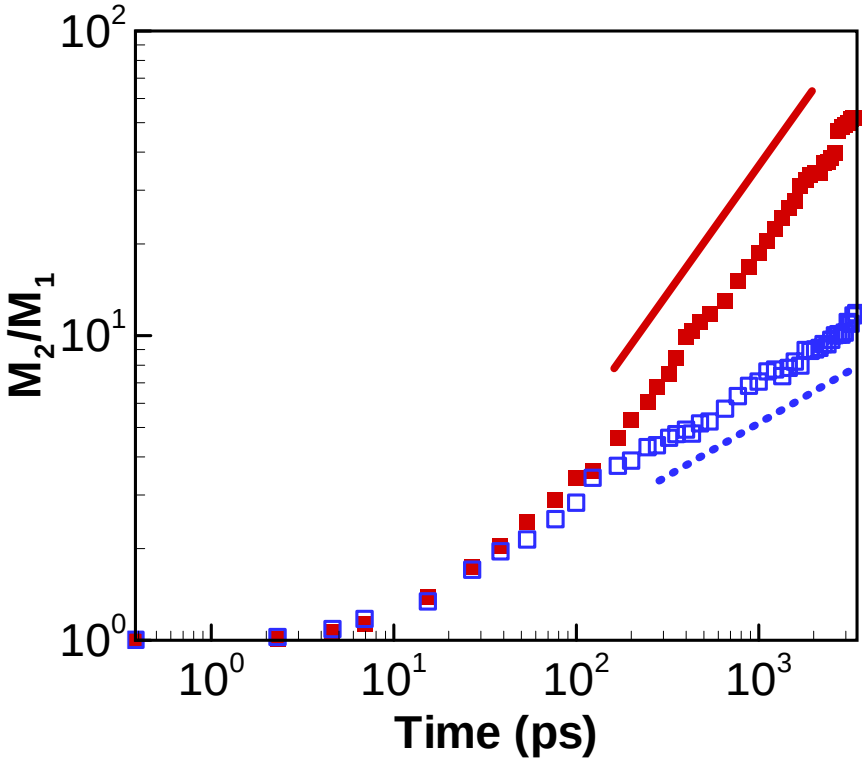

Figure 5.6: Evolution of the average interstitial cluster size, M_2/M_1, for pure Si (solid squares) and 0.9% C-doped Si (open squares). Exponents of the power-law fits are 0.81 for pure Si (solid line) and 0.37 for 0.9% C-doped Si (dashed line).

Both evolutions show an initial lag followed by the establishment of power-law scaling, $\sim t^z$ with the pure silicon case clearly exhibiting much faster evolution than the C-doped system (exponents, z, are 0.81 and 0.37, respectively). As in previous studies of vacancy aggregation in silicon,[121, 122] these evolutions indicate that it should be possible to interpret the interstitial aggregation profiles in the context of a mean-field model, which is outlined below. The individual distributions of small clusters ($n \leq 4$) for both cases are plotted in Figure 5.7.

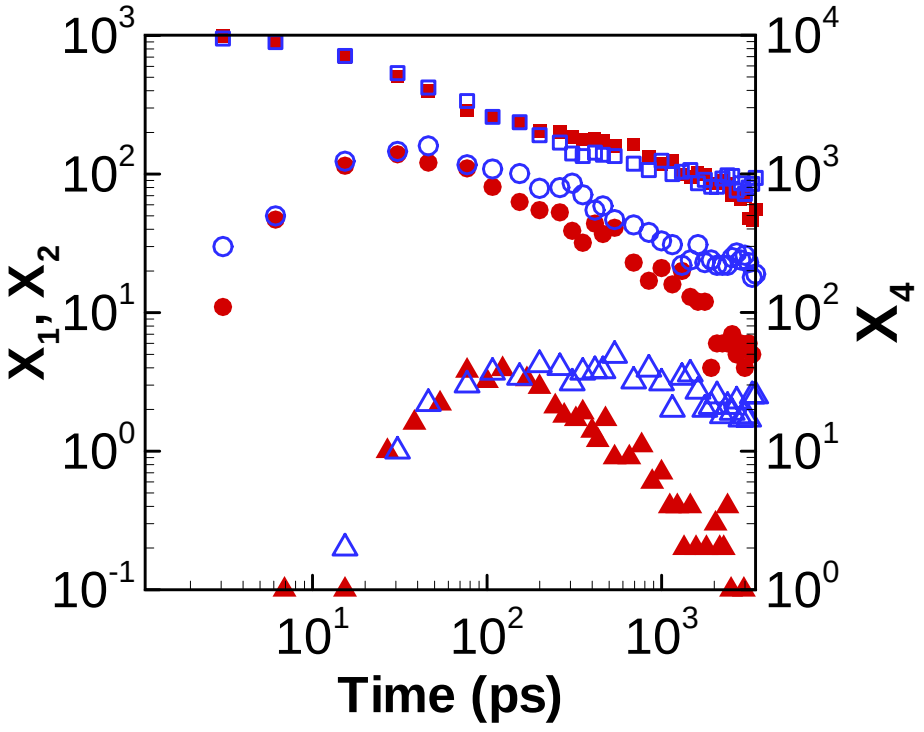

Figure 5.7: Evolution profiles for interstitial clusters of size 1, 2 and 4. Pure Si - filled symbols, 0.9% C-doped Si - open symbols. Tetramer profile is based on the right-hand side axis for clarity.

Interestingly, the single self-interstitial profiles are essentially identical throughout the simulation, indicating that *the presence of carbon does not substantially affect the transport of single self-interstitials*. However, for dimers and tetramers (and for larger clusters not shown in the figure), substantial divergence between the pure Si and C-doped simulations can be observed after 200 ps of simulation time. The extent of the divergence appears to increase with cluster size – in fact, for the duration of the simulation, the tetramer concentration in the carbon-doped case is essentially constant

and only begins to drop at the end of the simulation after reaching a maximum at 100 ps. In contrast the tetramer profile in the pure Si case rapidly decreases, indicating growth to larger sizes. Note that both dimers and tetramers form at the same rate in both simulations, and it is their growth to larger sizes which is most influenced by the presence of carbon.

5.3.2 A. Mean-field scaling approximation for aggregation

The power-law scaling of the average cluster sizes in Figure 5.6 suggest that a mean-field scaling analysis might be appropriate for compactly describing the carbon effect at the continuum scale. As discussed earlier, the co-existence of carbon and silicon atoms generally implies that a two-dimensional cluster representation is necessary to describe the evolution profiles. However, here we show that an effective medium formulation is appropriate, in which the carbon atoms simply modify the properties of self-interstitial clusters. The successful application of mean-field scaling theory to (single-component) defect aggregation has already been demonstrated by Prasad and Sinno in previous work.[121, 122]

A transformation proposed by Family et al.,[49] and later by Sorensen et al,[135] leads to the collapse of the Smoluchowski equation for a one-dimensional (single component) cluster system,

$$\frac{dX_k}{dt} = \frac{1}{2}\sum_{i+j=k}\left[K(i,j)X_iX_j - F(i,j)X_{i+j}\right] - \sum_{j=1}^{\infty}\left[K(k,j)X_kX_j - F(k,j)X_{k+j}\right] \quad (5.1)$$

into a single ordinary differential equation for the scaled average size, n^*:

$$\frac{dn^*}{dt^*} = n^{*\lambda} - n^{*(\alpha+2)} \tag{5.2}$$

In eq. (5.1), *K (i, j)* is the coagulation rate between two clusters of size *i* and *j*, and *F (i, j)* is the rate of dissociation of a cluster of size *i+j* into two clusters of size *i* and *j*. Implicit in the derivation of eq. (5.2) is that the coagulation and fragmentation kernels, *K (i, j)* and *F (i, j)*, are homogeneous, i.e. $K(ai, aj) = a^{\lambda} K(i, j)$ and $F(ai, aj) = a^{\alpha} F(i, j)$.

In eq. (5.2), $n^* = n(t)/n_0$ and $t^* = t/t_0$, where n_0 and t_0 are the equilibrium average cluster size, and the characteristic time to reach this equilibrium, respectively. For very small times, i.e. when $n^* << 1$, and assuming that fragmentation is not important at this stage of the evolution, the solution of eq. (5.2) is given by

$$n^* = \left[(1-\lambda) t^* + n_i^{*(1-\lambda)} \right] \tag{5.3}$$

where $n_i^* = n\ (t=0)/n_0$ is the scaled initial value of the mean cluster size, and $z = 1/(1-\lambda)$. Equation (5.3) implies that the average size should evolve as $n^* \sim t^z$, once the first term becomes sufficiently large.[122] Now, assuming that the entire aggregation process is diffusion-limited, the coagulation kernel, *K (i, j)*, is proportional to

$$K(i,j) \sim (D_i + D_j)(r_i + r_j)^2 \tag{5.4}$$

where r_x and D_x (x=i, j) are the capture radius and diffusivity, respectively, of a cluster of size x. Requiring that this kernel be homogenous is equivalent to requiring that both the capture radius and diffusivities also be homogenous in the cluster size.

5.3.3 Capture radius model for interstitial clusters and scaling predictions

The capture radius of a cluster is usually closely related to its size assuming that there are no long-range effects transmitted through the lattice. Here, we assume that the capture zone of an interstitial cluster scales with size as the cube root of the number of DAs contained within the cluster. The data in Figure 5.5 gives $r_{cap}(n_I) \sim n_I^{0.39}$ and $r_{cap}(n_I) \sim n_I^{0.36}$ for the pure silicon and carbon-doped cases, respectively, where n_I is the number of interstitials in a cluster. Note that the actual capture radius of the cluster is not required and only the scaling behavior is needed for the present mean-field analysis. Further assuming that $D_{\gamma i} = \gamma^p D_i$, and using eq. (5.4), the homogeneity condition for each case can be written as,

$$K(\gamma i, \gamma j) = \gamma^{p+0.78} K(i,j), \quad (C = 0\%) \tag{5.5}$$

$$K(\gamma i, \gamma j) = \gamma^{p+0.72} K(i,j), \quad (C = 0.9\%) \tag{5.6}$$

The exponents for M_2 / M_1 from Figure 5.4 can now be used to determine *p*, which represents the decay rate of the effective cluster diffusion coefficient as a function of the number of interstitials in the cluster *as predicted by the mean-field scaling approximation*:

$$D_{n_I}(C = 0\%) \sim n_I^{-1.01} \tag{5.7}$$

$$D_{n_I}^{\ eff}(C = 0.9\%) \sim n_I^{-2.42} \tag{5.8}$$

The mean-field model therefore indicates that power-law evolution of the average cluster size, M_2 / M_1, with exponents 0.81 and 0.37 (Figure 5.6), requires that the cluster diffusivity must decay with cluster size as stated in eqs. (5.7) and (5.8), respectively. In other words, the observed carbon effect can be explained purely on the basis of cluster diffusion inhibition. Note that the mean-field scaling analysis does not require that single interstitial diffusion be altered, a result that is consistent with the profiles shown in

Figure **5.7**.

5.3.4 Atomistic Studies of Cluster Diffusion

In order to test the hypothesis that carbon acts via cluster pinning as well as the overall validity of the scaling analysis presented in the previous section, a sequence of detailed cluster diffusion measurements was performed using lengthy (7-20 million time steps)

MD simulations. One to nine self-interstitials were placed in a host lattice containing up to 1,728 lattice atoms, depending on the size of the cluster and the desired carbon concentration. For each case, zero to seven silicon lattice atoms were replaced by carbon atoms. Between 4 and 8 simulations were performed for every situation in order to increase the statistical accuracy of the results. The mean-square displacement (MSD) of each cluster center-of-mass was computed by periodically quenching the simulation cell and locating DAs as described in Section 5.2.1.

Interstitial cluster diffusivity in the presence of carbon must be defined carefully. Implicit within the mean-field modeling presented in Section 5.3 was that the carbon atoms simply modified the diffusion and geometric properties of a cluster containing a given number of (self or carbon) interstitial atoms. In other words, the carbon atoms were considered as part of an effective medium that changes as the carbon concentration is varied, and the number of carbon atoms contained in a given cluster is not an explicit variable. Therefore, in the diffusion runs, we do not make a distinction between various cluster configurations and compositions, but rather, only monitor the overall diffusivity of the cluster averaged over all possible configurations. In all cases, time intervals in which the cluster was observed to fragment into two or more sub-clusters were discarded from the overall MSD calculation.

In order to demonstrate that the effect of carbon atoms on interstitial cluster diffusion can be described on a concentration basis, even when only a few carbon atoms are present, several diffusion runs were performed for each interstitial cluster size in which the total system size was varied but the carbon concentration was fixed. For example, the diffusivity of a cluster of three interstitials in a 0.4% carbon-doped system was measured

in host systems containing 512,1000, and 1728 silicon atoms with 2,4, and 7 carbon atoms, respectively, each corresponding to approximately 0.4% carbon concentration. A summary of the diffusion measurement simulation conditions used in this work is given in Table 5.1. The choice of interstitial cluster sizes considered at each carbon concentration was based purely on computational limitations – cluster diffusivity decreases with increasing carbon concentration and cluster size. Therefore, at the highest carbon concentration (~0.9%), the largest interstitial cluster size considered was four.

Table 5.1: System size and interstitial cluster size used for cluster diffusivity measurements as a function of carbon concentration (%C).

% C	*System Size*	*Cluster Size*
0	512,1000,1728	1,2,3,4,5,6,9
0.2	512,1000,1728	1,2,3,6
0.4	512,1000,1728	1,2,3,6
0.8,0.9	512,1000	1,2,3,4

Diffusion coefficients for clusters containing up to nine self-interstitials in varying background carbon concentrations are shown in Figure 5.8, along with power-law fits. Several immediate observations can be made.

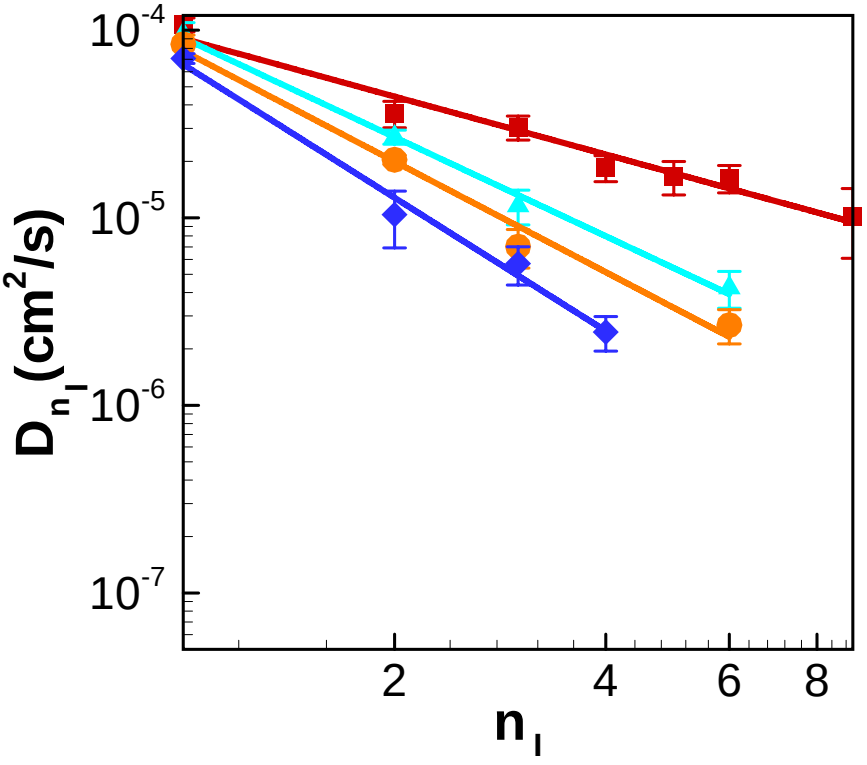

Figure 5.8: Self-interstitial diffusivities as a function of size with varying carbon concentrations. (a) 0% C (squares), (b) 0.2 % C (Triangles), (c) 0.4 % C (Circles), and (d) 0.9 % C (Diamonds).

First, at all carbon concentrations, the decay of cluster diffusivity with size is well represented by a single power law. Furthermore, the power law exponent is seen to become more negative as the carbon concentration is increased, as predicted by the mean-field scaling analysis in the previous section. Interestingly, we find once again that the effect of carbon on the diffusivity of a single self-interstitial is quite small compared to the large reduction observed in the case of the larger clusters. This finding is consistent with the monomer evolution profile in Figure 5.7 and further suggests that carbon-inhibition of interstitial aggregation (and dissolution) arises from the pinning of

interstitial *clusters*, rather than single self-interstitials. It should be emphasized that carbon does reduce single interstitial diffusivity to some degree, but to an extent that is much less than predicted by continuum models that assume that this is the dominant TED reduction mechanism.[85] Figure 5.9 shows the predicted diffusion coefficient for the 3-interstitial cluster in 0.4% carbon-doped silicon using three different simulation system sizes. The estimated diffusion coefficient is constant to within the uncertainty in the measurements, confirming that the carbon effect on cluster diffusion can be interpreted using the continuum concept of concentration, even in these very small discrete systems.

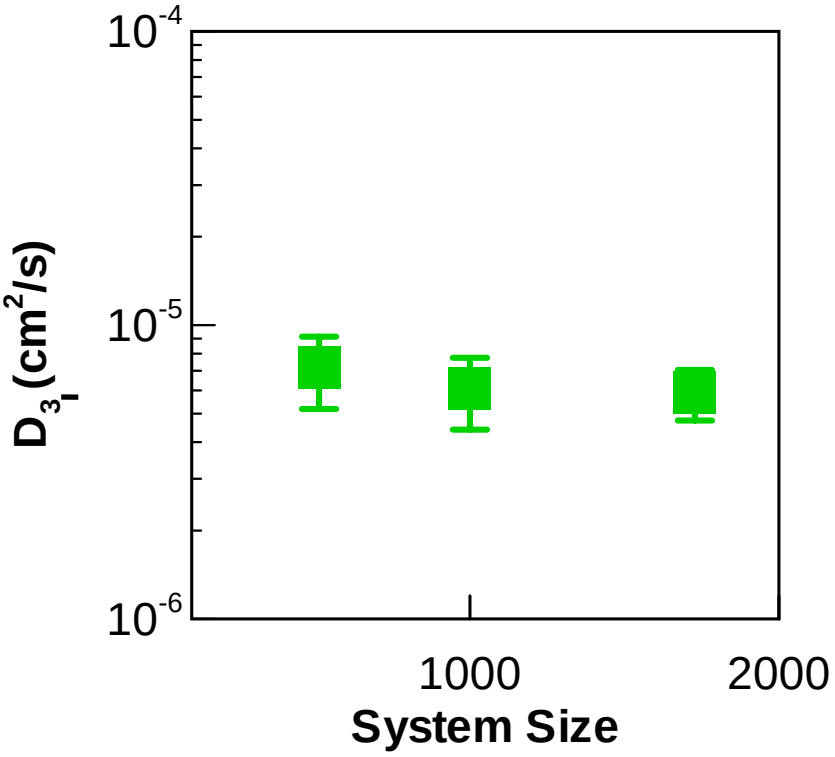

Figure 5.9: Effect of system size on estimation of 3-interstitial cluster diffusivity for a 0.4% carbon-doped silicon.

The exponents of the power-law fits for the diffusion coefficients as a function of cluster size are shown in Table 5.2 as a function of background carbon concentrations for both the atomistic simulation data and the mean-field fits. The diffusivity decay exponents for 0.9% carbon doping and the pure Si case, -2.36 and –1.03, respectively, are in excellent quantitative agreement with the mean-field scaling predictions (-2.42, and –1.02, respectively).

Table 5.2: Power law exponent, p, for cluster diffusivity ($D_n^{eff}(\%C) \sim n^p$) as a function of carbon concentration (%C), n represents interstitial cluster size.

%C	***p* (Direct MD)**	***p* (Mean-Field)**
0.0	-1.03	-1.01
0.2	-1.75	-
0.4	-1.96	-
0.9	-2.36	-2.42

This agreement indicates that the mean-field analysis is appropriate for this case, at least for the range of cluster sizes encountered in the PMD simulations. Note that even though only small clusters containing up to nine interstitials were considered in the diffusion runs, the fact that the PMD simulations predict a single power-law exponent until 3.46 ns of simulation time is evidence that the diffusion of larger clusters will continue to exhibit the behavior shown in Figure 5.8. After 3.46 ns of evolution, clusters

containing up to 120 interstitials (4337 DAs) were observed in the pure Si simulation and 35 interstitials (3164 DAs) in the 0.9% carbon doped simulation.

5.4 Sensitivity Analysis

5.4.1 Sensitivity to Empirical Potential Model

The analyses presented in the previous sections depend on the validity of several assumptions. The aim of this section is to address some of these and determine the sensitivity of our conclusions to various uncertainties. The most fundamental of these is the choice of the Tersoff multicomponent potential. As mentioned previously, few empirical potentials exist for the carbon-silicon system. We believe that the evidence cited in Section 5.1.2 is sufficient to give us reasonable confidence in the applicability of the multicomponent potential to the present problem, assuming that the overall interstitial aggregation picture is at least qualitatively captured by the potential. In order to test the latter assumption, another empirical potential for silicon, the Environment-Dependent Interatomic Potential (EDIP)[14, 90] was used to simulate interstitial aggregation in pure silicon. The temperature of the EDIP simulation was chosen to be 1600 K, which is the temperature at which the single self-interstitial diffusivity matched the Tersoff value at 2650 K.

The predicted evolutions of the average cluster size (M_2/M_1), the total cluster number (M_0), and the number of tetramers (X_4), is shown in Figure 5.10, along with the Tersoff predictions.

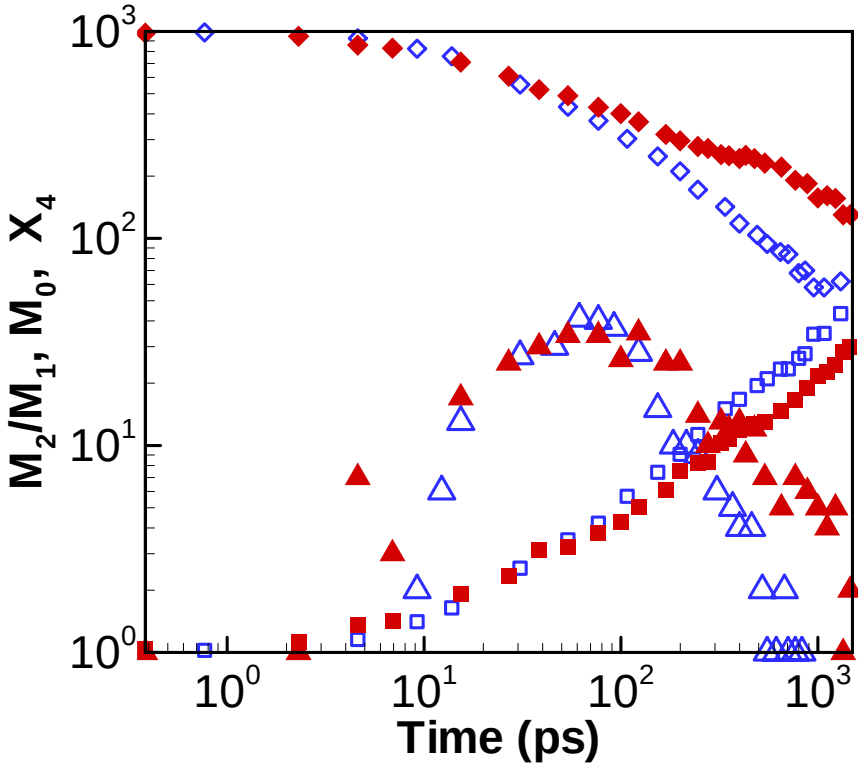

Figure 5.10: Evolution of the average cluster size (squares), total cluster number (diamonds), and tetramers (triangles) using the Tersoff (solid symbols), and EDIP (open symbols) potentials.

In all cases, the evolutions are qualitatively similar and only deviate (quantitatively) at later times. The EDIP potential appears to predict slightly more rapid evolution, with the largest difference appearing in M_0. This difference is due to a more rapid consumption of single interstitials in the EDIP case. The differences can be attributed to differences in the relative energies of each cluster size as well as the cluster diffusivities, most likely indicating that EDIP cluster diffuse slightly faster than Tersoff ones.

5.4.2 Sensitivity to Defective Atom Identification

The threshold displacement for identifying a defective atom in all previous results was set to $\theta = 0.63\,\mathring{A}$ along with an interaction distance of $\beta(3nn) = 4.82\,\mathring{A}$ for identifying DA clusters. Here we demonstrate that while the number of DAs per cluster, n_{DA}, is quite sensitive to changes in θ, the resulting interstitial cluster size distribution is only weakly affected. The number of DAs per cluster for different displacement thresholds is shown in Figure 5.11, and demonstrates the sensitivity of the presumed cluster size (on a DA basis) to this parameter. Note however, that the power-law scaling of n_{DA} is unchanged, which implies that the mean-field analysis in Section IV would, in any case, be unaffected by this variability.

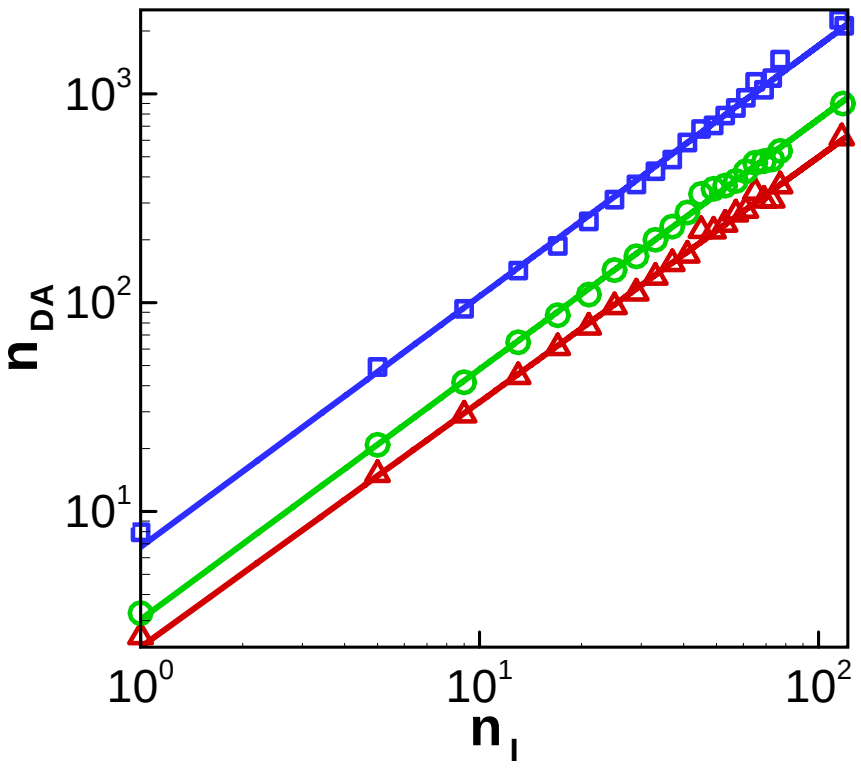

Figure 5.11: Number of defective atoms (n_{DA}) as a function of interstitial cluster size for different values of the threshold parameter, θ: (a) $\theta = 0.21\,\mathring{A}$ (squares), (b) $\theta = 0.42\,\mathring{A}$ (circles), (c) $\theta = 0.63\,\mathring{A}$ (triangles).

Another important point is that for all θ values considered in Figure 5.11, all 1,000 of the excess atoms in the system were located at every time snapshot. Obviously, for very large values of θ, some of the interstitial atoms would be missed, and this sets a (weak) upper bound on θ. Values of θ lower than $0.21\,\mathring{A}$ led to most of the atoms in the simulation cell being tagged as defective. Physically, this percolation observation is not consistent with the mean-field interpretation and therefore $\theta = 0.21\,\mathring{A}$ can be taken as a strict lower bound.

The question of how the choice of θ affects the predicted *interstitial* cluster size distribution was addressed next. The sensitivity of the average cluster size and total cluster number with respect to θ is shown in Figure 5.12. The predicted cluster size distribution is seen to depend only weakly on the choice of θ, and even then, only for small times. In fact, the exponent of the power-law evolution of M_2 / M_1 varies from the base value by only 2-3% when $\theta = 0.23\,\mathring{A}$ and the mean-field scaling analysis therefore is seen to be unaffected by the inherent arbitrariness in the choice of θ.

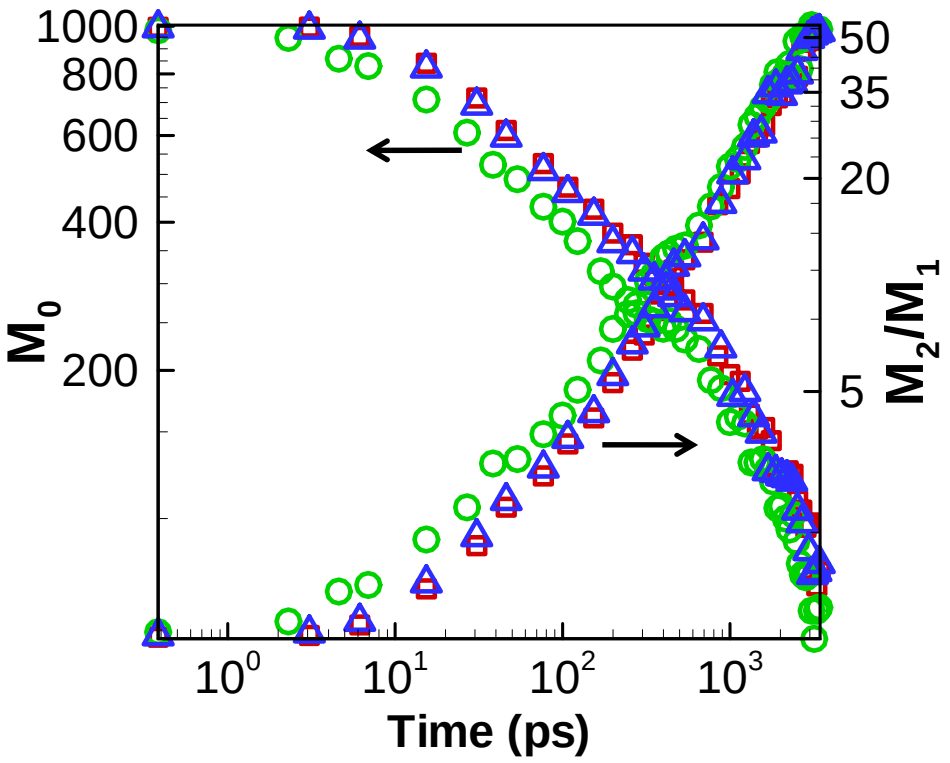

Figure 5.12: Sensitivity of the computed size distribution to the threshold parameter, θ. $\theta = 0.63\,\mathring{A}$ (squares), (b) $\theta = 0.42\,\mathring{A}$ (triangles), (c) $\theta = 0.21\,\mathring{A}$ (circles).

Similarly, for a fixed value of θ, DA distribution but not the interstitial cluster distribution (see Figure 5.13) was sensitive to interaction distance, β, in the range 2NN< β <5NN.

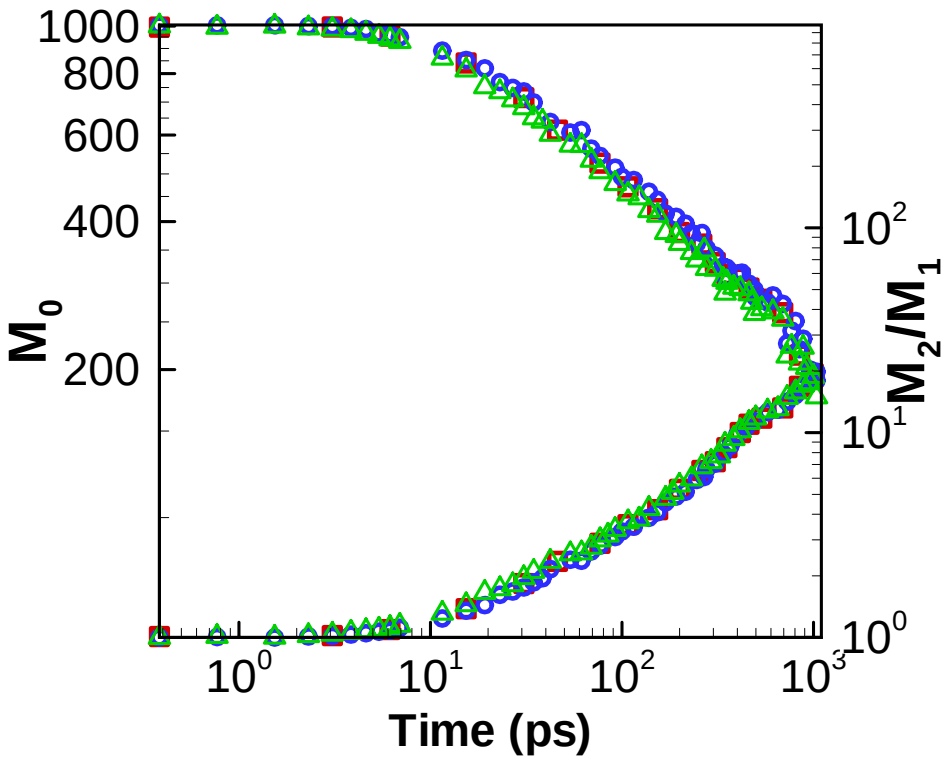

Figure 5.13: Sensitivity of the computed size distribution to the interaction distance, β. $\beta = 2NN$ (squares), (b) $\beta = 3NN$ (triangles), (c) $\beta = 4NN$ (circles).

5.5 Continuum Rate Equation Modeling

The detailed atomistic analysis presented in previous sections gives a mechanistically correct picture of the self-interstitial aggregation process. Unfortunately following the evolution of self-interstitial clusters using the detailed atomistic calculations is limited to few nanoseconds, as it becomes computationally expensive to carry out the large scale parallel MD simulations beyond a few nanoseconds. In order to extend the scope of atomistic simulations to realistic processing environments such as post implant annealing, a coupled rate equation based continuum model is being used to describe the interstitial cluster aggregation in silicon. Such a model has been developed by Prasad and Sinno [121] for vacancy aggregation process and is shown to reproduce an atomistic representation for vacancy cluster aggregation during crystal growth. Here we extend the continuum model for vacancy aggregation to silicon self-interstitial aggregation process, and come up with a mechanistically consistent picture of input parameters (free energy and cluster capture radii as a function of size), that accurately describe the self-interstitial aggregation process. The detailed model is described below.

An interstitial cluster of size i reacts with a cluster of size j to evolve onto a bigger cluster of size $(i+j)$,

$$I_i + I_j \underset{F(i,j)}{\overset{K(i,j)}{\longleftrightarrow}} I_{i+j} \tag{5.9}$$

Following Prasad and Sinno [121], evolution of self-interstitials via above reaction can be represented by sequence of coupled rate equations,

$$\frac{dX_i}{dt} = \sum_{j=1}^{i-1}\left[J_{i-j}^{j} - J_i^j \right] - J_i^i - \sum_{j\geq i}^{N_{\max}-i} J_j^i, \qquad 1 \leq i \leq N_d \tag{5.10}$$

$$\frac{dX_i}{dt} = \sum_{j=1}^{N_d}\left[J_{i-j}^{j} - J_i^j \right], \qquad N_d \leq i \leq N_{\max} - 1 \tag{5.11}$$

$$\frac{dX_i}{dt} = \sum_{j=1}^{N_d}\left[J_{i-j}^{j} \right], \qquad i = N_{\max} \tag{5.12}$$

$$J_i^j = 0, \qquad i < j \tag{5.13}$$

where, N_d represents the number of diffusing clusters and J_i^j is defined as the net forward flux at size i due to reaction enabled by a diffuser of size j, and is given by,

$$J_i^j = K\left(i, j\right) X_i X_j - F(i, j) X_{i+j} \tag{5.14}$$

where, X_i represents the concentration of interstitial clusters of size i, and $K(i, j)$ and $F(i, j)$ represents the forward and fragmentation rate constants, and are given by,

$$K(i, j) = \frac{4\pi}{V\delta}\left(D_i + D_j\right) r_{cap}^2(i, j) \exp\left(-\frac{G_{i+j\rightarrow(i+j)}}{KT} \right) \tag{5.15}$$

where, V is the system volume, which is known, and δ is the single self-interstitial hop distance, taken here as one bond distance, i.e. $\delta = 0.235nm$. D_i is the diffusivity of interstitial cluster of size i, as determined above in section 5.3.4. $r_{cap}(i, j)$ represents the capture radii for two clusters of size i and j, within an interaction range of each other. $G_{i+j\to(i+j)}$ is defined as the free energy barrier associated with reaction (5.9), and is given by,

$$G_{i+j\to(i+j)} = \Delta G_{i+j} - \Delta G_i - \Delta G_j - kT \cdot \ln(\frac{\Omega_2}{\Omega_1}) \tag{5.16}$$

where, ΔG_i is the free energy of formation of interstitial clusters of size i, and for a system consisting of N possible positions for single self-interstitial atoms,

$$\frac{\Omega_2}{\Omega_1} = \frac{(i+1).\left(\frac{N}{(i+1)} - X_{i+1}\right).X_i.X_1}{i.\left(\frac{N}{i} - X_i + 1\right).(N - X_1 + 1).(X_{(i+1)} + 1)} \tag{5.17}$$

Thus to completely solve the system of equations (5.10)-(5.13), all we need to specify is the set of input parameters (formation free energy, ΔG_i of interstitial cluster of size i, and the capture radii).

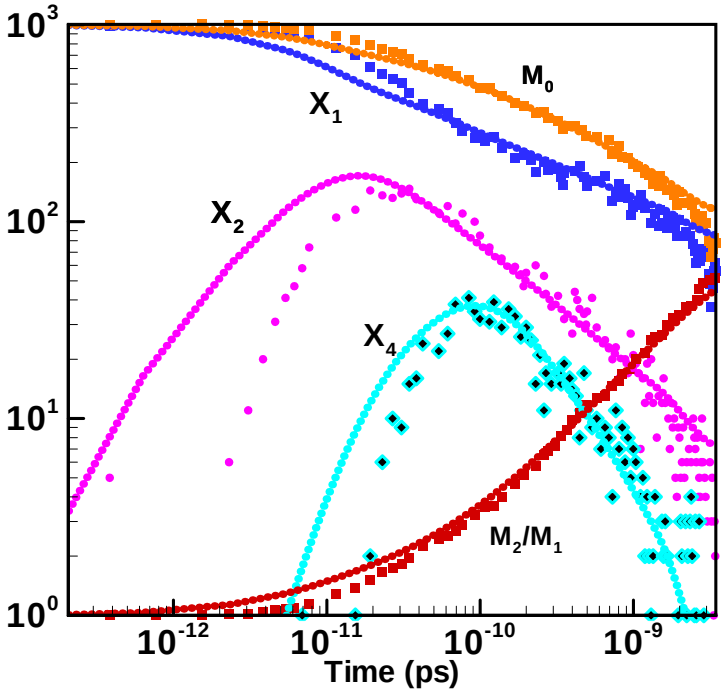

Figure 5.14: Continuum rate equation fit (dotted curves) to the MD size-distribution (solid data points) for interstitial clusters with 0% carbon content

These parameters are obtained by continuously regressing the size-distribution from the continuum model to the one obtained from large scale parallel MD simulations using a combination of simulated annealing and genetic algorithm. The best fit size-distribution from the continuum model is shown in Figure 5.14, along with data from the large scale parallel MD simulations.

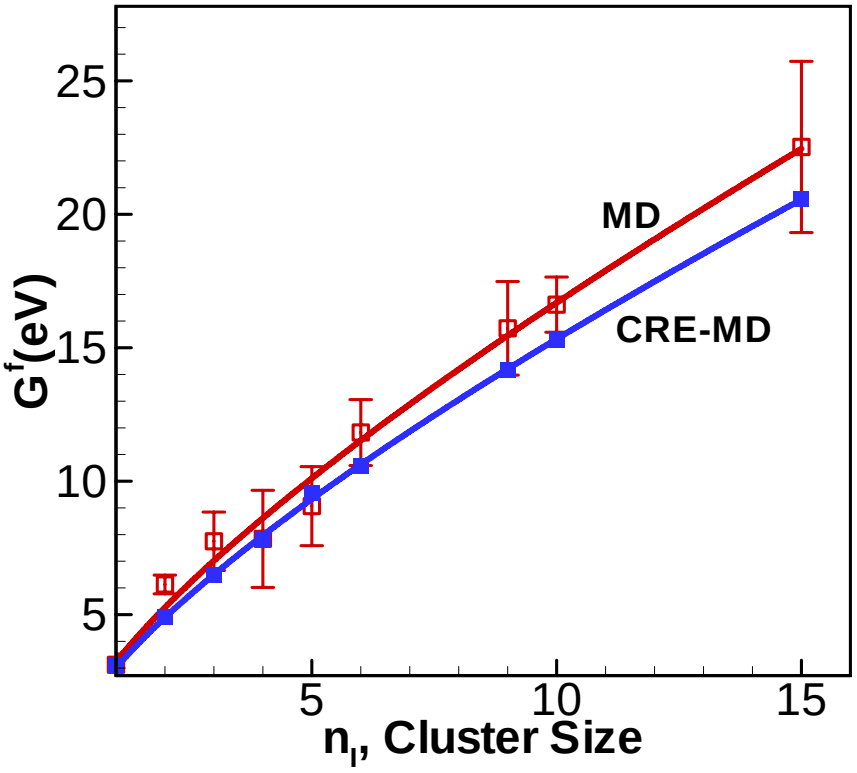

Figure 5.15: Formation free energy for interstitial clusters as a function of size, (open squares) from detailed MD calculations, (solid squares) from the best fit continuum rate equation model.

Figure 5.15 shows the corresponding formation free energy ΔG_i from the best fit size distribution. Also shown in the Figure 5.15, is the ΔG_i value obtained directly from detailed atomistic simulations, and is consistently higher than the best fit estimate. This can be attributed to the effect of internal configurational entropy, which is neglected in detailed atomistic simulations but is inherently included in the fitted value. Finally an estimate of capture radii $r_{cap}(i, j)$ is plotted in Figure 5.16 and is shown to lie within the average spherical cluster radii and maximum cluster radii. This is consistent with the

picture for vacancy cluster that also shows enhanced capture radii to account for the non-spherical shape of the vacancy clusters [121].

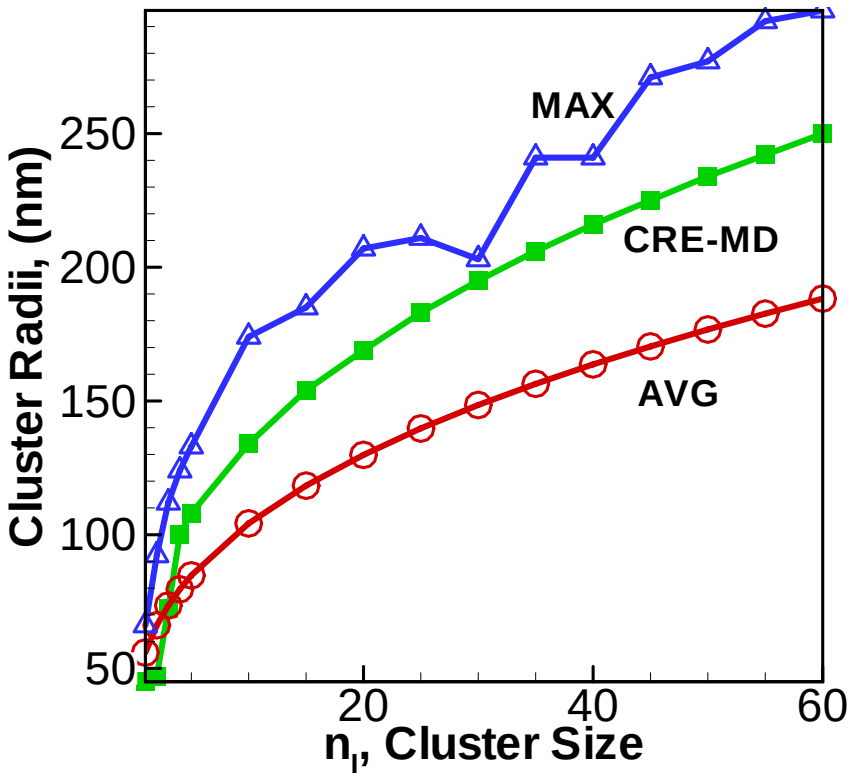

Figure 5.16: Cluster Radii based on the number of defective atom count as determined by fitting the continuum rate equation model to the MD (squares), is compared to average (circles) and max cluster radii (triangles) as obtained from the direct MD calculations.

Although the continuum rate equation model for vacancy aggregation can be reasonably extended to the process of silicon self-interstitial clustering, more work is required to extend it to the interstitial clustering in presence of carbon, as our effort to

correlate the and CRE and MD model for interstitial clustering in presence of carbon, didn't yield a good fit.

5.6 Conclusions

The results in this work provide new insight into the technologically and scientifically interesting TED inhibition effect of carbon doping. No assumptions are made other than the validity of the multicomponent Tersoff potential which has been tested extensively for this system.[108] Carbon is shown to inhibit cluster diffusion rather than single self-interstitial transport and the overall effect on aggregation can be described well by a quasi-one component mean-field representation. The results should be useful for constructing robust, but simple, rate equation models for carbon mediated self-interstitial aggregation/dissolution, and therefore increasing the robustness of TED models.

6 Conclusions

The objective of this thesis is to develop the computational methodology that quantitatively describes the evolution of defect clusters in crystalline solids at atomic level, and provide a mechanistic understanding of underlying physics behind the defect aggregation process. Although in this thesis, we have applied the methodology to understand the vacancy and self-interstitial aggregation phenomenon in Silicon, but the methodology is fairly general and can be applied to study aggregation phenomenon at atomic level in other crystalline solids.

In the first part of the thesis, a novel approach is proposed for probing the thermodynamics of defect and defect clusters in solids that inherently take care of the internal configuration entropy of point defect clusters. Contrary to the traditional practice of assuming ground state structure to be the lowest energy structure for all temperatures, the methodology inherently captures configurational entropy for all the possible structures dynamically at a given temperature. This has been successfully applied to estimate the thermo physical properties of vacancy clusters in crystalline silicon. In particular it is shown that configurational entropy at high temperature not only dramatically influences the thermodynamics of clusters, but also the aggregation kinetics through a modification of the effective capture radius. At high temperatures the effective surface energy for vacancy clusters is approximately constant over the size interval $2<n<35$, implying that the free energy of formation scales as $n^{2/3}$ for all cluster sizes

considered. In addition, since the 35-vacancy cluster is fully representative of the continuum limit because it is the smallest structure that can assume a perfect (111) faceted octahedral shape[125], as a result, the surface free energy scales as $n^{2/3}$ for *all* sizes at elevated temperatures. At lower temperatures, however, the smallest clusters clearly possess higher effective surface free energy and deviate from the $n^{2/3}$ scaling law. The observed deviation for small clusters arises because at low temperatures the effect of configurational entropy is negligible and the atomistic (discrete) nature of the clusters leads to a higher effective surface free energy.

The heretofore-neglected contribution of the configurational entropy to vacancy cluster free energy is obviously important in the context of modeling microvoid formation during Czochralski (CZ) crystal growth. During this process, vacancy aggregation is initiated at high temperature because of vacancy supersaturation that results from crystal cooling. Continuum models for void formation have shown unequivocally that low (i.e. ~0.75-0.85 J/m^2) values of σ are necessary to predict the correct nucleation onset temperature (approx. 1350-1400K [112]). On the other hand it has been difficult to reconcile this range of values for the cluster surface free energy with experimental measurements of the (111) surface energy at 77 K, which are clustered around 1.25 J/m^2 [39, 65, 83]. Since the (111) surface is widely considered as a good basis for estimating the free energy of experimentally observed octahedral voids, our prediction for the effective surface free energy of the 35V cluster, which is entirely comprised of (111) surfaces, decreases from about 1.24 J/m^2 at 77 K to 0.82 J/m^2 at the experimental melting temperature of silicon, 1685 K. Based on the present results, it is now possible to consolidate both values with a single result. The large clusters that are experimentally

observed in commercial single-crystal silicon after cooling are unaffected by configurational entropy, and are well described by the (111) surface energy model. However, early during the nucleation process, small clusters at high temperature are spatially extended due to a combination of configurational and vibrational entropy and are therefore characterized by a much smaller surface free energy.

In the second part of the thesis, a comprehensive picture of self –interstitial aggregation in silicon under the external conditions of temperature and constant hydrostatic pressure is presented. At high temperature and compressive pressure, self-interstitial clusters assume disordered, three-dimensional configurations (amorphous) until they reach large sizes. At lower temperatures and tensile pressure, clusters undergo a morphological transition from the three-dimensional state to planar configurations which includes RLD {111}, RLD {113} and planar PDL {111} and FDL {111}. The critical size for this transition is temperature dependent and becomes smaller as the temperature is decreased, presumably because of reduced entropic favorability of the three-dimensional configurations at low temperatures. Moreover, the transition appears to be kinetically favorable and no apparent barriers are observed in our simulations. Figure 6.1, shows an evolution map for self-interstitial aggregation as a function of cluster size and temperature. In most cases the effect of hydrostatic pressure is qualitatively similar to increasing the temperature.

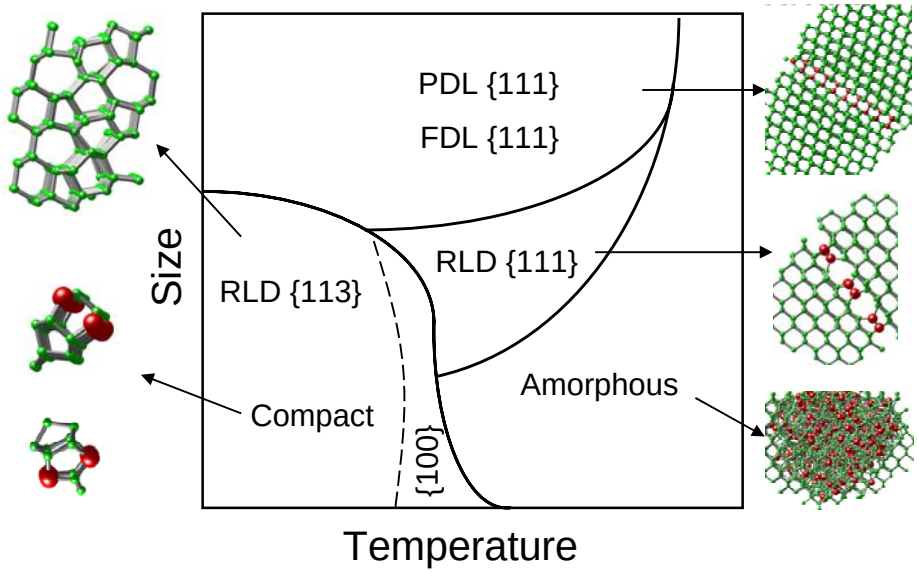

Figure 6.1: Evolution map for self-interstitial aggregation as a function of cluster size and temperature. In most cases, the effect of hydrostatic pressure is qualitatively similar to increasing the temperature.

In Chapter 4, a detailed thermodynamics analysis (by extending the approach developed for vacancy clusters) of various cluster configurations is employed to probe the mechanistic origins of these observations. At low temperature and/or tensile lattice strain, compact configurations for certain cluster sizes n_I=4, 8, 12 are observed in special "magic" configurations and are favored over other possible rearrangements by a combination of low formation energy and large vibrational and configurational entropy. It must be noted that while there is only one magic configuration for n_I=4, the Humble/Arai configuration, whereas for n_I=8 and 12, two main types of distinguishable configurations are possible, which are directly related to the formation of {113} and {100} planar defects The entropic sources are particularly large for structures comprised of the

Humble/Arai four interstitial building block, which is the building block for self-interstitial clusters in the compact configuration, and provide a compelling explanation as why very strong stability at n=8 has been extracted from experiments at moderate annealing temperature but not yet confirmed by literature calculations of formation energies to date. Note it is not possible to extend our simulations to the point at which {113} defects evolve by unfaulting into lower energy {111} defects, but previous work shows that this transition is expected at around n_I = 500. At higher temperatures (with zero or compressive strain), the density of states associated with interstitial clusters for most sizes, except n_I=4, is sufficiently large so as to "drown out" the special configurations that lead to {100} and {113} planar defects. As a result, most small clusters assume three-dimensional amorphous configurations up to a certain (temperature and pressure dependent) critical size at which point they collapse into {111}-oriented planar defects of various types including RLDs, FDLs, and PDLs, all of which have been observed experimentally. In this growth mode, the transition to {111} defects is much earlier than that associated with the {113}-{111} transition, and {113} defects are never formed. However, note that even at zero strain, {100} defects are still observed because of the large vibrational entropy associated with the Humble/Arai configuration.

Lattice strain can dramatically alter the pathway by which self-interstitials aggregate to form the various types of cluster morphologies observed in the literature. A key aspect of this mechanism is that lattice strain acts by modifying the overall density of states distribution of formation energies associated with a cluster, rather than by strongly modifying the formation thermodynamics of a particular cluster structure. Thus, although the particular cluster configurations responsible for {113} and {100} motif

formation are entropically stabilized relative to other configurations, this stabilization can become overwhelmed by the large number of other possible (usually higher energy) configurations. Unfortunately, our results do not explain the apparent dearth of {100}-oriented defects in damaged, interstitial-rich silicon; in agreement with previous calculations, these are found to be both energetically and now, also entropically, favorable.

Finally in the Chapter 5, we investigate the effect of carbon on self-interstitial aggregation. The presence of carbon in the silicon dramatically reduces cluster coalescence, with almost no direct effect on the single self-interstitials. This suggests that suppression of transient enhanced diffusion of boron (in presence of carbon), could be due to the direct interaction between carbon atoms and self-interstitial clusters.

6.1 Future Work

The following discussion proposes extensions to the work done in this dissertation.

6.1.1 Effect of Non-Hydrostatic (Biaxial and Uniaxial Stress) on defect clustering

Although in this thesis, we only studied the impact of constant hydrostatic pressure, the quantitative approach we have developed here can be easily extended to study the defect dynamics in biaxial and uniaxial stress/strain systems. Biaxial and uniaxial stress fields are becoming more common with use of SiGe over Si technology, and further work will be required to characterize the effect of these fields on self-interstitial clustering.[10]

Recent DFT calculations show that in some cases the differences may be important and may lead to additional heterogeneities in the cluster distribution.[16]

6.1.2 Cluster Patterning in Multi-Component Systems

As the device dimension continues to shrink down to sub 20nm, it will bring a marked shift in micro-electronic device manufacturing processes, which may no longer apply to nanoscale device production. Many efforts have been made to fabricate nanoscale devices using so-called "bottom up" approaches, in which devices are built atom by atom. The most common approach is to use some kind of self-assembly, which refers to a broad class of systems in which there exists a natural driving force for atomic aggregation into distinct clusters. Two key challenges arise in the application of self-assembly to device fabrication: (1) How can self-assembly be driven to create "perfect" (i.e. defect-free) phases, even in the presence of strong entropic forces, and (2) How can the spatial distribution of these clusters be controlled to create structures that are useful?

Directed aggregation under stress is one such potential approach which takes advantage of the inherent coupling between mechanical and chemical potential fields. In other words, the thermodynamic (and transport) properties of solid solutions depend (sometimes strongly) on the local stress environment in a solid. Thus by controlling the mechanical environment in the solid, aggregation potentially can be directed spatially.

Consider an alloy AB, containing an excess of chemical species A, in the interstitial positions. The excess A will tend to diffuse, and form large aggregates/precipitates of A in the surrounding AB (substrate) matrix. Rather than letting

excess ‘A’ particles to diffuse randomly, and coalesce into randomly distributed clusters, it has been shown that it is possible to modulate (using external stress, for example) the motion of ‘A’ particles to form uniformly distributed ‘A’ precipitates in the AB matrix. A schematic description of external stress modulated precipitation is shown in Figure 6.2.

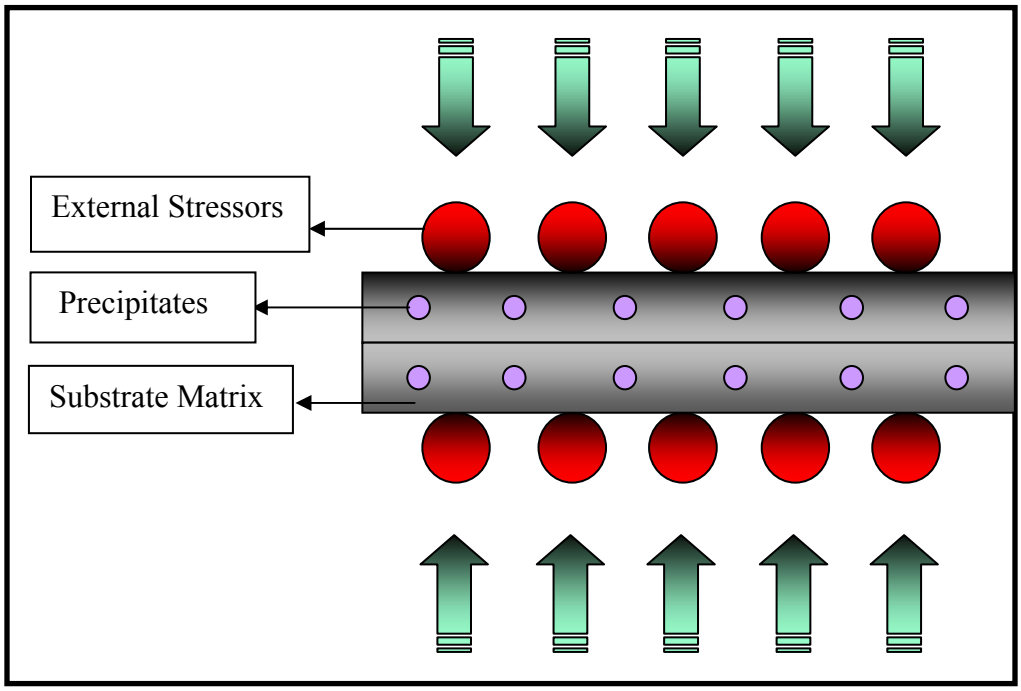

Figure 6.2: Selective precipitation using external stress

Arsenic precipitation in GaAs is an example of one such system that has been experimentally realized in which uniformly distributed precipitates of arsenic were formed in a GaAs matrix. This system has a potential application in fabrication of nano-electronic circuitry; based on single-electron tunneling devices, where small arsenic

precipitates would act as a metallic islands and the GaAs (semiconductor) matrix would serve as insulating tunnelling barriers between the islands[79, 80] Recent experiments on selective arsenic precipitation in GaAs[94, 114, 125] have demonstrated that directed self-assembly using external stress is a indeed a feasible option. Another potential system where this technique can be applied is the aggregation of Si nano-crystallites in silicon dioxide matrix under an externally applied stress field. Note that even though we have used an alloy AB to explain the process of directed aggregation, it applies equally well in case of single element matrix say M, containing vacancies, self-interstitials, or substitutional and interstitial impurities.

Directed assembly using external strain offers a tremendous opportunity, however challenges remain to take these technologies to a manufacturing level. This is only possible by first developing a through understanding of thermodynamics of defects and defect clusters. The quantitative approach we have developed can be extended to study the atomic scale mechanisms that couple mechanical and thermodynamic driving forces for directed aggregation of a multi component system.

Bibliography

1. www.apple.com/pr/products/
2. www.nobelprize.org/educational_games/physics/transistor/history/index.html
3. www.lammps.sandia.gov/
4. http://www.caesar.de/english/research/project_groups/cg_mission.html
5. www.intel.com/research/silicon
6. *International Technology Road Map for Semiconductors*. 2005.
7. Alippi, P., L. Colombo, P. Ruggerone, A. Sieck, G. Seifert, and T. Frauenheim, Phys. Rev. B 64 (2001).
8. Allen, M.P. and D.J. Tildesly, Computer Simulation of Liquids (Oxford University Press, Oxford, 1987).
9. Arai, N., S. Takeda, and M. Kohyama, Phys. Rev. Lett. 78, 4265 (1997).
10. Aziz, M.J., Appl. Phys. Lett. 70, 2810 (1997).
11. Bai, G. and M.A. Nicolet, J. Appl. Phys. 70, 649 (1991).
12. Bai, G. and M.A. Nicolet, J. Appl. Phys. 70, 3551 (1991).
13. Battaile, C.C. and D.J. Srolovitz, Annu. Rev. Mater. Res. 32, 297 (2002).
14. Bazant, M.Z., E. Kaxiras, and J.F. Justo, Phys. Rev. B 56, 8542 (1997).
15. Birner, S., J. Kim, D.A. Richie, J.W. Wilkins, A.F. Voter, and T. Lenosky, Solid State Commun. 120, 279 (2001).

16. Bondi, R.J., S. Lee, and G.S. Hwang, Phys. Rev. B 80 (2009).

17. Bondi, R.J., S. Lee, and G.S. Hwang, Phys. Rev. B 79 (2009).

18. Bongiorno, A., L. Colombo, and T.D. De la Rubia, Europhys. Lett. 43, 695 (1998).

19. Bongiorno, A., L. Colombo, F. Cargnoni, C. Gatti, and M. Rosati, Europhys. Lett. 50, 608 (2000).

20. Broughton, J.Q. and X.P. Li, Phys. Rev. B 35, 9120 (1987).

21. Cacciato, A., J.G.E. Klappe, N.E.B. Cowern, W. Vandervost, L.P. Biro, J.S. Custer, and F.W. Saris, J. Appl. Phys. 79, 2314 (1996).

22. Calvo, P., A. Claverie, N. Cherkashin, B. Colombeau, Y. Lamrani, B. de Mauduit, and F. Cristiano, Nucl. Instrum. Methods Phys. Res., Sect. B 216, 173 (2004).

23. Caturla, M.J., M.D. Johnson, and T.D. de la Rubia, Appl. Phys. Lett. 72, 2736 (1998).

24. Chou, C.T., D.J.H. Cockayne, J. Zou, P. Kringhoj, and C. Jagadish, Phys. Rev. B 52, 17223 (1995).

25. Claverie, A., L. Laanab, C. Bonafos, C. Bergaud, A. Martinez, and D. Mathiot, Nucl. Instrum. Methods Phys. Res., Sect. B 96, 202 (1995).

26. Claverie, A., L.F. Giles, M. Omri, B. de Mauduit, G. Ben Assayag, and D. Mathiot, Nucl. Instrum. Methods Phys. Res., Sect. B 147, 1 (1999).

27. Claverie, A., B. Colombeau, F. Cristiano, A. Altibelli, and C. Bonafos, Nucl. Instrum. Methods Phys. Res., Sect. B 186, 281 (2002).

28. Claverie, A., B. Colombeau, B. De Mauduit, C. Bonafos, X. Hebras, G. Ben Assayag, and F. Cristiano, Appl. Phys. A: Mater. Sci. Process. 76, 1025 (2003).

29. Colombeau, B., F. Cristiano, A. Altibelli, C. Bonafos, G. Ben Assayag, and A. Claverie, Appl. Phys. Lett. 78, 940 (2001).

30. Cook, S.J. and P. Clancy, Phys. Rev. B 47, 7686 (1993).

31. Coomer, B.J., J.P. Goss, R. Jones, S. Oberg, and P.R. Briddon, J. Phys.: Condens. Matter 13, L1 (2001).

32. Cowern, N.E.B., H.F.F. Jos, and K.T.F. Janssen, Mater. Sci. Eng., B 4, 101 (1989).

33. Cowern, N.E.B., K.T.F. Janssen, and H.F.F. Jos, J. Appl. Phys. 68, 6191 (1990).

34. Cowern, N.E.B., K.T.F. Janssen, G.F.A. Vandewalle, and D.J. Gravesteijn, Phys. Rev. Lett. 65, 2434 (1990).

35. Cowern, N.E.B., D. Alquier, M. Omri, A. Claverie, and A. Nejim, Nucl. Instrum. Methods Phys. Res., Sect. B 148, 257 (1999).

36. Cowern, N.E.B., G. Mannino, P.A. Stolk, F. Roozeboom, H.G.A. Huizing, J.G.M. van Berkum, F. Cristiano, A. Claverie, and M. Jaraiz, Phys. Rev. Lett. 82, 4460 (1999).

37. Cristiano, F., B. Colombeau, C. Bonafos, A. Altibelli, G. Ben Assayag, and A. Claverie, Gettering and Defect Engineering in Semiconductor Technology 82-84, 201 (2002).

38. Cristiano, F., N. Cherkashin, X. Hebras, P. Calvo, Y. Lamrani, E. Scheid, B. de Mauduit, B. Colombeau, W. Lerch, S. Paul, and A. Claverie, Nucl. Instrum. Methods Phys. Res., Sect. B 216, 46 (2004).

39. Cuendet, N., T. Halicioglu, and W.A. Tiller, Appl. Phys. Lett. 68, 19 (1996).

40. Czochralski, J., Z. physik. Chem. 92, 219 (1918).

41. Dai, J.G., J.M. Kanter, S.S. Kapur, W.D. Seider, and T. Sinno, Phys. Rev. B 72 (2005).

42. Dal, J., W.D. Seider, and T. Sinno, Mol. Simul. 32, 305 (2006).

43. Dearnaley, G.F., J. H.; Nelson, R. S.; Stephen, J., Ion Implantation (American Elsevier Publishing Co, New York,, 1973).

44. Eaglesham, D.J., P.A. Stolk, H.J. Gossmann, and J.M. Poate, Appl. Phys. Lett. 65, 2305 (1994).

45. Emoto, T., J. Ghatak, P.V. Satyam, and K. Akimoto, J. Appl. Phys. 106 (2009).

46. Estreicher, S.K., J.L. Hastings, and P.A. Fedders, Appl. Phys. Lett. 70, 432 (1997).

47. Estreicher, S.K., Physica Status Solidi B-Basic Research 217, 513 (2000).

48. Falster, R. and V.V. Voronkov, Mater. Sci. Eng., B 73, 87 (2000).

49. Family, F., P. Meakin, and J.M. Deutch, Phys. Rev. Lett. 57, 727 (1986).

50. Fedina, L., A. Gutakovskii, A. Aseev, J. Van Landuyt, and J. Vanhellemont, Philos. Mag. A 77, 423 (1998).

51. Fedina, L., A. Gutakovskii, A. Aseev, J. Van Landuyt, and J. Vanhellemont, Phys. Status Solidi A 171, 147 (1999).

52. Foll, H., U. Gosele, and B.O. Kolbesen, 77, 565 (1977).

53. Foll, H., U. Gosele, and B.O. Kolbesen, J. Cryst. Growth 52, 907 (1981).

54. Föll, H., *Defects in Crystals*.

55. Foulkes, W.M.C., L. Mitas, R.J. Needs, and G. Rajagopal, Reviews of Modern Physics 73, 33 (2001).

56. Franzblau, D.S., Phys. Rev. B 44, 4925 (1991).

57. Frenkel, D. and A.J.C. Ladd, J. Chem. Phys. 81, 3188 (1984).

58. Frenkel, D., Phys. Rev. Lett. 57, 2331 (1986).

59. Frewen, R.A., T. Sinno, E. Dornberger, R. Hoelzl, W. von Ammon, and H. Bracht, J. Electrochem. Soc. 150, G673 (2003).

60. Frewen, T.A., Ph.D. Thesis, University of Pennsylvanisa (2004).

61. Frewen, T.A., S.S. Kapur, W. Haeckl, W. von Ammon, and T. Sinno, J. Cryst. Growth 279, 258 (2005).

62. Frewen, T.A. and T. Sinno, Appl. Phys. Lett. 89 (2006).

63. Ghandhi, S.K., VLSI Fabrication Principles: Silicon and Gallium Arsenide (Wiley, New York, 1983).

64. Gilbert, J.C. and J. Nocedal, Siam Journal on Control and Optimization 2, 21 (1992).

65. Gilman, J.J., J. Appl. Phys. 31, 2208 (1960).

66. Girifalco, L.A., Statistical Physics of Materials (Wiley, New York, 1973).

67. Goedecker, S., T. Deutsch, and L. Billard, Phys. Rev. Lett. 88 (2002).

68. Goldstei.M, J. Chem. Phys. 51, 3728 (1969).

69. Goldstein, H., C.P. Poole, and J.L. Safko, Classical mechanics (Addison Wesley, San Francisco, 2002).

70. Goss, J.P., T.A.G. Eberlein, R. Jones, N. Pinho, A.T. Blumenau, T. Frauenheim, P.R. Briddon, and S. Oberg, J. Phys.: Condens. Matter 14, 12843 (2002).

71. Goss, J.P., B.J. Coomer, R. Jones, C.J. Fall, P.R. Briddon, and S. Oberg, Phys. Rev. B 67 (2003).

72. Goss, J.P., P.R. Briddon, T.A.G. Eberlein, R. Jones, N. Pinho, A.T. Blumenau, and S. Oberg, Appl. Phys. Lett. 85, 4633 (2004).

73. Hafner, J., Acta Mater. 48, 71 (2000).

74. Haynes, T.E., D.J. Eaglesham, P.A. Stolk, H.J. Gossmann, D.C. Jacobson, and J.M. Poate, Appl. Phys. Lett. 69, 1376 (1996).

75. Henkelman, G. and H. Jonsson, J. Chem. Phys. 115, 9657 (2001).

76. Hoover, W.G., B.L. Holian, and Hindmars.Ac, J. Chem. Phys. 57, 1980 (1972).

77. Hull, D. and D.J. Bacon, Introduction to Dislocations (Pergamon Press, Oxford, 1984).

78. Humble, P., Proc. R. Soc. London, A 381, 65 (1982).

79. Hung, C.Y., J.S. Harris, A.F. Marshall, and R.A. Kiehl, Appl. Phys. Lett. 73, 330 (1998).

80. Hung, C.Y., J.S. Harris, A.F. Marshall, and R.A. Kiehl, Appl. Phys. Lett. 75, 917 (1999).

81. Itsumi, M., H. Akiya, T. Ueki, M. Tomita, and M. Yamawaki, J. Appl. Phys. 78, 5984 (1995).

82. Itsumi, M., H. Akiya, T. Ueki, M. Tomita, and M. Yamawaki, Japanese Journal of Applied Physics Part 1-Regular Papers Short Notes & Review Papers 35, 812 (1996).

83. Jaccodine, R.J., J. Electrochem. Soc. 110, 524 (1963).

84. Jaraiz, M., G.H. Gilmer, J.M. Poate, and T.D. delaRubia, Appl. Phys. Lett. 68, 409 (1996).

85. Johnson, M.D., M.J. Caturla, and T.D. de la Rubia, J. Appl. Phys. 84, 1963 (1998).

86. Johnson, R.A., Phys. Rev. B 28, 6695 (1983).

87. Jones, K.S., S. Prussin, and E.R. Weber, Appl. Phys. A: Mater. Sci. Process. 45, 1 (1988).

88. Jones, K.S., J. Liu, L. Zhang, V. Krishnamoorthy, and R.T. DeHoff, Nucl. Instrum. Methods Phys. Res., Sect. B 106, 227 (1995).

89. Jones, K.S., ed. *Structure of ion implanted induced defects in c-Si*. Properties of Crystalline Silicon. (pp. 755-763). Institution of Engineering and Technology., ed. R. Hull. 1997. 755.

90. Justo, J.F., M.Z. Bazant, E. Kaxiras, V.V. Bulatov, and S. Yip, Phys. Rev. B 58, 2539 (1998).

91. Kapur, S.S., M. Prasad, and T. Sinno, Phys. Rev. B 69 (2004).

92. Kapur, S.S., M. Prasad, J.C. Crocker, and T. Sinno, Phys. Rev. B 72 (2005).

93. Kapur, S.S. and T. Sinno, Appl. Phys. Lett. 93 (2008).

94. Kiehl, R.A., M. Saito, M. Yamaguchi, O. Ueda, and N. Yokoyama, Appl. Phys. Lett. 66, 2194 (1995).

95. Kim, J., F. Kirchhoff, W.G. Aulbur, J.W. Wilkins, F.S. Khan, and C. Kresse, Phys. Rev. Lett. 83, 1990 (1999).

96. Kim, J., F. Kirchhoff, J.W. Wilkins, and F.S. Khan, Phys. Rev. Lett. 84, 503 (2000).

97. Kim, J.N., J.W. Wilkins, F.S. Khan, and A. Canning, Phys. Rev. B 55, 16186 (1997).

98. Kissinger, G., G. Morgenstern, J. Vanhellemont, D. Graf, U. Lambert, and H. Richter, Appl. Phys. Lett. 72, 223 (1998).

99. Kohno, H., N. Arai, T. Mabuchi, M. Hirata, S. Takeda, M. Kohyama, M. Terauchi, and M. Tanaka, Defects in Semiconductors - Icds-19, Pts 1-3 258-2, 547 (1997).

100. Kohyama, M. and S. Takeda, Phys. Rev. B 46, 12305 (1992).

101. Kohyama, M. and S. Takeda, Phys. Rev. B 51, 13111 (1995).

102. Kohyama, M. and S. Takeda, Phys. Rev. B 60, 8075 (1999).

103. Kotrla, M., Comput. Phys. Commun. 97, 82 (1996).

104. Lee, S. and G.S. Hwang, Phys. Rev. B 77 (2008).

105. Li, J.H. and K.S. Jones, Appl. Phys. Lett. 73, 3748 (1998).

106. Liu, J., M.E. Law, and K.S. Jones, Solid-State Electron. 38, 1305 (1995).

107. Liu, J., V. Krishnamoorthy, H.J. Gossman, L. Rubin, M.E. Law, and K.S. Jones, J. Appl. Phys. 81, 1656 (1997).

108. Mattoni, A., F. Bernardini, and L. Colombo, Phys. Rev. B 66 (2002).

109. Michel, A.E., W. Rausch, P.A. Ronsheim, and R.H. Kastl, Appl. Phys. Lett. 50, 416 (1987).

110. Mirabella, S., A. Coati, D. De Salvador, E. Napolitani, A. Mattoni, G. Bisognin, M. Berti, A. Carnera, A.V. Drigo, S. Scalese, S. Pulvirenti, A. Terrasi, and F. Priolo, Phys. Rev. B 65, 045209 (2002).

111. Muto, S. and S. Takeda, Philos. Mag. Lett. 72, 99 (1995).

112. Nakamura, K., T. Saishoji, T. Kubota, T. Iida, Y. Shimanuki, T. Kotooka, and J. Tomioka, J. Cryst. Growth 180, 61 (1997).

113. Napolitani, E., A. Coati, D. De Salvador, A. Carnera, S. Mirabella, S. Scalese, and F. Priolo, Appl. Phys. Lett. 79, 4145 (2001).

114. Ngo, T.T., P.M. Petroff, H. Sakaki, and J.L. Merz, Phys. Rev. B 53, 9618 (1996).

115. Nichols, C.S., C.G. Vandewalle, and S.T. Pantelides, Phys. Rev. Lett. 62, 1049 (1989).

116. Pan, G.Z. and K.N. Tu, J. Appl. Phys. 82, 601 (1997).

117. Pan, G.Z., K.N. Tu, and A. Prussin, J. Appl. Phys. 81, 78 (1997).

118. Pan, G.Z., K.N. Tu, and S. Prussin, Appl. Phys. Lett. 71, 659 (1997).

119. Parrinello, M. and A. Rahman, Phys. Rev. Lett. 45, 1196 (1980).

120. Prasad, M. and T. Sinno, Appl. Phys. Lett. 80, 1951 (2002).

121. Prasad, M. and T. Sinno, Phys. Rev. B 68, 045207 (2003).

122. Prasad, M. and T. Sinno, Phys. Rev. B 68, 045206 (2003).

123. Prasad, M., Ph.D. Thesis, University of Pennsylvania (2004).

124. Prunier, C., E. Ligeon, A. Bourret, A.C. Chami, and J.C. Oberlin, Nucl. Instrum. Methods Phys. Res., Sect. B 17, 227 (1986).

125. Romanov, A.E., P.M. Petroff, and J.S. Speck, Appl. Phys. Lett. 74, 2280 (1999).

126. Rozgonyi, G.A., A. Karoui, A. Kvit, and G. Duscher, Microelectron. Eng. 66, 305 (2003).

127. Rucker, H., B. Heinemann, D. Bolze, R. Kurps, D. Kruger, G. Lippert, and H.J. Osten, Appl. Phys. Lett. 74, 3377 (1999).

128. Sastry, S., Nature 409, 300 (2001).

129. Sciortino, F., W. Kob, and P. Tartaglia, Phys. Rev. Lett. 83, 3214 (1999).

130. Seeger, A. and K.P. Chik, Phys. Status Solidi 29, 455 (1968).

131. Simpson, T.W., R.D. Goldberg, and I.V. Mitchell, Appl. Phys. Lett. 67, 2857 (1995).

132. Sinno, T. and R.A. Brown, J. Electrochem. Soc. 146, 2300 (1999).

133. Sinno, T., H. Susanto, R.A. Brown, W. von Ammon, and E. Dornberger, Appl. Phys. Lett. 75, 1544 (1999).

134. Sinno, T., E. Dornberger, W. von Ammon, R.A. Brown, and F. Dupret, Mater. Sci. Eng., R 28, 149 (2000).

135. Sorensen, C.M., H.X. Zhang, and T.W. Taylor, Phys. Rev. Lett. 59, 363 (1987).

136. Stiebel, D., P. Pichler, and N.E.B. Cowern, Appl. Phys. Lett. 79, 2654 (2001).

137. Stillinger, F.H., J. Chem. Phys. 38, 1486 (1963).

138. Stillinger, F.H. and T.A. Weber, Phys. Rev. A 25, 978 (1982).

139. Stillinger, F.H. and T.A. Weber, Phys. Rev. B 31, 5262 (1985).

140. Stillinger, F.H., Science 267, 1935 (1995).

141. Stolk, P.A., D.J. Eaglesham, H.J. Gossmann, and J.M. Poate, Appl. Phys. Lett. 66, 1370 (1995).

142. Stolk, P.A., H.J. Gossmann, D.J. Eaglesham, D.C. Jacobson, C.S. Rafferty, G.H. Gilmer, M. Jaraiz, J.M. Poate, H.S. Luftman, and T.E. Haynes, J. Appl. Phys. 81, 6031 (1997).

143. Takeda, S., Jpn. J. Appl. Phys., Part 2 30, L639 (1991).

144. Takeda, S., Microscopy Research and Technique 40, 313 (1998).

145. Tan, T.Y., H. Foll, and W. Krakow, Appl. Phys. Lett. 37, 1102 (1980).

146. Tang, M.J. and S. Yip, Phys. Rev. B 52, 15150 (1995).

147. Tersoff, J., Phys. Rev. B 38, 9902 (1988).

148. Tersoff, J., Phys. Rev. B 39, 5566 (1989).

149. Tersoff, J., Phys. Rev. Lett. 64, 1757 (1990).

150. Tersoff, J., Phys. Rev. B 41, 3248 (1990).

151. Vaithyanathan, V., C. Wolverton, and L.Q. Chen, Acta Mater. 52, 2973 (2004).

152. Voronkov, V.V., J. Cryst. Growth 59, 625 (1982).

153. Voronkov, V.V. and R. Falster, J. Cryst. Growth 194, 76 (1998).

154. W. Häckl, J.V., Th. Wetzel, A. Sattler, R. Hölzl, W. v. Ammon, *Numerical simulation of point and bulk defects in monocrystalline silicon.* 2002.

155. Wang, F.G. and D.P. Landau, Phys. Rev. Lett. 86, 2050 (2001).

156. Wimmer, E. and W. Wolf, Mater. Sci. Semicond. Process. 3, 3 (2000).

157. Zawadzki, M.T., W.W. Luo, and P. Clancy, Phys. Rev. B 6320, 205205 (2001).

158. Zhang, L.H., K.S. Jones, P.H. Chi, and D.S. Simons, Appl. Phys. Lett. 67, 2025 (1995).